PHASE BEHAVIOR OF HYDROCARBON FLUIDS IN SHALE SYSTEMS FROM MOLECULAR SIMULATION

A Dissertation

by

BIKAI JIN

Submitted to the Office of Graduate and Professional Studies of
Texas A&M University
in partial fulfillment of the requirements for the degree of

DOCTOR OF PHILOSOPHY

Chair of Committee,	Hadi Nasrabadi
Committee Members,	Maria A. Barrufet
	Eduardo Gildin
	Sara Abedi
Head of Department,	A. Daniel Hill

May 2018

Major Subject: Petroleum Engineering

ABSTRACT

Production from shale reservoirs is getting more attention from the oil industry. However, the shale is not understood as well as conventional reservoirs. One complexity is the unclear fluid phase behavior in shale nanopores. Since the knowledge of the hydrocarbon phase behavior is fundamental for the petroleum reservoir simulation, the phase behavior in shale reservoirs has received significant attention in recent years. Since hydrocarbon fluids are stored inside nanopores of shale matrices, a great interaction exists among the pore boundary and fluid molecules. Thus, fluid phase behavior in a shale reservoir is substantially different from conventional behavior. Due to this interaction, the fluid molecules are distributed heterogeneously inside the nanopores and the phase diagrams are shifted under confinement.

Molecular simulation techniques have been developed in previous studies for an advanced performance in the phase behavior description under confinement. In this work, a new molecular simulation method, gauge-GCMC, is presented to study the phase behavior of multiple component fluids considering the confinement effect. This method is verified by matching the phase diagrams of simple and complex hydrocarbons with theoretical results and the simulation data from other techniques. The simulation results show that the density differences between vapor and liquid phases are reduced while critical densities increase under confinement. Also, the confined phase behavior has a great change in the fluid compositions, because heavier components have a stronger adsorption effect than that of lighter components.

Shale rocks usually have a wide pore size distribution (PSD) and the traditional single

pore-size models are not accurate enough to represent a real shale system. To understand the PSD effect on the phase behavior, the gauge-GCMC is used to generate phase diagrams based on two types of cylindrical models (single pore and multiple pores, including one based on Eagle Ford shale rock). The simulation results show that with an increasing pore size, the phase equilibrium properties approach the bulk values. In addition, the small pore causes a stronger shift in the phase diagram, compared with large pores. The small pores are filled before the large ones, which means that liquid condensation will first happen in the small pores. In the Eagle Ford test, it is possible to use a single pore model with a 10 nm diameter to represent the phase diagrams of this complex pore system.

To investigate the contribution from boundary material on the fluid phase behavior, two types of pore models (slit and cylinder), which are built from three materials (two inorganic minerals and one kerogen), are used to generate the phase diagrams of pure fluids (C_1 and C_3) and one ternary fluid ($C_1/C_3/nC_5$). Under confinement, liquid densities are reduced while vapor densities are increased in both pore models. Critical points are shifted to lower densities. For the ternary case, a large shift of the nC_5 composition is shown in the vapor phase ternary diagrams, while only small changes have been observed in the liquid composition. When the temperature increases to one typical shale condition, phase separation of the ternary fluid is available in slit pore tests, while only one phase is formed in tests of cylinder pores. Based on the comparison of all results, the cylinder pore, which has more adsorption surface area, can provide a stronger adsorption effect than the slit pore. The calcite models have a greater confinement effect on fluid properties, and the other two materials cause the similar shift effect on phase diagrams.

DEDICATION

To my family & my friends.

CONTRIBUTORS AND FUNDING SOURCES

Contributors

This work was supported by a dissertation committee consisting of Professor Hadi Nasrabadi [advisor] of the Department of Petroleum Engineering, Professor Maria A. Barrufet of the Department of Petroleum Engineering and Chemical Engineering, and Professors Eduardo Gildin and Sara Abedi of the Department of Petroleum Engineering.

All the work conducted for the dissertation was completed by the student independently.

The simulation work is supported by Texas A&M High Performance Research Computing Facility. The computations are conducted by a modified version of the Monte Carlo for Complex Chemical Systems (MCCCS) Towhee.

Funding Sources

Graduate study was supported from the Crisman Institute for Petroleum Research at Texas A&M University.

NOMENCLATURE

Q	System partition function
F	Helmholtz free energy
H	System Hamiltonian
K	Kinetic energy
U	Potential energy
$U_{nonbond}$	Nonbonded energy
U_{tail}	Tail correction in nonbonded energy
U_{bond}	Bonded energy
U_{bend}	Bond bending potential
U_{tor}	Torsion potential
U_{imp}	Improper torsion potential
k_B	Boltzmann's constant
R	Long-range correction parameter for tail energy
N	Molecular number
V	System volume
T	Temperature
P	Pressure
ρ	Average density inside box
μ_i	Chemical potential of component i
N_i	Molecule number of component i

Λ_i	Thermal de Broglie wavelength for component i
$\mathbf{p}^N$	Momenta of N particles
$\mathbf{r}^N$	Coordinates of N particles
$\mathbf{r_i}$	Coordinates of particle i
$\mathbf{r}_{ab}$	Vector between sites a and b
r_{ij}	Distance between particles i and j
r_{cutoff}	Cutoff distance
ε_{ij}	Potential well depth between particles i and j
σ_{ij}	Distant where the interaction energy is zero between particles i and j
W	Rosenbluth weight of the CBMC insertion
W_k	Rosenbluth weight of step k in the CBMC procedure
${P_{trial}}^{arb}(\mathbf{r}_j))$	An arbitrary trial distribution of $\mathbf{r}_j$
${P_{trial}}^{ideal}(\mathbf{r}_j))$	Trial distribution of an ideal system
$w_{ab}(\mathbf{r}_{ab})$	Site–site pair virial function

TABLE OF CONTENTS

Page

LIST OF FIGURES

FIGURE Page

LIST OF TABLES

TABLE Page

1. INTRODUCTION

1.1 Background

The production of shale reservoirs has increased dramatically over the past decade [1, 2], which will take a large share of energy supply in the United States over the next few decades. Since the booming development of shale reservoirs, a lot of research projects are proposed for a detailed understanding of the shale reservoirs. One main difference between shale and conventional reservoirs is the fluid phase behavior. Since the knowledge of phase behavior serves as a fundamental description of fluid properties in the oil and gas industry, it is essential in a lot of regions, such as reservoir simulation, well performance evaluation, and enhance oil recovery. However, phase behavior in shale condition has not been well studied compared with that in conventional reservoirs. Shale matrices contain pores with diameters in the nanometer range. Inside these nanopores, which are usually treated as the storage space for hydrocarbon fluids, the pore boundary molecules contribute a great impact on the distribution of fluid molecules in the pore.The combination of interactions between fluid-boundary and fluid-fluid leads to a heterogeneous molecular distribution of confined fluids [3]. This uneven molecular distribution results in the phase behavior under confinement, which is also named as confined phase behavior [4, 5].

The porous media in shale matrices consists of micropores (< 2 nm), mesopores (2 – 50 nm), and macropores (>50 nm) [6]. Usually, the pore system in shale is described as pore size distribution (PSD) [7–11]. Many techniques have been employed to determine the PSD, such as low pressure adsorption isotherm [7, 8, 11], high pressure mercury intrusion [9–11], small-angle or ultra-small-angle neutron scattering [7], nuclear magnetic

resonance spectrum [10, 12], and X-ray diffraction [13]. From these researches, the PSDs of shale reservoirs have been found to vary between samples and regions (Fig. 1.1). It can be concluded that nanopores are dominant in shale pore systems. There are even reports that the nanopores with diameters less than 10 nm take up to 40% of the total pore space [10, 14, 15]. Also, it should be noted that fluids can stay in an equilibrium state inside these nanopores. Thus, the PSD effect should be considered in the phase behavior study.

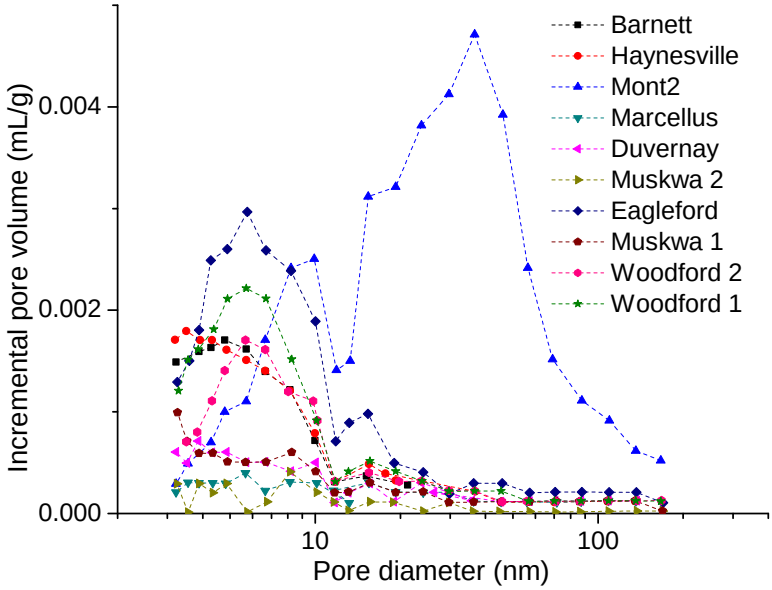

Sample data from shale gas reservoirs in North America [7]. Reprinted from [16].

Figure 1.1: Incremental pore volume plot for shale samples.

Shale is a multi-phase material in which organic nodules are mixed an inorganic matrix [17]. The nanopore system in shale is widely distributed in both organic and inorganic materials. It has been reported that the fluid-in-place can be divided into two

parts, the free molecules inside pores and adsorbed molecules along pore boundaries [18]. The amount of free fluid depends on the system porosity and the adsorbed fluid is determined by the pore surface. Usually, the porosity is provided by the organic matter along with some micro-structure for adsorption [19]. Inside these nodules, the organic matter consists of microporous materials with structures in nanometer scale [6]. Although the organic content only makes up a small portion of the total volume in shale [20], there is a large part of hydrocarbons associated with it. It is even assumed that half of the total hydrocarbons are adsorbed in organic matter [21]. However, the contribution of inorganic matter is not negligible in the evaluation of fluid-in-place. The inorganic matter has micro- to meso- pores which contain more adsorption surface [7]. As the inorganic matter occupies the majority of the material in shale, the nanoscale structure of the inorganic matrix can provide the similar constraint on fluids as that from organic materials [22]. It is reported that the North American shale reservoirs have a broad range of inorganic compositions, in which calcite, quartz, illite and muscovite take dominant [7]. Since fluids can stay in micro-structures inside organic and inorganic materials, the boundary material effect needs to be included in the study of phase behavior.

Efforts have been taken to investigate the confinement effect on the phase behavior of fluids in nanopores through several approaches. Experimentation is the most direct way to quantify the confined phase behavior based on adsorption isotherms. It has been reported that the critical temperatures of the fluid SF_6 are lower than the bulk values, based on the controlled pore glass (CPG) with 24 and 31 nm mean diameters, while the critical densities of the confined fluid are increased [23]. Based on CPG-10 model with 7.7 nm diameter, a supercritical fluid was observed at the reduced temperature $T_r = 0.985$ in the nanopore [24]. Another nanoporous material, MCM-41 silica, was used in several tests at several temperatures for various pore diameters to get the conclusion that the pressure

at phase equilibrium is raised when the pore diameter and temperature increasing [25]. Luo et al. captured the bubble point data of pure and binary fluids in nanopores through the DSC (differential scanning calorimetry) instrument [26–28]. An obvious difference was observed among the bubble point data of fluids under confinement and in bulk. Another nano-device, the chip of nanochannels, has been employed in the experiments to measure the confinement effect on phase behavior and visualize the fluid flow in nanopores [29–31]. Though experimentation is a direct way to capture the confinement effect, the data are limited to pore boundary materials, fluid types, pressure settings, and environmental temperature. To get a complete phase behavior description including the bulk and confinement conditions, simulation work is necessary to expand the studies of phase behavior in various situations.

Several adsorption models have been developed for the computation of fluid phase behavior under confinement. The theory of ideal adsorbed solution was designed for the equilibrium simulation in the mixture of ideal gases [32], however, it may not be suitable for the simulation of non-ideal fluids. To compute confinement effect from the boundary on the adsorption of mixtures, the Langmuir method, as well as BET approach, have been widely applied in various case studies [33–36]. The basic assumption for Langmuir methods is that one single layer, consisting of adsorbates without interaction between adsorbed molecules, is presented near the boundary and the ideal gas assumption is applied to other fluid molecules. The BET method designed as a development of the Langmuir model contains unlimited adsorption layers above the boundary surface under the assumption that no interaction among layers. The usage of both methods are limited by the assumptions and requires parameters from experimental data. Other approximations are required for the extension of the Langmuir method. In addition, Kelvin equation is used to calculate the pressure difference from a curved interface and

applied in the simulation of the porous system [36, 37]. However, all these models do not cover the hysteresis effect, which is important for fluids under confinement [4, 38].

Recently, several new modifications of the equation of states (EOS) have been proposed in the confined fluid simulation. Capillary pressure based on Young–Laplace equation is popular in the equilibrium simulation of vapor and liquid phases [39–42]. Some work has been done to improve the computation of capillary pressure by introducing an extra parameter [43] or the adsorption layer thickness [44]. However, inside shale nanopores, the interaction between molecules of boundaries and fluids contributes a significant impact on the distribution of fluid molecules and cannot be covered in these procedures above since the mechanism is different from the capillary pressure [4]. Another approach, by modifying the critical properties of fluid components, was conducted to determine the phase diagrams under confinement [42, 45–47]. Since this modification depends on molecular simulation data, it is limited to the database in which the molecular simulation conducted. Some new extensions of EOS are designed by considering the boundary–fluid interaction [48] or including the density function theory [38]. But the boundary material effect on phase behavior simulation is not fully considered. Furthermore, hysteresis is hard to describe based on EOS simulation.

Molecular simulation techniques have the advantages in the phase behavior simulation, especially the Monte Carlo (MC) methods [4, 5, 38, 49]. Based on the thermodynamic description of the interactions between molecular particles, the statistical method is suitable for describing molecular distributions in complex pore models without additional assumptions. Also, simulations of hysteresis and the interface are also available in the molecular simulation. The defect of a large simulation resource requirement could be reduced by parallel computation techniques. Various MC methods are developed for

simulations based on different ensembles [50, 51], such as the Canonical Monte Carlo (CMC) [52, 53], the Gibbs ensemble Monte Carlo (GEMC) [54–57], the grand canonical Monte Carlo (GCMC) [58–66], the gauge-GEMC [67–69] and gauge-GCMC [3, 16]. Detailed information about each method will be covered in chapter 2. Because of the applicability of Monte Calor molecular simulation in the study of the nanopore, it is chosen in this work to perform the simulation of confined phase behavior.

1.2 Thesis outline

In chapter 2, basic theories of Monte Carlo molecular simulation are introduced, including the Metropolis Monte Carlo and other methods on various ensembles.

In chapter 3, several details of the energy computation are explained, including the definition of the potential model, configurational bias Monte Carlo, the computation methods for chemical potential and system pressure, and the periodic boundary condition.

In chapter 4, fluid phase behavior is studied under confinement based on the slit pore model of graphite. Simulation cases include pure fluids, one binary fluid, and one ternary fluid. The accuracy of the new method, gauge-GCMC, is verified by comparing results with those of other Monte Carlo methods.

In chapter 5, pore size distribution effect is investigated on the methane phase behavior. Several cylinder pore models are employed, including single pore with different diameters, multiple pore model with various diameters and one simplified Eagle Ford case.

In chapter 6, to understand the phase behavior in different shale condition, confined phase behavior simulations are conducted for two pure fluids and one ternary fluid based on two types of nanopores which are generated from three kinds of materials.

In chapter 7, a summary is listed about the content in previous chapters and some possible research topics are described as future work.

2. METHODOLOGIES*

2.1 Metropolis Monte Carlo

Based on the classical statistical mechanics [58], the partition function Q of a system with a volume V and particle number N at a temperature T is expressed as:

$$Q = c \int d\mathbf{p}^N d\mathbf{r}^N exp[-H(\mathbf{r}^N, \mathbf{p}^N)/k_B T] \tag{2.1}$$

where k_B is the Boltzmann's constant, c is a proportionality constant. $\mathbf{p}^N$ and $\mathbf{r}^N$ are momenta and coordinates of the N particles, respectively. $H(\mathbf{r}^N \mathbf{p}^N)$ is the system Hamiltonian, $H = K + U$, where K is the kinetic energy and U is the potential energy. Usually, an observation A can be expressed on the basis of partition function:

$$< A >= \frac{\int d\mathbf{p}^N d\mathbf{r}^N A(\mathbf{r}^N, \mathbf{p}^N) exp[-\beta H(\mathbf{r}^N, \mathbf{p}^N)]}{\int d\mathbf{p}^N d\mathbf{r}^N exp[-\beta H(\mathbf{r}^N, \mathbf{p}^N)]} \tag{2.2}$$

here $\beta = 1/k_B T$. In the above calculation, the computation of $A(\mathbf{r}^N)$ is difficult. Only in some specific cases, there are analytical solutions for this multidimensional integration, and numerical approaches are necessary for all other situations. Since the particle number N could be a large value and most studies are conducted in the 3D condition, it is a daunting task to calculate the above average directly.

To improve the computation efficiency, the importance sampling setting for Monte Carlo technique was introduced by Metropolis et al. [70]. The average observation can be

*Part of the data reported in this chapter is reprinted with permission from "Phase behavior of multi-component hydrocarbon systems in nano-pores using gauge-GCMC molecular simulation" by Bikai Jin and Hadi Nasrabadi, 2016. *Fluid Phase Equilibria*, 425, 324-334, Copyright [2016] by Elsevier B.V.

simplified as following by ignoring the kinetic energy for the static system:

$$< A >= \frac{\int d\mathbf{r}^N A(\mathbf{r}^N) exp[-\beta U(\mathbf{r}^N)]}{\int d\mathbf{r}^N exp[-\beta U(\mathbf{r}^N)]} \tag{2.3}$$

here the probability density of the system in a configuration near $\mathbf{r}^N$ is denoted as follows:

$$N(\mathbf{r}^N) \equiv \frac{exp[-\beta U(\mathbf{r}^N)]}{\int d\mathbf{r}^N exp[-\beta U(\mathbf{r}^N)]} \tag{2.4}$$

then, when we have a lot of sampling point with a total number M in the configuration space,

$$< A >\approx \sum_{i=1}^{M} N(\mathbf{r_i}^N) A(\mathbf{r_i}^N) \tag{2.5}$$

Based on this equation, only the relative but not the absolute probabilities of points in the configuration space is required in the computation of average observations. And this procedure will greatly reduce the computation task as mentioned before because the Metropolis scheme will "deny" the points which are covered in the conventional calculation scheme and have a negligible contribution to the integration. The Metropolis scheme can be derived as follows.

Define the probability of transition from configuration o to n as $\pi(o \rightarrow n)$, and the probability of configuration o as $N(o)$. To satisfy the detailed balance condition, that in equilibrium state the average moves from configuration o to n should be exactly equal to the average of reverse moves, we have,

$$N(o)\pi(o \to n) = N(n)\pi(n \to o) \tag{2.6}$$

In a Monte Carlo move, the first stage is the generation of a trial move from state o to n with the probability $\alpha(o \to n)$, and the next stage is the decision to accept this move with an acceptance probability $acc(o \to n)$, then

$$\pi(o \to n) = \alpha(o \to n) * acc(o \to n) \tag{2.7}$$

in the Metropolis scheme, α is a symmetric matrix, that $\alpha(o \to n) = \alpha(n \to o)$. Then, we have

$$\frac{acc(o \to n)}{acc(n \to o)} = \frac{N(o)}{N(n)} = exp(-\beta[\mathcal{U}(n) - \mathcal{U}(o)]) \tag{2.8}$$

and the original choice of Metropolis for $acc(o \to n)$ is:

$$acc(o \to n) = \begin{cases} exp(-\beta[U(n) - U(o)]) & U(n) > U(o) \\ 1 & U(n) \leq U(o) \end{cases} \tag{2.9}$$

There are other possible strategies for $acc(o \to n)$, but the Metropolis scheme is the most popular choice and can provide a more efficient sampling of the configuration space than other solutions [58, 71]. To decide whether to accept or reject a trial move, a random number $Rand$ is generated from a uniform distribution in the interval $[0, 1]$. If $Rand < acc(o \to n)$, the trial move is accepted and rejected otherwise. This procedure guarantees the acceptance probability of a trail move equal to $acc(o \to n)$.

In the above section, the Metropolis method is one kind of Markov chain process, in which the new state only depends on the current state, but not the other states before. A random walk in the configuration space is generated in a way that each state at ($\mathbf{r}^N$) has a probability (proportional to $exp(-\beta U(\mathbf{r}^N))$) to be chosen. Usually, a basic Monte Carlo algorithm is designed as follows:

1. Randomly select an initial state o with the energy $U(o)$.
2. Generate a new state n with the energy $U(n)$ through a Monte Carlo move.
3. Accept the change if $Rand < acc(o \rightarrow n)$, reject otherwise.
4. Repeat the above process for millions Monte Carlo moves.

Usually, Monte Carlo method is used to compute the equilibrium properties of a classical many-body system, and there is a wide choice of ensembles for Monte Carlo simulations, such as canonical, grand canonical, isobaric-isothermal, and Gibbs ensemble. As explained above, the principal idea of these Monte Carlo methods is to generate a random walk in those regions of the configuration space that have a major contribution in the computation of ensemble averages. Next, detailed information will be covered about several Monte Carlo methods used in this work.

2.2 Canonical Monte Carlo

Canonical Monte Carlo (CMC), also called canonical NVT simulation, is one method for direct interfacial simulation [50, 58]. Usually, one box is set up for the system within two-phase region [72]. Molecular number (N), box volume (V) and temperature (T) are kept as constants during the simulation process. Several Monte Carlo moves (e.g. displacement, regrow) have been implied to make system equilibrium. If the initial setting (NVT) locates in the two-phase region, the system will spontaneously separate

into two phases by the creation of interface. Initial system configuration is important for phase separation. By setting two-phase regions close to the expected equilibrium state with interfaces, the system is easy to reach stable with different densities in each section [73–75]. As shown in Fig. 2.1, all molecules are put in the center region to form the initial expectation of liquid state, and two ends of the simulation box are empty to represent the gas state. At end of a simulation, most molecules stay in the center region with a high liquid density. Some molecules move into the two ends to form a gas state with low density.

CMC is the most straightforward method for phase equilibrium simulation because an explicit interface is included in the method setting. However, the CMC simulation encounters some uncertainty problems. Since the box volume is finite and phase space sampling is slow by shaking these phases, the density distribution has a strong fluctuation [76]. This density fluctuation leads to an unclear interface and uneven density distribution inside each phase. When the density difference between two phases is small, it is impossible to get a stable two-phase system. And for a large system, a major fraction of molecules locates near the interface and have properties that cannot be explained by fluid behavior in the bulk [50]. Even with these uncertainties, CMC simulation is still used to generate phase properties and to provide two phases co-existing configuration [52, 53].

2.3 Grand Canonical Monte Carlo

Grand Canonical Monte Carlo (GCMC) simulation, also known as μVT simulation described in [58, 59], has been applied in a lot of studies [60–66]. In a GCMC simulation, the chemical potential for each component (μ_i), temperature (T) and box volume (V) are fixed as input parameters, and the molecular number is modified through particle insertion

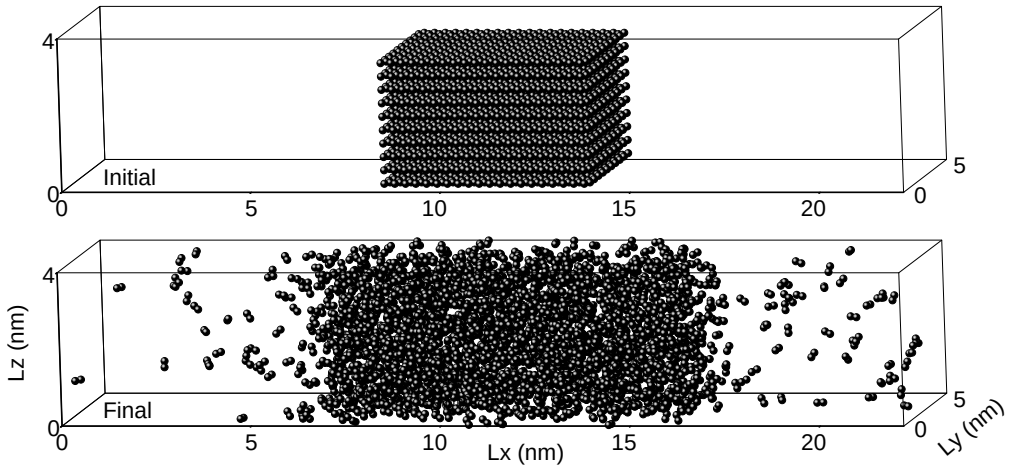

Solid lines stand for box dimensions, and spheres for molecules. Top is the initial configuration, bottom is the final configuration.

Figure 2.1: Schematic of Canonical NVT simulation in bulk

or deletion to meet the chemical potentials setting, as shown in Fig. 2.2. This setting is a mimic of the adsorption experiment in which the adsorbed gas is in equilibrium with the gas outside. The outside gas can be treated as a reservoir which imposes a chemical potential and temperature on the adsorbed gas [58].

Based on the statistical mechanical basis of the GCMC method, for a system of N interacting particles in volume V, the partition function is:

$$Q(\mu, V, T) = \sum_{N=0}^{\infty} \frac{exp(\beta\mu N)V^N}{\Lambda^{3N}N!} \int d\mathbf{r}^N exp[-\beta U(\mathbf{r}^N)] \tag{2.10}$$

where $\beta = 1/k_BT$, Λ is thermal de Broglie wavelength. The corresponding probability is:

$$\mathcal{N}_{\mu VT}(\mathbf{s}^N, N) \propto \frac{exp(\beta\mu NV^N)}{\Lambda^{3N}N!} exp[-\beta U(\mathbf{r}^N)] \tag{2.11}$$

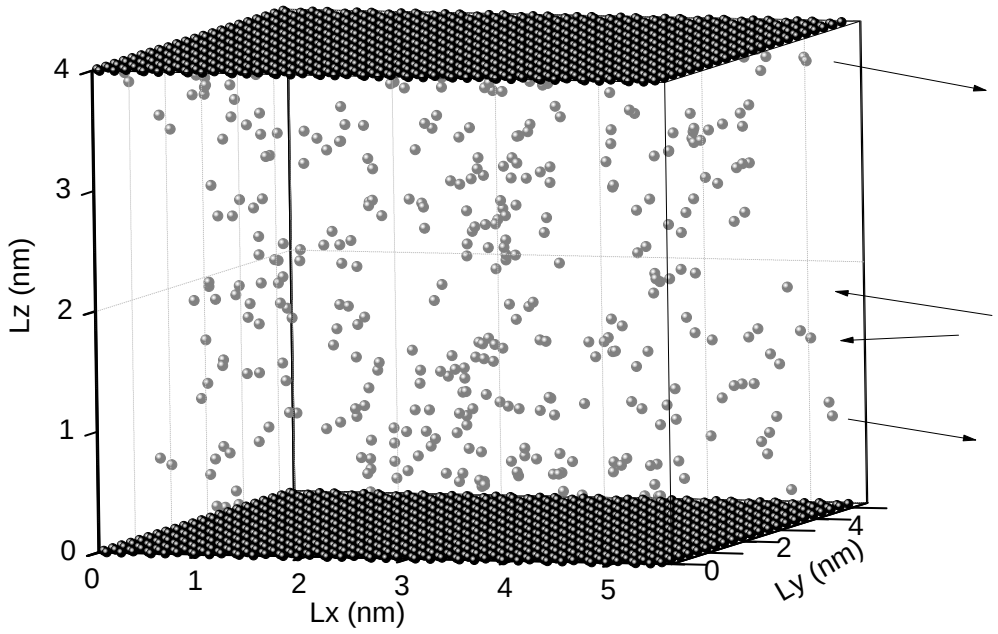

Arrows: particle insertion or deletion. Gray, black spheres: fluid molecules and pore boundary molecules. Solid lines: box dimensions. Reprinted from [3].

Figure 2.2: GCMC method schematic.

In a GCMC simulation, there are two kinds of Monte Carlo moves used to sample the distribution in (2.11):

1. Particle conformation change: Randomly select a particle ($\mathbf{r}^N$) and give it a new conformation ($\mathbf{r'}^N$) (e.g. displacement, rotation, partial regrow). This kind of move is accepted with the probability

$$acc(\mathbf{r}^N \rightarrow \mathbf{r'}^N) = min(1, exp[-\beta(U(\mathbf{r'}^N) - U(\mathbf{r}^N))]) \tag{2.12}$$

2. Particle insertion or deletion: A particle is randomly selected and deleted from the system with the probability

$$acc(N \rightarrow N-1) = min(1, \frac{\Lambda^{3N} N}{V} exp(-\beta[\mu + U(N-1) - U(N)])) \tag{2.13}$$

and the probability of the new particle insertion at a random position is

$$acc(N \rightarrow N+1) = min(1, \frac{V}{\Lambda^{3N}(N+1)} exp(\beta[\mu - U(N-1) + U(N)])) \tag{2.14}$$

For a GCMC simulation, the initial configuration is important to get proper final results. If the simulation box is empty or there is quite a small amount of molecules at the initial state, the adsorption isotherm will be generated through a series of tests with different chemical potentials, as shown in Fig. 2.3. If the simulation box is fully saturated or there a lot of molecules at the beginning state, the desorption isotherm will be produced by increasing the chemical potential inputs in a series of tests. The separation between these isotherms results in the hysteresis [23, 50, 77], in which the state of a system depends on its generation history and the adsorption/desorption processes is not reversible. Apparently, the phase transition properties are not direct outputs of the GCMC simulation, since there are multiple possible solutions to the phase transition on the hysteresis diagrams (Fig. 2.3). According to Peterson and Gubbins [78], the phase transition point can be identified based on another extra simulation at the supercritical temperature. However, the details of this method will not be covered here since another approach, the histogram reweighting method [79–83], is adopted in this work and will be explained in the next section.

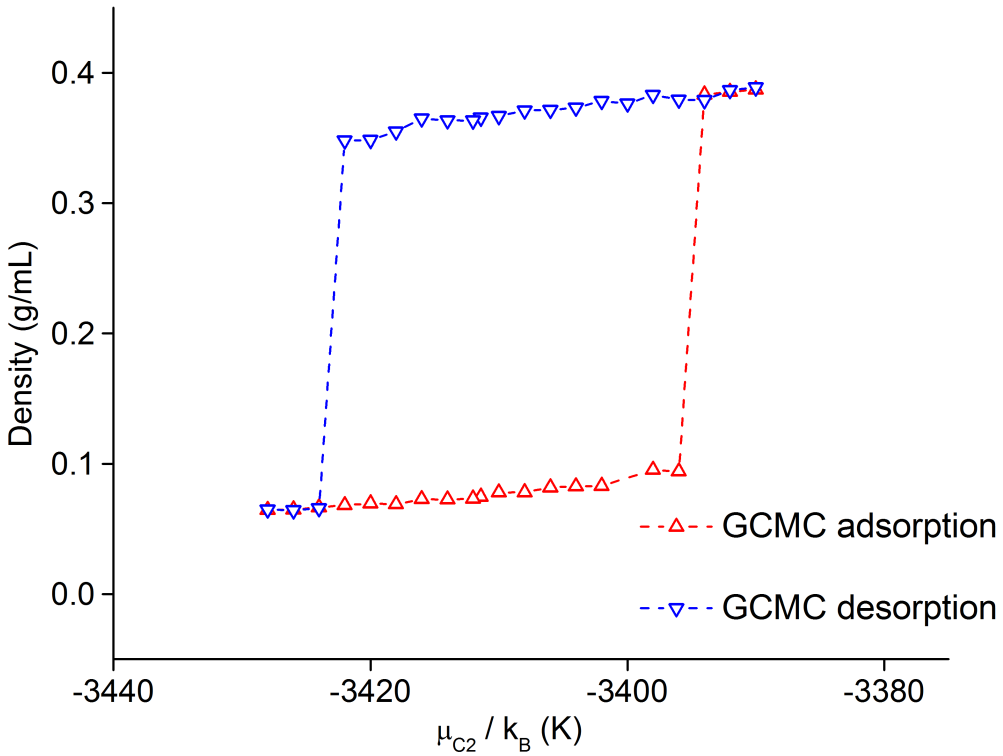

C_1: methane, C_2: ethane. $\mu_{C_1}/k_B = -3300\ K$

Figure 2.3: $\mu_{C_2}/k_B - \rho$ diagram of C_1/C_2 fluid at 273.15 K in bulk.

For a system of i components and $(N_1, N_2, ...N_i)$ particles in the simulation box with configurational energy of E, the histogram reweighting method requires the collection of probability distribution $f(N_1, N_2, ..., N_i, E)$,

$$f(N_1, N_2, ..., N_i, E) = \frac{\Omega(N_1, N_2, ..., N_i, E, V) exp(-\beta E + \beta(\mu_1 N_1 + \mu_2 N_2 + ... + \mu_i N_i))}{\Xi(\mu_1, \mu_2, ..., \mu_i, V, \beta)} \tag{2.15}$$

where $\beta = 1/k_B T$. $\Omega(N_1, N_2, ..., N_i, E, V)$ is the microcanonical partition function and $\Xi(\mu_1, \mu_2, ..., \mu_i, V, \beta)$ is the grand partition function,

$$\Xi(\mu_1, \mu_2, ..., \mu_i, V, \beta) = \sum_{N_1, N_2, ..., N_i} \frac{1}{\Lambda_1^{3N_1} N_1!} \frac{1}{\Lambda_2^{3N_2} N_2!} ... \frac{1}{\Lambda_i^{3N_i} N_i!} exp(\beta(\mu_1 N_1 + \mu_2 N_2 + ... + \mu_i N_i)) \int d\mathbf{r}^N exp(-\beta E(N)) \tag{2.16}$$

where $N = N_1 + N_2 + ... + N_i$ and $E(N)$ is the system configurational energy. Actually, this probability distribution $f(N_1, N_2, ..., N_i, E)$ can be recorded during the simulation. Then, the entropy $S(E, V, N)$ can be produced as follows:

$$S(E, V, N_1, N_2, ..., N_i)/k_B = ln\Omega(N_1, N_2, ..., N_i, E, V) = lnf(N_1, N_2, ..., N_i, E) + \beta E - \beta(\mu_1 N_1 + \mu_2 N_2 + ... + \mu_i N_i) + C \tag{2.17}$$

where C is a constant. If several simulations at different temperatures and chemical potentials have an overlap region in the space of $(N_1, N_2, ..., N_i, E)$, these entropy functions can be merged by "shifting" to an identical form in the overlap region, and a global function will be generated with a wide coverage in the space $(N_1, N_2, ..., N_i, E)$. To determine the optimal strategy for merging these raw data, Ferrenberg and Swendsen [79–81] proposed a solution by minimizing the divergence between the recorded and predicted histograms. If there are R overlapped simulations for a specific system, the probability, $\mathcal{P}(N, E; \mu, \beta)$, of observing N particles and energy E is,

$$\mathcal{P}(N, E; \mu, \beta) = (\sum_{i=1}^{R} f_i(N, E) exp(-\beta E + \beta \mu N))/(\sum_{i=1}^{R} K_i exp(-\beta_i E + \beta_i \mu_i N - C_i)) \tag{2.18}$$

here $K_i = \sum_{N,E} f_i(N, E)$, and K_i is the number of total records for simulation i. The constant C_i is calculated through iteration,

$$exp(C_i) = \sum_E \sum_N \mathcal{P}(N, E; \mu, \beta) \tag{2.19}$$

With an initial guess of the weights C_i, equations (2.18) and (2.19) can be solved after the integration gets converged. Based on these histogram records from i simulations, the thermodynamic properties of the system located in the coverage of the merged histograms can be computed without extra simulations. For instance, the average density is,

$$< \rho >_{\mu,\beta} = \frac{1}{V} \sum_E \sum_N \mathcal{P}(N, E; \mu, \beta) N \tag{2.20}$$

In practice, it is prohibitive to generate 3D histograms since the covered region of the phase space is pretty large in a simulation. Instead, most work based on GCMC are focus on simple systems (1D or 2D) [60–66]. If one simulation is conducted near the phase transition region, then the system should sample states on each side of the phase transition, leading to a histogram with multiple peaks. As shown in Fig 2.4, there are two states sampled in the simulation, one at small and another one at a large particle number, corresponding to the gas and liquid phase.

Based on the above bimodal distribution of the histogram record, one approach [50,58] is proposed to generate the phase diagram from only several GCMC simulations by providing a connection between states through a near-critical path. As illustrated in Fig. 2.5, a simulation is performed at $T = 303\ K$ and $\mu/k_B = -3690\ K$, in which the histogram covers a big range of density in both gas and liquid phases. The average density for this run is indicated by a blue triangle. Since this test is close to the critical point, the histogram has a wide coverage of the system density and is reweighted to generate the properties at lower temperatures ($T = 300\ K$). Then the estimated chemical

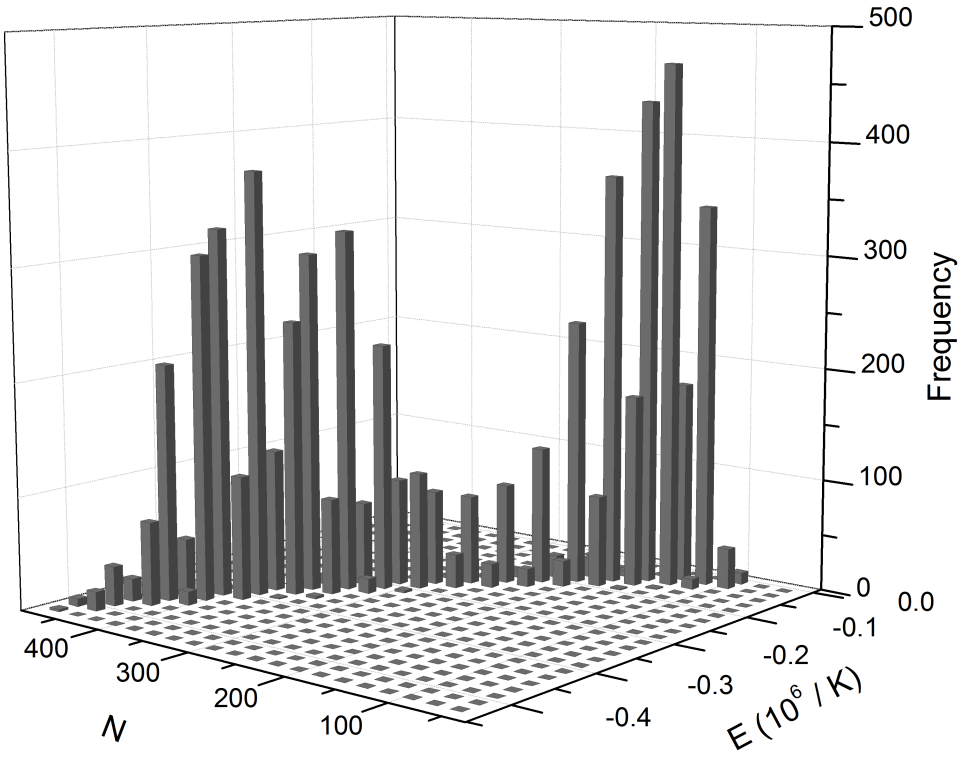

$T = 303\ K$, $\mu/k_B = -3690\ K$. E: system energy in unit of K. N: molecular number.

Figure 2.4: Frequency of state observations from GCMC test of ethane.

potential at 300 K is used as the input of new simulations, which sample states near the saturated liquid and gas lines, indicated as solid lines. The new histograms from these two simulations can combine with previous one to generate a new estimation of properties at the lower temperature (e.g. $290\ K$). By repeating the above procedure, the diagram will be calculated through limited simulations. The key point of this method is that the estimated properties should locate in the sampling range of previously combined histograms.

Note that the above method cannot extend to the temperature higher than the one near the critical point (304 K in the above example). Following the principle of critical

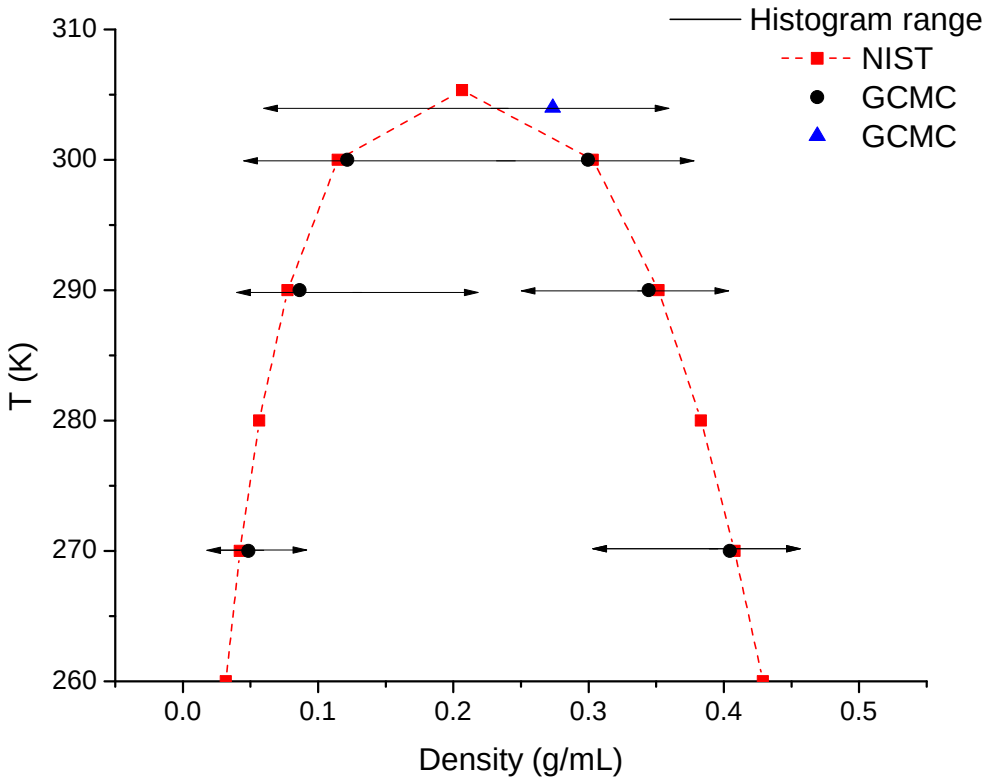

Red square: theoretical data from NIST. Black circle: GCMC histogram reweighting results. Blue triangle: GCMC test near the critical point. Solid arrow: the density range sampled of each histogram.

Figure 2.5: Phase diagram of ethane.

point universality [84], that the fluid critical behavior is in the same universality class as the Ising model [85], the apparent critical parameters can be determined as shown in Fig. 2.6. The histogram record is adjusted to provide the best fit between the normalized probability distribution $P_L(x)$ of the ordering operator x and the universal distribution at the criticality. After the adjustment, the critical value in an infinite system is scaled from the apparent critical parameters following finite-size corrections [50,86,87].

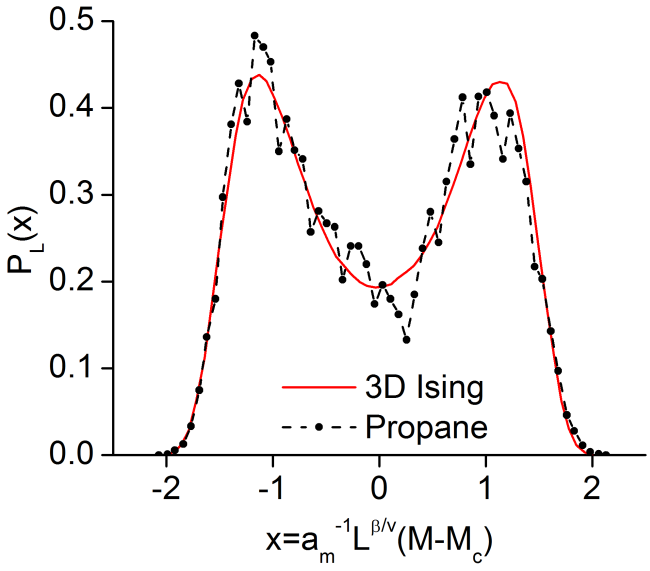

Solid line: 3D Ising universality class. Black symbols: results in bulk.

Figure 2.6: Ordering operator distribution of propane at critical point in bulk.

2.4 Gibbs Ensemble Monte Carlo

Gibbs Ensemble Monte Carlo method, also named by the initials GEMC, is a technique designed for direct simulation of phase equilibrium in fluids [50, 54, 88]. Even though this method is not used in this work, we should understand it first because the other two methods below are developed from GEMC. A schematic of GEMC is shown in Fig. 2.7. Two boxes are employed in the simulation to represent two phases. The requirements for phase coexisting are that the temperature T, pressure P, the chemical potential of each component μ_i should be the same in two boxes and each phase should be internal equilibrium.

The GEMC setting is the canonical ensemble for the total system of two boxes (Fig. 2.7), in which total volume V, total molecular number N and temperature T are constant.

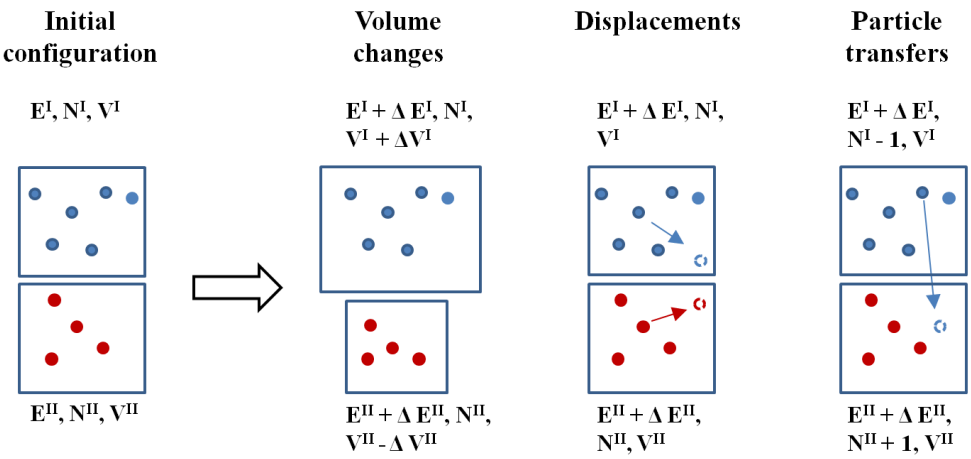

Figure 2.7: A schematic of GEMC method in one-component system.

Then we have $\Delta V_1 = \Delta(V - V_2) = -\Delta V_2$, $\Delta N_1 = \Delta(N - N_2) = -\Delta N_2$. For a one-component system, the partition function is

$$Q_{NVT} = \frac{1}{\Lambda^{3N} N!} \sum_{N_1=0}^{N} \binom{N}{N_1} \int_0^V dV_1 V_1^{N_1} V_2^{N_2} \int d\xi_1^{N_1} exp[-\beta U_1(N_1)] \\ * \int d\xi_2^{N_2} exp[-\beta U_2(N_2)] \tag{2.21}$$

where ξ_1 and ξ_2 are the coordinates of particles in these two boxes, and the corresponding probability density function is

$$\mathcal{P}(N_1, V_1; N, V, T) \propto \frac{N!}{N_1!\, N_2!} exp[N_1 ln V_1 + N_2 ln V_2 - \beta U_1(N_1) - \beta U_2(N_2)] \tag{2.22}$$

Usually, in GEMC simulation there are three kinds of Monte Carlo moves, displacement, volume change, and particle transfer. For a displacement move in one of the two boxes, the acceptance probability is

$$\mathcal{P}_{displace} = min[1, exp(-\beta \Delta U)] \tag{2.23}$$

For a volume change move, in which V_1 is increased by ΔV_1,

$$\mathcal{P}_{volume} = min[1, exp(-\beta\Delta U_1 - \beta\Delta U_2 + N_1 ln\frac{V_1 + \Delta V}{V_1} + N_2 ln\frac{V_2 - \Delta V}{V_2})] \quad (2.24)$$

For a particle transfer move from box 2 to box 1,

$$\mathcal{P}_{trans} = min[1, \frac{N_2 V_1}{(N_1 + 1)V_2} exp(-\beta\Delta U_1 - \beta\Delta U_2)] \quad (2.25)$$

All equations are suitable for phase coexisting simulation of pure fluids at the temperature lower than critical point. However, for multicomponent systems, the GEMC setting should be considered as NPT [55, 89], in which the total molecular number, external pressure, and temperature are constants. The volume changes in the two boxes are performed independently. Since the GEMC method with NPT setting is not used in this work, no more details will be covered. To investigate the phase behavior under confinement, pore-pore GEMC method is proposed that the confinement effect is applied as an external force in the two boxes based on GEMC method with NVT setting [56]. In the practice, this pore-pore GEMC is used for the capillary condensation coexistence simulation in the nanopores [67]. But the coexistence point determination depends on the initial configuration, which limits the usage of this method. To have a deep understanding of capillary condensation phenomena, Neimark and Vishnyakov [67] developed the Gauge-GEMC method, which will be covered in the following section.

2.5 Gauge-GEMC

To study the fluid phase equilibrium in confined systems, Gauge-GEMC method is developed from the original GEMC technique [67, 68]. Two simulation boxes are employed in this method, including one fluids system box and one gauge meter which usually has a limited volume (Fig. 2.8).

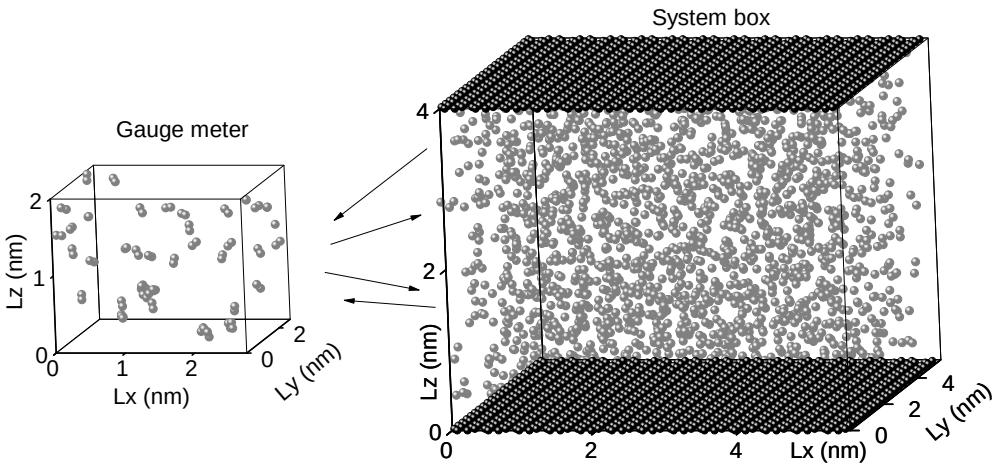

Gray, black spheres: fluid molecules and pore boundary molecules. Arrows: Monte Carlo move of particle transfer.Solid lines: box dimensions. Reprinted from [3].

Figure 2.8: Gauge-GEMC method schematic.

Since the volume of gauge meter is finite, it limits the density change in the fluid system box and allows the system to remain in any state, such as unstable state which is hard to reach from other methods. In this Gibbs ensemble setting, the total Helmholtz free energy in two boxes is minimized:

$$F_f(N_f, V_f, T) + F_g(N_g, V_g, T) \rightarrow min \tag{2.26}$$

when the temperature T, total molecular number N and volume of each box (V_f, V_g) are kept as constants,

$$N_f + N_g = const, V_f, V_g, T = const \tag{2.27}$$

where F is the Helmholtz free energy, g represents the gauge box, and f indicates the fluid box.

There are several kinds Monte Carlo moves used in this method, including particle transfer, regrow and displacement. No volume change is allowed during the simulation. This method allows one to construct a van der Waals shape (or S-shape) phase diagram, which consists of stable, metastable, and unstable states [67] (Fig. 2.9). Through a set of simulation tests by increasing the total molecular numbers, the μ-ρ relationship of a pure fluid is generated. Based on the Maxwell equal area rule [90], the phase equilibrium points are calculated through thermodynamic integration in the unstable and metastable regions,

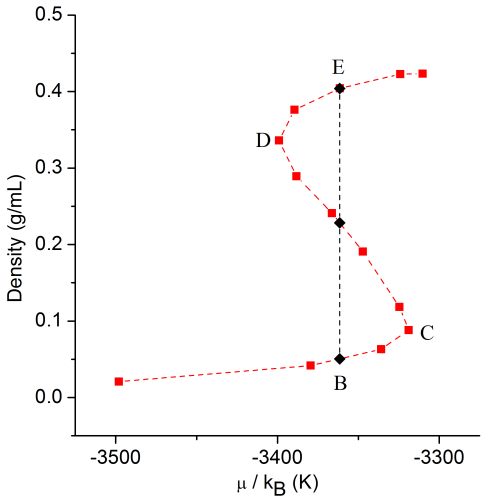

Square: results at 270 K. Diamond: equilibrium points. Reprinted from [16].

Figure 2.9: μ/k_B-ρ diagrams of a pure ethane system in bulk.

$$\int_B^C \rho d\mu + \int_C^D \rho d\mu + \int_D^E \rho d\mu = 0 \tag{2.28}$$

Like the GEMC method, gauge-GEMC is suitable for phase equilibrium simulation at

the temperature lower than the critical point. When getting close to the critical point, the density differences between phases is decreasing and the S-shaped isotherm gets unclear. Thus, the critical point properties (ρ_c, T_c) can only be extrapolated from the results at the lower temperature based on the law of rectilinear diameter [91] and the scaling law for density [92]:

$$\frac{\rho_L + \rho_G}{2} = \rho_c + C(T_c - T) \tag{2.29}$$

$$\rho_L - \rho_G = A(T_c - T)^\beta \tag{2.30}$$

By employing more boxes, this method is extended to multicomponent systems [69]. For an N component fluid, the simulation needs $N + 1$ boxes — one main box for the fluid system plus N separated gauge meters — while molecules of component i are only transferred between the gauge box i and the main box. No particle transfer is allowed between gauge boxes. Each gauge box only contains molecules of one component and serves as the properties meter of this given component in the main box.

Since the gauge-GEMC method is developed under the NVT setting, the $\mu - \rho$ relationship is not a straightforward output of the simulation. For example, a series of tests are conducted with different molecular numbers in the C_1/C_2 system. As shown in Fig. 2.10, by keeping the mole fraction as the same ($C_1\% = 20\%$), the system samples the configuration space along the curve when the total molecular number changes. It is clear that only one set of tests cannot provide enough information about phase equilibrium properties. By repeating the above tests at different mole fraction settings of C_1, we can have dense sampling points in the configuration space. The $\mu_{C_2} - \rho$ relationship can

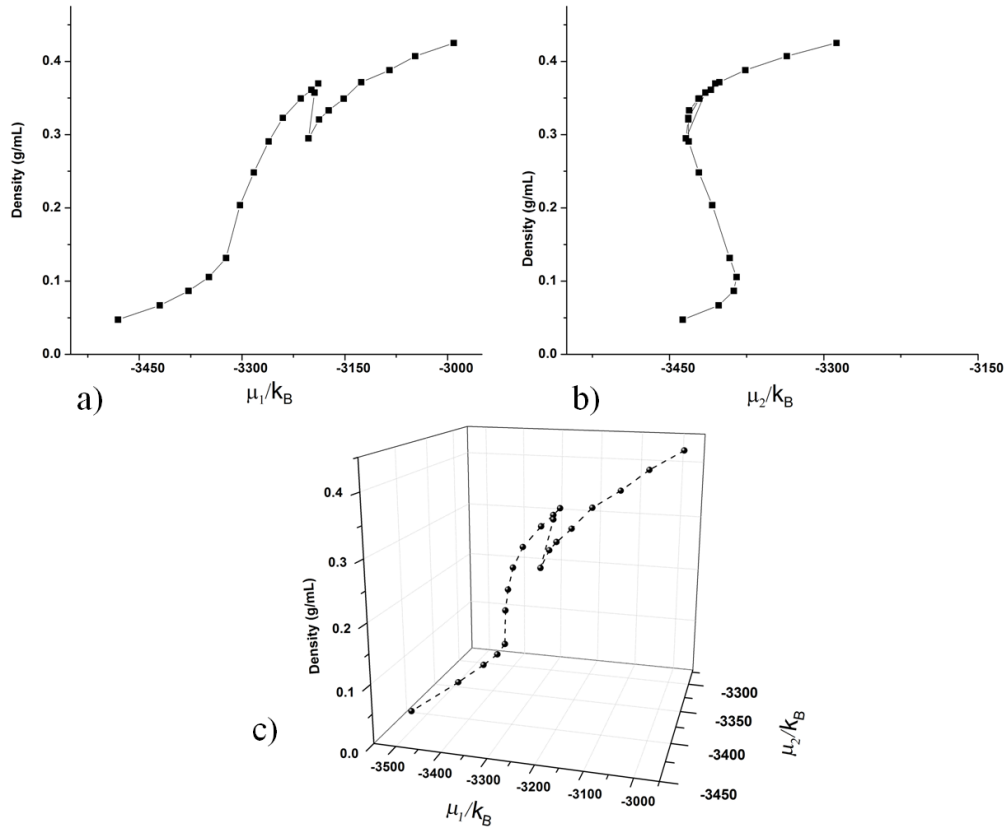

a) μ_1/k_B-ρ view, b) μ_2/k_B-ρ view, c) 3D view.

Figure 2.10: μ_1/k_B-μ_2/k_B-ρ diagrams of a C_1/C_2 system in bulk at 273.15 K.

be interpolated as some given values of μ_{C_1} and the Maxwell equal area rule is used to computed the properties at equilibrium.

The usage of gauge-GEMC method is limited to simple fluids, such as pure and binary fluids. For example, to get the phase equilibrium diagrams of a C_1/C_3/C_{nC_5} system, a set of simulations are conducted by maintaining the inputs (N_{C_1}, N_{C_3}) and increasing the N_{nC_5}. To repeat the set tests by modifying the inputs (N_{C_1}, N_{C_3}) to other values, the sampling points are generated in the configuration space (μ_{C_1}, μ_{C_3}, μ_{nC_5}, ρ). However, it is extremely hard to interpolation the $\mu_{nC_5} - \rho$ relationship at some givens state in which

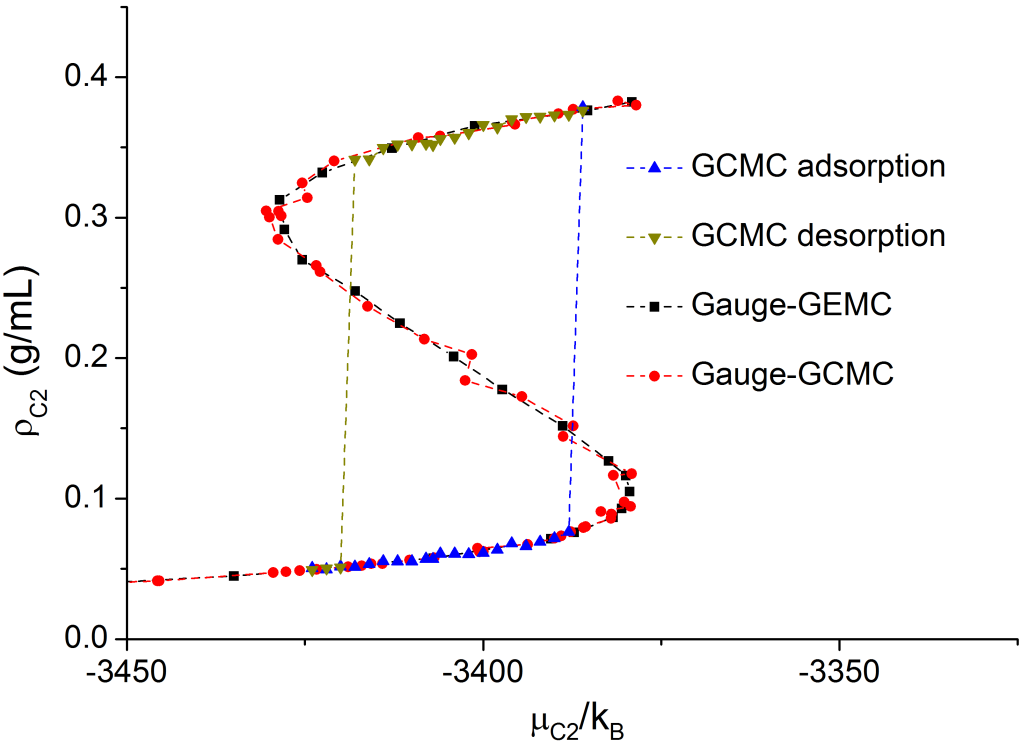

$T = 273.15\ K, \mu_1/k_B = -3400\ K.$

Figure 2.11: μ_2/k_B-ρ diagrams of a C_1/C_2 system in bulk.

$(\mu_{C_1}, \mu_{C_3})_{gas} = (\mu_{C_1}, \mu_{C_3})_{liquid}$. Therefore, the gauge-GEMC method is suggested for the simulation of simple fluids but not the ternary or multiple component fluids.

2.6 Gauge-GCMC

To expand the usage of gauge-GEMC method and keep its feature of generating van der Waals loop, a new method, named gauge-GCMC, is proposed for the simulation of multicomponent fluids under confinement by upgrading the two-box setting gauge-GEMC method with the feature of GCMC technique [3]. The two-box setting is still adopted in the gauge-GCMC method and several Monte Carlo moves (e.g. displacement, regrow and

transfer) are used to get the equilibrium inside each box and between two boxes. The calculation of chemical potentials follows the same procedure as in gauge-GEMC method. In the gauge meter, an extra Monte Carlo move, as used in GCMC method, is introduced for molecule insertion and deletion. As shown in Fig. 2.11, there is an excellent match between the results of gauge-GCMC, gauge-GEMC, and GCMC. For a fluid system with M components, the chemical potentials (μ_1, μ_2, ..., μ_{M-1}), box volume (V), system temperature (T), and the molecular number (N_M) of component M are set as constant inputs.

The simulation process is described based on the example of a C_1/C_3/nC_5 system as follows. In each simulation case, the parameters (μ_{C_1}, μ_{C_3}, N_{nC_5}, T, V) are set as constants. Molecule numbers (N_{C_1}, N_{C_3}) are changed by insertion or deletion so that the calculated chemical potential can meet the input constants in the system. The displacement and regrow Monte Carlo moves are used to get the internal equilibrium in each box. The molecules of each component are transferred between boxes to make the chemical potentials in both boxes equal to each other ($\mu_{C_i,fluid} = \mu_{C_i,gauge}$). While keeping other parameters as constants but increasing N_{nC_5} values, a set of tests are performed to provide the μ_{nC_5}-ρ relationship in the S-shape. Fluid densities at equilibrium are calculated based on the Maxwell equal area rule [90]. The difference between these two "gauge" methods is displayed in the flowcharts (Fig. 2.13). The change in the constant setting makes it possible to get the $\mu - \rho$ relationship in complex fluids. After repeating the above tests at other combinations of (μ_{C_1}, μ_{C_3}), additional equilibrium densities are generated to form the 3D phase diagram for this ternary system. If there is only one component fluid in the system ($M = 1$), the gauge-GCMC simulation is exactly equal to the gauge-GEMC method.

For a clear understanding of the computation efficiency, the gauge-GCMC is compared with the GCMC method. To get the phase equilibrium properties of single fluids or a complex system, only a dozen tests of gauge-GCMC are necessary for the simulation, but a lot of tests of GCMC are needed to build the isotherms. Even GCMC is faster in a single test, gauge-GCMC method is more suitable for simulation in multicomponent fluids considering the total computational cost.

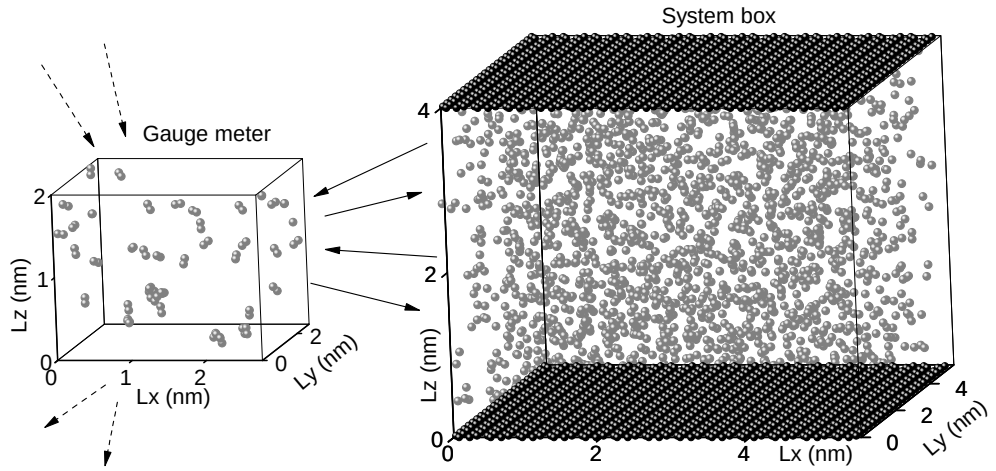

Solid, dashed arrows: transfer move and insertion/deletion move. Gray, black spheres: fluid molecules and boundary molecules. Solid lines: box dimensions. Reprinted from [3].

Figure 2.12: Gauge-GCMC method schematic.

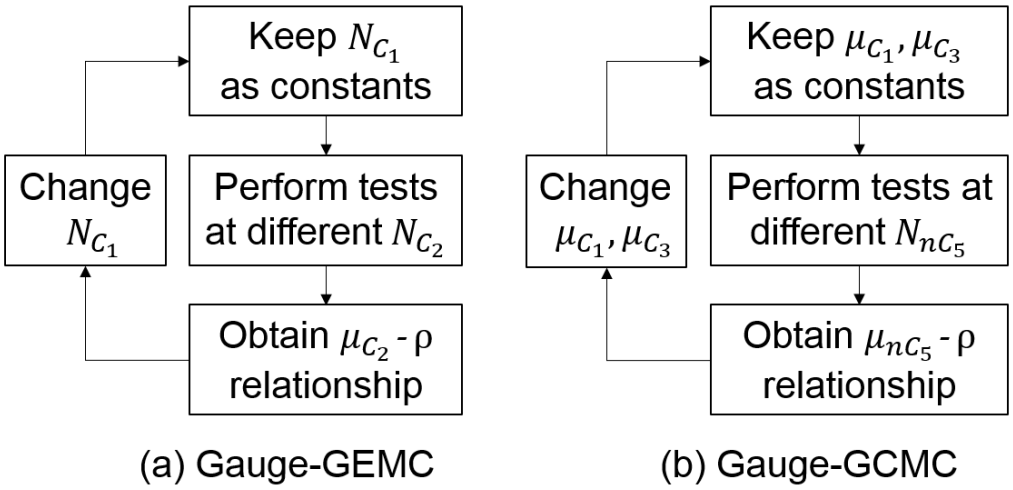

(a) Gauge-GEMC method for a binary system, (b) Gauge-GCMC method for a ternary system. Reprinted from [3].

Figure 2.13: Flowcharts of gauge-GCMC and gauge-GEMC.

3. SIMULATION DETAILS

3.1 Potential models

In a classical simulation work [71], only intermolecular interactions (nonbonded term) and intramolecular interactions (bonded, bending angles, dihedral angles, improper torsion, and intramolecular nonbonded terms) are considered in the potential energy calculation and the quantum effects are ignored.

$$\begin{aligned} U(\mathbf{r}^N) = &\sum_{i\neq j} U_{nonbond}(\mathbf{r_i}, \mathbf{r_j}) + \sum_{i\neq j} U_{bond}(\mathbf{r_i}, \mathbf{r_j}) + \sum_{i\neq j\neq k} U_{bend}(\mathbf{r_i}, \mathbf{r_j}, \mathbf{r_k}) \\ &+ \sum_{i\neq j\neq k\neq l} U_{tor}(\mathbf{r_i}, \mathbf{r_j}, \mathbf{r_k}, \mathbf{r_l}) + \sum_{i\neq j\neq k\neq l} U_{imp}(\mathbf{r_i}, \mathbf{r_j}, \mathbf{r_k}, \mathbf{r_l}) \end{aligned} \tag{3.1}$$

where $\mathbf{r}^N$ is the coordinates of all N particles, and $\mathbf{r_i}, \mathbf{r_j}$ are the coordinates of particle i and j, respectively. Here, one molecule could consist of several particles.

In the calculation of intermolecular interactions under real situations, the three-body forces have a large contribution to the configurational energy of a condensed phase [88, 93]. However, it is prohibitively expensive in the computational cost by using explicit three-body forces in the simulations. Thus, it is a common procedure to adopt simplified potential models that are effective pair-wise additive [88]. These potentials do not stand for the actual forces between a pair of molecules in the vacuum, but they are sufficient in the calculation of configuration energy since the three-body forces are incorporated in these models. In this work, the Lennard–Jones (LJ) potential is used to calculate the intermolecular interaction energy:

$$U_{nonbond}(\mathbf{r_i}, \mathbf{r_j}) = \begin{cases} 4\varepsilon_{ij}[(\frac{\sigma_{ij}}{r_{ij}})^{12} - (\frac{\sigma_{ij}}{r_{ij}})^{6}] & r_{ij} < r_{cutoff} \\ 0 & r_{ij} \geq r_{cutoff} \end{cases} \tag{3.2}$$

where $U_{nonbond}(\mathbf{r_i}, \mathbf{r_j})$ is the configurational potential between particles (i, j) located at a distance r_{ij}. ε_{ij} is the potential well depth, and σ_{ij} is the distance parameter where $U = 0$, r_{cutoff} is the cutoff distance. Since no partial charge is considered in hydrocarbon fluids, no electric potential is calculated in the following sections.

If the intermolecular potential is not rigorously zero beyond the cutoff distance, the truncation of the energy calculation at r_{cutoff} will result in a system error. Thus, the tail correction is considered in the energy computation [71]:

$$U_{tail} = \sum_{i=1}^{n} \sum_{j=1}^{n} \frac{N_i N_j R}{V} \tag{3.3}$$

$$R = 2\pi \int_{r_{cutoff}}^{\infty} r^2 U(r) dr \tag{3.4}$$

where R is the parameter from long-range corrections to calculate the van der Waals tail corrections, n is the number of components, N_i and N_j are the molecular numbers of component i and j, respectively.

The parameters of hydrocarbon particles (Table 1) for the LJ potential are provided from the TraPPE-UA force field [94]. The parameters for cross potential between unlike particles are calculated from Lorentz–Berthelot combining rules [95, 96], as follows,

Table 3.1: Parameters for LJ potential from TraPPE-UA force field

	CH_4	CH_3-	$-CH_2-$	aromatic carbon
ε/k_B [K]	148.0	98.0	46.0	30.0
σ [nm]	0.373	0.375	0.395	0.370

$$\sigma_{ij} = \frac{\sigma_{ii} + \sigma_{jj}}{2} \tag{3.5}$$

$$\varepsilon_{ij} = \sqrt{\varepsilon_{ii}\varepsilon_{jj}} \tag{3.6}$$

For intramolecular interactions, U_{bond} represents the vibration around the equilibrium bond length between particle i and j,

$$U_{bond}(\mathbf{r_i}, \mathbf{r_j}) = K_b(r_{ij} - r_0)^2 \tag{3.7}$$

where K_b and r_0 are the oscillation parameter and the equilibrium bond length. Since this work is focused on hydrocarbon fluids, the bond length is fixed at 0.154 nm and no vibration potential is included in the calculation. Bond bending potential U_{bend} denotes the potential energy between two bonds sharing one common atom and is computed as the standard harmonic-shape potential [97] in this work,

$$U_{bond}(\mathbf{r_i}, \mathbf{r_j}) = K_\theta(\theta - \theta_0)^2 \tag{3.8}$$

where θ is the bending angle, θ_0 is the corresponding equilibrium angle defined as $114°$, and $K_\theta = 31250\ K/rad^2$ for hydrocarbons. There are two kinds of torsion potentials, the dihedral angle potential and the improper torsion. Both potentials depend on four bonded atoms. The first one is also called the torsion potential $U_{tor}(\mathbf{r_i}, \mathbf{r_j}, \mathbf{r_k}, \mathbf{r_l})$, which describes the dihedral angle potential between bonds of four consecutive atoms. In this work, U_{tor} is computed from OPLS united atom cosine series [98],

$$U_{tor} = K_0 + K_1(1 + cos\phi) + K_2(1 - cos2\phi) + K_3(1 + cos3\phi) \tag{3.9}$$

where ϕ is the torsional angle, also the dihedral angle. $K_0 = 0, K_1 = 355K, K_2 =$

$-68.2K, K_3 = 791.3K$. The improper torsion potential also depends on four atoms, in which three of them centers around the fourth atom. The improper torsional angle is defined as the dihedral angle between two planes, one consists of the center atom and other two atoms, another one consists of all surrounding three atoms. The function form is given as,

$$U_{imp}(\mathbf{r_i}, \mathbf{r_j}, \mathbf{r_k}, \mathbf{r_l}) = K_{ijkl}(\phi - \phi_0)^2 \tag{3.10}$$

where K_{ijkl} and ϕ_0 are the improper torsion parameter and the equilibrium dihedral angle. Since only hydrocarbon fluids are studied in this work, this potential is set as zero in the calculation. The intramolecular nonbonded potential is only considered for atoms separated by three bonds in the same molecule following the equation (3.2). For atoms separated by more than three bonds, there is no calculation about the interaction energy.

3.2 Configurational bias Monte Carlo

In the history of the development of Monte Carlo molecular simulations, the methods' usage was limited to simple fluids since the prohibitively low acceptance of molecular moves [50]. For a dense phase, it was nearly impossible to add an extra large molecule inside the simulation box. To improve the sampling efficiency in the configuration space during the simulation, the configurational bias Monte Carlo (CBMC) was proposed and reviewed in detail by [58, 99]. Here, only the general concept of CBMC will be covered.

In the CBMC method, a multisegment molecule is inserted, removed or transferred segment-by-segment in the simulation box. Thus a molecule consisting of n_{step} segments will take n_{step} for the CBMC process. Several trial positions $\mathbf{r_i}$ are attempted for each segment movement based on the arbitrary distribution $P^{arb}_{trial}(\mathbf{r}_i)$ [100]. One specific

position is chosen for the growth of step k during the CBMC process according to the selection probability,

$$P_{select}(\mathbf{r_i}) = \frac{[P_{trial}^{ideal}(\mathbf{r}_i)/P_{trial}^{arb}(\mathbf{r}_i)]exp[-\beta U(\mathbf{r_i})]}{W_k} \tag{3.11}$$

where $U(\mathbf{r_i})$ is the energy at the trial position, $P_{trial}^{ideal}(\mathbf{r}_i)$ is the probability distribution of a trial position for an ideal system, in which $U(\mathbf{r_i}) = 0$ for all $\mathbf{r_i}$. W_k is the Rosenbluth weight of step k,

$$W_k = \sum_{j=1}^{n_{trial}^k} \frac{P_{trial}^{ideal}(\mathbf{r}_j)}{P_{trial}^{arb}(\mathbf{r}_j)} exp[-\beta U(\mathbf{r_j})] \tag{3.12}$$

where n_{trial}^k is the number of trial positions during step k of the CBMC procedure. A full CBMC process consisting of n_{step} segments will be accepted based on the following probability,

$$P_{accept} = min(1, \frac{\prod_{k=1}^{n_{step}} W_k^{new}}{\prod_{k=1}^{n_{step}} W_k^{old}}) \tag{3.13}$$

where the new Rosenbluth weight is calculated by randomly selecting a trial position during each growth step, while the old Rosenbluth weight is computed by setting the trial position at the old site in each step.

3.3 Chemical potential

The chemical potential is calculated through the insertion of molecules which depends on the average Rosenbluth weight during the insertion of an additional molecule in the simulation box,

$$\mu_{insert} = -k_B T ln[< \prod_{k=1}^{n_{step}} W_k^{new} >] \tag{3.14}$$

where $<>$ represents the value of inside variables after an ensemble average. The total chemical potential is a combination of the insertion chemical potential and another number density term, including all the inter- and intra-molecular interactions [101],

$$\mu_i = -k_B T ln[< \frac{WV}{(N_i + 1){\Lambda_i}^3} >] \tag{3.15}$$

where k_B is the Boltzmann's constant, T is temperature, V is the simulation box volume, N_i is the molecular number of component i, W is the Rosenbluth weight shown before, and Λ_i is the thermal de Broglie wavelength for component i. Based on equation (3.14), the computation of $u(\mathbf{r}_j)$ depends on the interactions between all molecules inside the simulation box, as mentioned in the above section.

3.4 Pressure

As expressed in detail in chapter 2 of [71], the pressure is computed based on the molecular virial that the stress tensor depends on the intermolecular pair forces of the system [71, 101]:

$$PV = Nk_B T + W \tag{3.16}$$

$$W = \frac{1}{3} \sum\nolimits_i \sum\nolimits_{j>i} w(\mathbf{r}_{ij}) \tag{3.17}$$

$$w(\mathbf{r}_{ij}) = \sum\nolimits_a \sum\nolimits_b \frac{w_{ab}(\mathbf{r}_{ab}) \mathbf{r}_{ab} \mathbf{r}_{ij}}{{\mathbf{r}_{ab}}^2} \tag{3.18}$$

where, P is the system pressure, V is the system volume, N is the molecular number, T is the temperature, W is the internal virial, $\mathbf{r}_{ij}$ is the vector between the molecular mass center i and j, $\mathbf{r}_{ab}$ is the vector between sites a and b, $w_{ab}(\mathbf{r}_{ab})$ is the virial function between two sites, and a and b are the specific atoms in each molecule. Since no partial charge is considered for hydrocarbon molecules in following chapters, w_{ab} will have the same value as the LJ potential.

As shown above, the pressure is a function of the molecular distribution inside the simulation box. This function has been proved valid in the bulk situations and can generate a stress tensor with the same principle values, which agrees with the homogeneous assumption of molecular distribution in bulk. However, since the existence of pore boundary, the molecular distribution is heterogeneous inside nanopores, which will be discussed in following chapters, and the stress tensor contains different principal values. Thus, if this method is used in the pressure computation of a confined fluid, the calculated pressure could be unstable and unsuitable for comparison with pressure in bulk conditions. Due to the constraint from boundary molecules, which changes the force field of fluid molecules, the calculated pressure in the confined system has a different meaning comparing to the one in bulk [100, 102]. Thus, to get the pressure of a fluid under confinement, an additional GCMC test in bulk conditions is conducted at the equilibrium chemical potential which is computed from gauge-GCMC tests.

3.5 Periodic boundary condition

Molecular simulation aims to provide information for the fluid system of a macroscopic based on the model system of a microscopic. Most simulations are performed in a system of particles in the size of a few hundred to thousands, which is still

an extremely small number compared with the thermodynamic system in a real situation. In order to simulate fluid properties in bulk, the periodic boundary condition is necessary to mimic the presence of an infinite bulk around the system box. In general, this setting means to repeat the cubic system box in three Orthogonal directions to fulfill the 3D space.

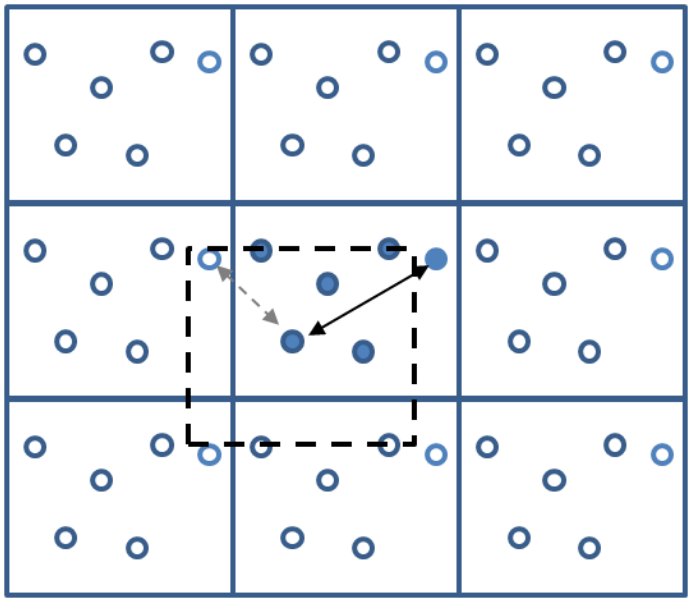

Figure 3.1: Schematic representation of periodic boundary condition.

As shown in Fig. 3.1, if any component of the distance vector is larger than half the box length in the same direction, this component should be substitute by the closest image. It will be easy to understand this substitute strategy based on following equations in the x-axis direction, where L_x is the box length.

$$\mathbf{r_{ij}}|_x = \begin{cases} \mathbf{r_{ij}}|_x + L_x & \mathbf{r_{ij}}|_x <= -0.5 * L_x \\ \mathbf{r_{ij}}|_x - L_x & \mathbf{r_{ij}}|_x >= 0.5 * L_x \end{cases} \tag{3.19}$$

4. CONFINED PHASE BEHAVIOR FROM GAUGE-GCMC*

To study the phase behavior under confinement or in porous media, we need to consider fluid compositions, system pressure, temperature, material for pore boundary and pore size distribution (PSD). In this chapter, the confined phase behavior is investigated based on the slit pore model and graphite as the boundary material. The contribution from PSD is not considered in the following cases. Based on the CBMC method, several Monte Carlo moves (e.g. regrowth, displacement, and transfer) are adopted to make fluid into equilibrium state in each box. Usually, the test cases reach equilibrium state after one million of Monte Carlo moves. Then the system is kept running for additional nine million Monte Carlo steps to get the average output. In the next sections, the pore model will be discussed in details, following by the vapor-liquid coexistence tests and confined fluid properties computation from simple to complex fluid cases.

4.1 Simulation setting

Graphite model is employed in this section to represent the material of pore boundary. This model is widely used in previous studies [4, 5, 38] because it has a simple structure and carbon is also one of the most common elements in shale rocks. Usually, the graphite model has a multilayer structure, in which the separation between layers is 0.335 nm. In each layer, the graphite has the hexagon lattice structure with bond length 0.142 nm. As shown in Fig. 4.1, the contribution from the second and above layers is negligible in the energy computation. Thus, only the single layer of graphite model is included at the top

*Part of the data reported in this chapter is reprinted with permission from "Phase behavior of multi-component hydrocarbon systems in nano-pores using gauge-GCMC molecular simulation" by Bikai Jin and Hadi Nasrabadi, 2016. *Fluid Phase Equilibria*, 425, 324-334, Copyright [2016] by Elsevier B.V.

and bottom of simulation box to form a slit model with a total boundary atom number of 2288. The pore diameter L_z is defined as the distance between the top and bottom layers. To make sure the calculated results match with the experimental data in bulk situations, the 3D periodic boundary condition [58] is used as the standard procedure in the molecular simulation. However, to avoid the molecular overlap or meaningless system structures, the simulation box cannot be periodically repeated in the vertical direction. Thus, the 2D periodic boundary condition is applied for this slit pore structure. The simulation box dimension settings ($L_x = 5.5497\ nm$, $L_y = 5.42234\ nm$) are shown in Fig. 4.1 for all case studies in this section. The box sizes are designed by duplicate the lattice cell in horizontal directions several times. According to the LJ parameters in Table 3.1, the r_{cutoff} is determined as 2 nm in all cases.

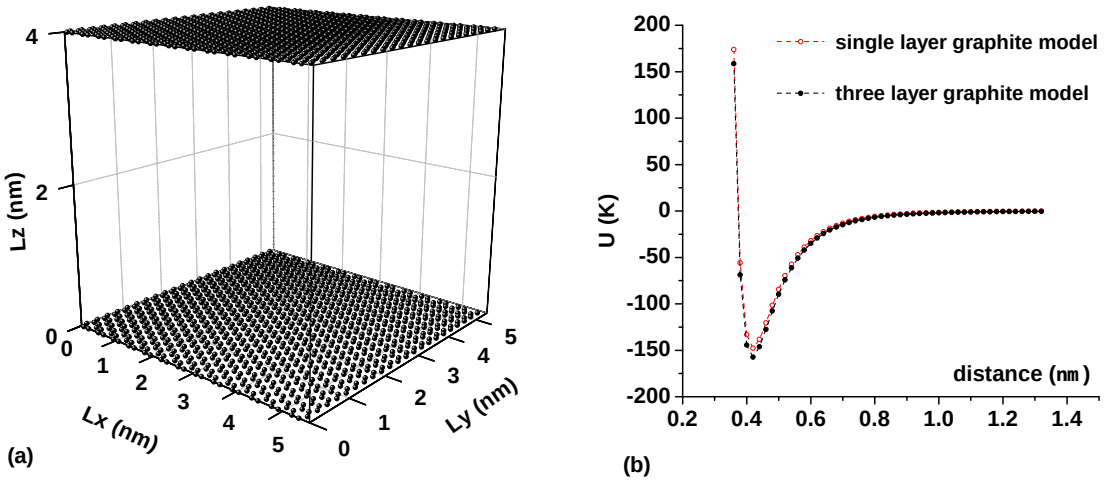

(a) Slit pore model. Sphere: boundary atoms. (b) LJ potentials for the CH_4 atom in three layer and single layer graphite models. Reprinted from [3].

Figure 4.1: Slit pore model and the potential comparison between two graphite models

4.2 Vapor-Liquid coexistence

Two group tests (five cases in each group) are conducted for ethane in bulk situation and under confinement, based on CMC technique. The box dimensions are set up as $L_x = 22.1988nm$,$L_y = 5.4223nm$, $L_z = 4nm$. The maximum displacement is set up as a constant 5 nm in all cases. The molecule number is kept as constant 2000 in the five cases of the bulk test group. As the $x - z$ side view in Fig. 4.2(A), all molecules are put in the center of the box as "saturated liquid" in the initial configuration. After simulation begins, the liquid begins to swelling, and evaporation happens. Molecules enter the empty regions at the ends of the system, which becomes the gas region after equilibrium. There is a clear phase separation when the temperature is below the critical point, and the phase separation vanishes when the temperature is higher than the critical value.

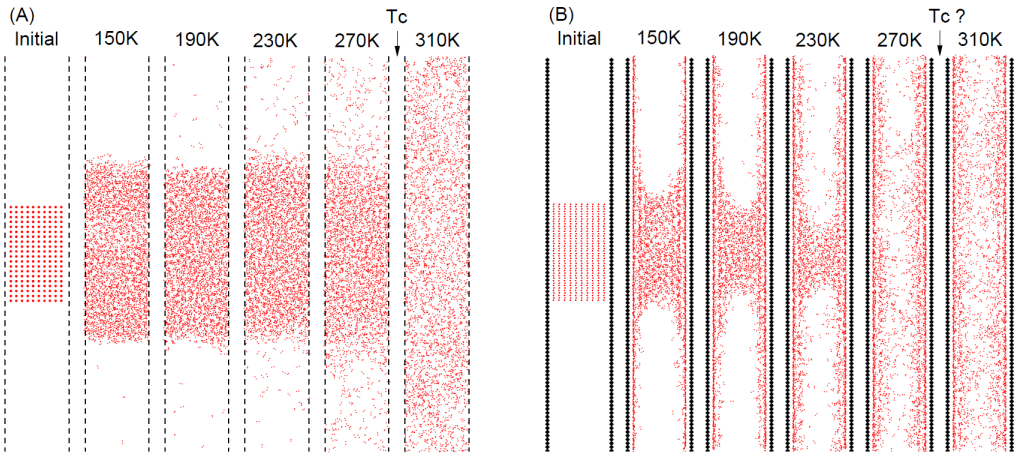

(A) the bulk situation, (B) in 4 nm slit pore. Solid line: box dimensions. Diamond and circle: graphite and ethane molecules, respectively.

Figure 4.2: CMC tests for ethane.

In the group tests under confinement (Fig. 4.2(B)), the molecule number is kept as constant 2000 in five cases. Since the existing of slit pore boundary, some ethane molecules will be adsorbed to the pore boundary, other free molecules can still move in the pore center and lead to the density fluctuation parallel to the pore axle direction. Here, the density means the average density. At lower temperature, there are only adsorbed molecules and a few free molecules in two ends of simulation box. Most free molecules are attracted to each other and located between adsorbed layers at the box center. Based on the density difference between fluids in the two ends and in the box center, they are treated as the gas-like and liquid-like states, which are named as gas phase and liquid phase in this work. Two phases are separated by an inter-phase region, not as an inter-phase surface in bulk. When the temperature is approaching critical point, the inter-phase region will be expanded and the density gap will vanish between two phases. There is only one phase when the temperature is higher than the critical value, and density fluctuation is only introduced in the radial direction.

Another two group tests are set up for one ternary fluid ($C_1/C_3/nC_5$) at 160 °F(Fig. 4.3, 4.4). All molecules are put in the box center as the initial configuration. After equilibrium, molecule distribution is different for each component in bulk and under confinement. Methane acts like gas with nearly homogeneous distribution in bulk and under confinement. Heavy components have high potential to keep the initial state and result in the density difference along the pore axis in the bulk situation. However, the high pore-fluid interaction leads to evenly distribution for heavy components along pore boundary under confinement. Also, the heavier components have two peaks of the molecular distribution in the radial direction under confinement (Fig. 4.5).

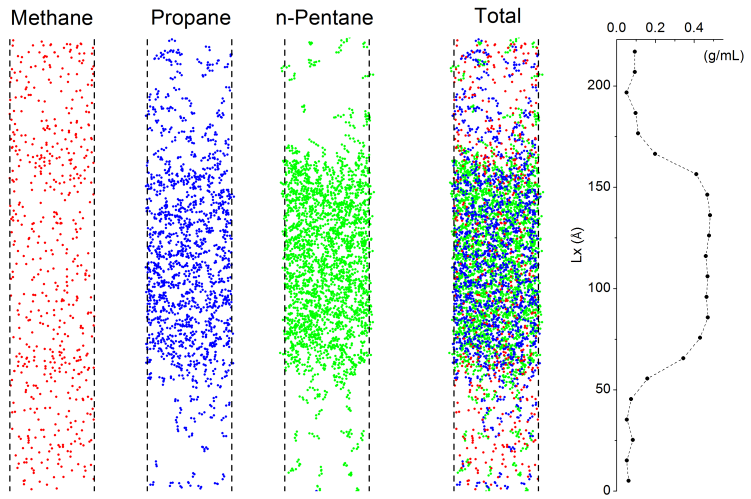

Black dash line: box dimensions, red: methane, blue: propane, green: n-pentane. $T = 160$ °F.

Figure 4.3: Final configurations of CMC tests for $C_1/C_3/nC_5$ fluid in bulk.

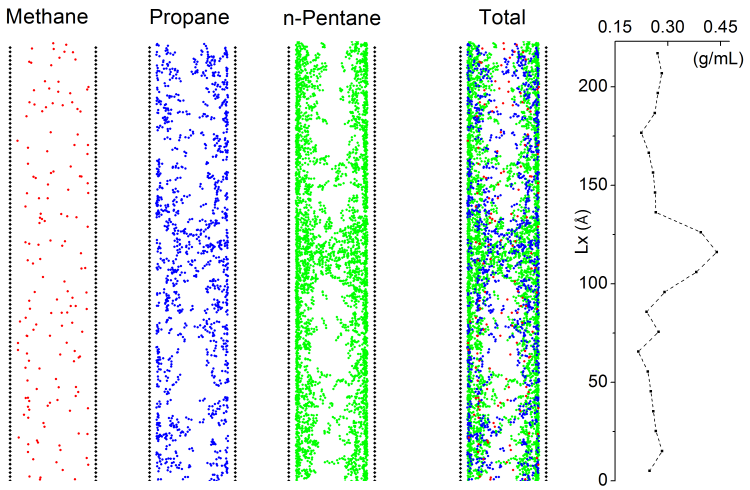

Black diamond: graphite, red: methane, blue: propane, green: n-pentane. $T = 160$ °F.

Figure 4.4: Final configurations of CMC tests for $C_1/C_3/nC_5$ fluid in 4 nm slit pore.

It could be concluded that two-phase coexisting is possible for fluid mixture under

confinement with heterogeneous molecular distribution based on the density difference (4.3), as reported in [103] that liquid and vapor phases can coexist in nanopores with the same chemical potential.

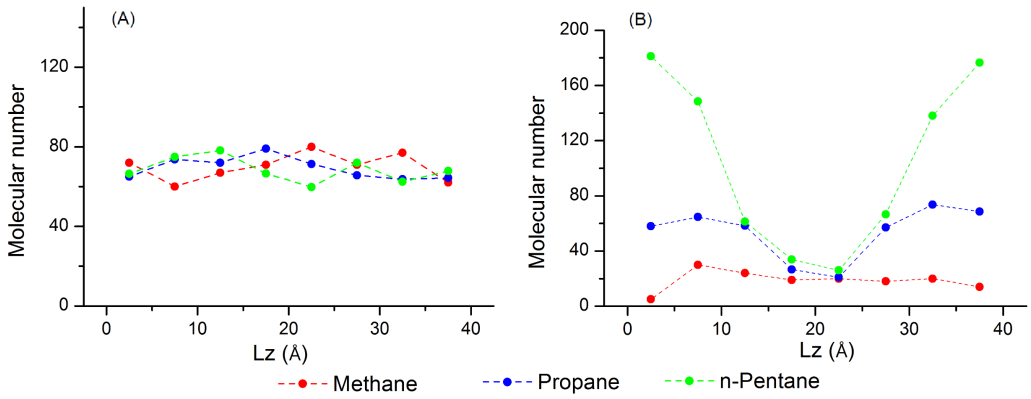

CMC tests for $C_1/C_3/nC_5$ fluid at 160 °F. (A) bulk condition, (B) 4 nm slit pore.

Figure 4.5: The profile of molecular number in the radial direction.

4.3 Single component fluids

For the accuracy benchmark tests, gauge-GCMC is employed in the phase behavior simulation of methane and ethane in bulk situations. The results are compared with those from GCMC simulations and theoretical results from the NIST [104]. The relative errors between the simulation results of the two methods and theoretical data are within 5% (Fig. 4.6). To compute the phase diagrams under confinement, the slit pore model is introduced in the simulations with various pore diameters (Fig. 4.7).

For fluids under confinement, the phase diagrams are generated from a set of gauge-GCMC tests at given box volume and system temperature. In each set, the molecular number varies in different cases. For example, the molecular number increases

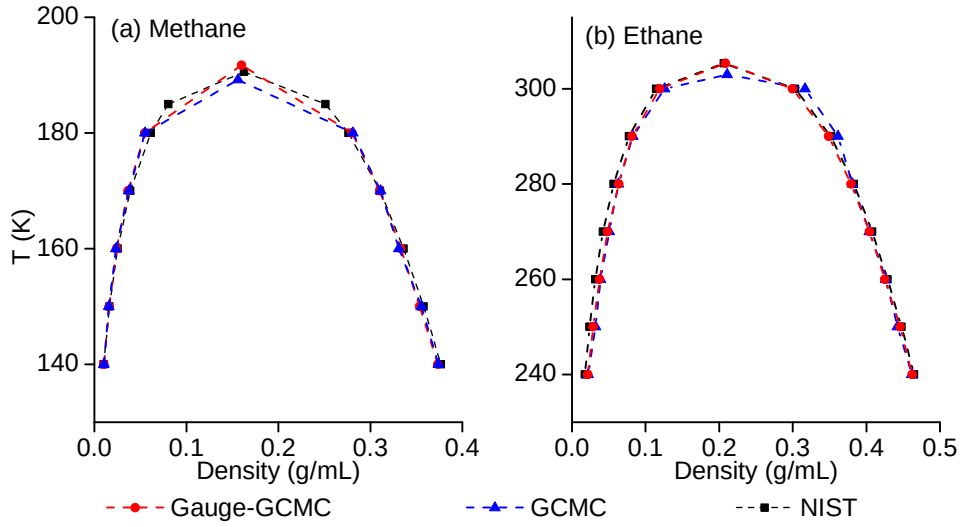

Squares: NIST data. Triangles: GCMC results. Circles: gauge-GCMC results. Reprinted from [3].

Figure 4.6: Phase diagrams of pure fluids in bulk condition.

from 100 to 4000 for tests of methane, and from 100 to 2500 for cases of ethane. Based on the results of each set, the phase equilibrium properties can be calculated following the Max equal area rule (Fig. 4.8). As the benchmark, GCMC method is conducted at the same temperature by setting different chemical potential inputs in a series of simulations. For instance, some trial tests are performed under confinement for ethane at 270 K with μ/k_B in the range (-3332 K, -3390 K) to generate the histogram records of system energy and molecular number in bimodal shape. The critical temperature is determined when the difference is minimized between the distributions of ordering operator in the 3D Ising universality class and ordering operator $P_L(x)$ (Fig. 4.9) [84]. The fluid properties of vapor and liquid at lower temperatures are generated based on the GCMC histogram reweighting method as discussed in chapter 2.

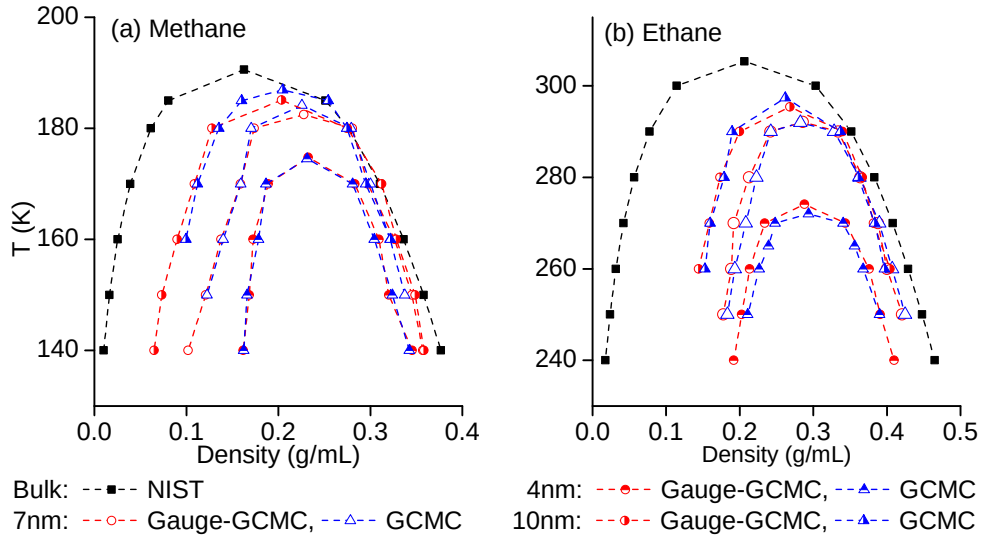

Squares: NIST data. Triangles: GCMC results. Circles: gauge-GCMC results. Reprinted from [3].

Figure 4.7: Phase diagrams of pure fluids in different slit pores.

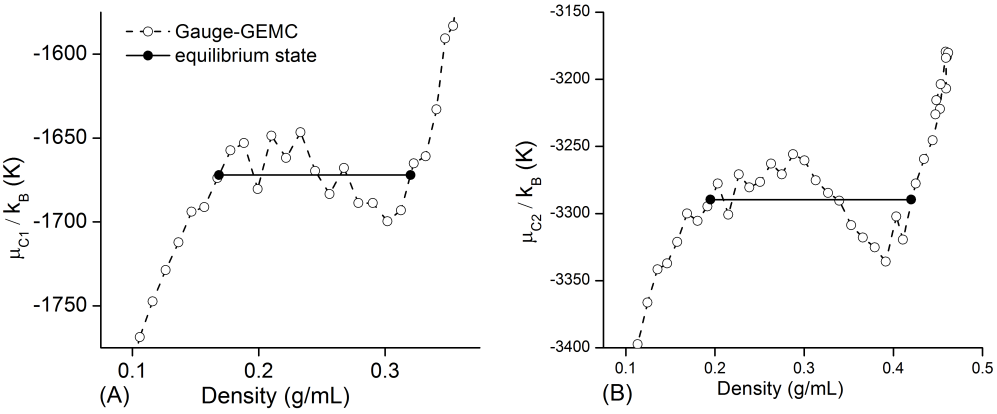

(a) methane at 150 K, (b) ethane at 240 K.

Figure 4.8: $\mu - \rho$ diagrams of 4 nm slit pore tests from gauge-GCMC method.

As shown in Fig. 4.8, there is an excellent match between the results of gauge-GCMC and GCMC methods in each nanopore cases. The vapor density is increased under confinement while a reduction is observed in the liquid density in tests of several pore diameters. Comparing with the bulk data, the confined critical point has a larger density and smaller temperature. By changing the pore diameter from small to large, the difference is decreased between the confined phase diagrams and bulk data, as stated in other work [4].

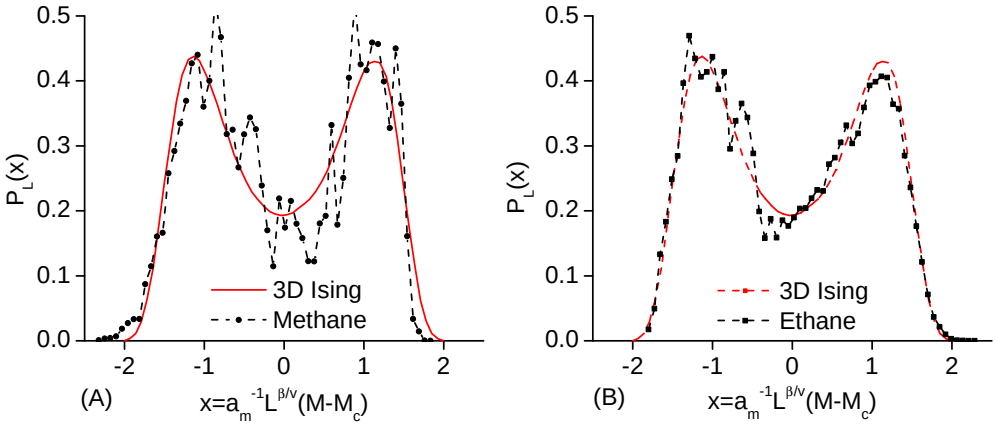

Squares: test results in 4 nm slit pore. Solid lines: 3D Ising universality class.

Figure 4.9: Ordering operator distribution.

In one single test of gauge-GCMC method, different results will be yielded if the gauge meter is in confined or bulk conditions. However, only the $\mu - \rho$ relationship is the key to get the phase equilibrium properties, not a single data point. Thus, no matter what situation the gauge box is in, we can get the identical $\mu - \rho$ relationship of fluids in the system box, as shown in Fig. 4.10.

To get the snapshot of the final configuration of ethane in 4 nm slit pore, two additional GCMC tests are conducted based on the chemical potential computed from gauge-GCMC method, and multiple adsorption layers are observed in the density profiles (Fig. 4.11). Comparing the density profiles with the bulk data, two peaks are generated near the pore boundaries and the density matches the bulk data at the center region of the simulation box, which means the constraint effects are much stronger near the boundary than in the center. The molecular distribution in each phase is not homogeneous (Fig. 4.11). Since the fluid is at an internal equilibrium state and the molecules can move between the box center and the adsorption layers, it is not easy to have a clear separation between the adsorbed molecules and free particles in the center region. Thus, the average density is reported as the fluid parameters to determine the phase transition.

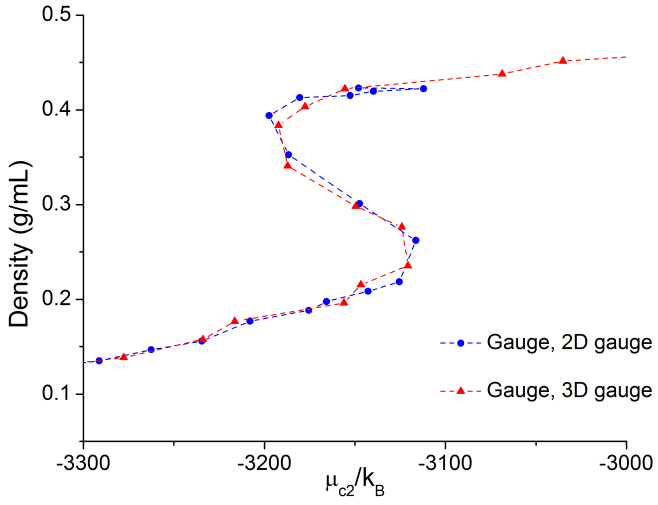

Blue circle: the gauge box in confinement situation with 2D periodic boundary condition. Red triangle: the gauge box in bulk situation.

Figure 4.10: $\mu - \rho$ relationship for ethane in 4 nm slit pore.

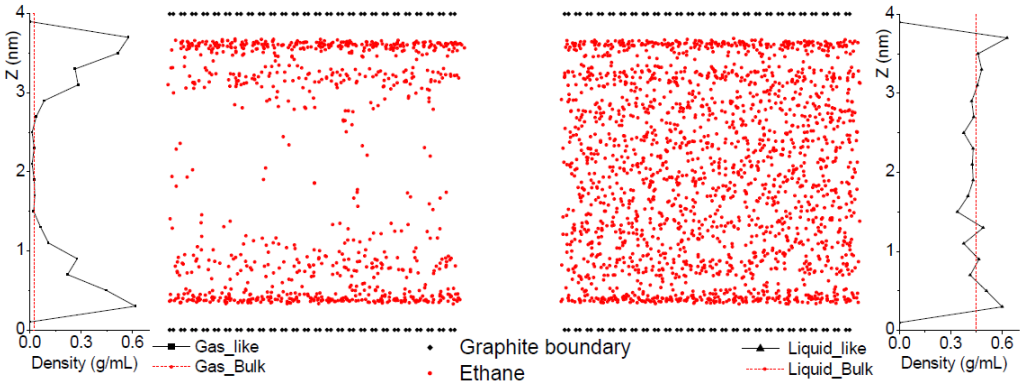

Spheres: ethane molecules. Squares: graphite model. Dashed lines: NIST data. Solid lines: density distributions from GCMC. Reprinted from [3].

Figure 4.11: Snapshots of confined ethane in two-phase equilibrium at 250 K.

Theoretically, the gauge-GCMC method can be treated as another modification of the GCMC, in which one hypothetical box is paired with the fluid system for the molecule transfer move. Because no volume shift move is considered in both methods, they have the similar computation efficiency. In addition, the molecular number is the output of the GCMC method but an input of the gauge-GCMC and the chemical potential is the input of the GCMC method but an output of the gauge-GCMC method. Since the molecular number is much easier to estimate as an input parameter than chemical potential, gauge-GCMC is the preferred method in the following studies.

4.4 Two component fluids

For the accuracy tests, three approaches (GCMC, gauge-GCMC and modified gauge-GEMC) are carried out in the simulations of the binary fluid (C_1/C_2) in bulk at 273.15 K. Based on the good agreement between the data from three methods and the theoretical results of Peng–Robinson equation of state (PR EOS) [105] from CMG, these methods are stable and suitable for simulation of binary fluids (Fig. 4.12).

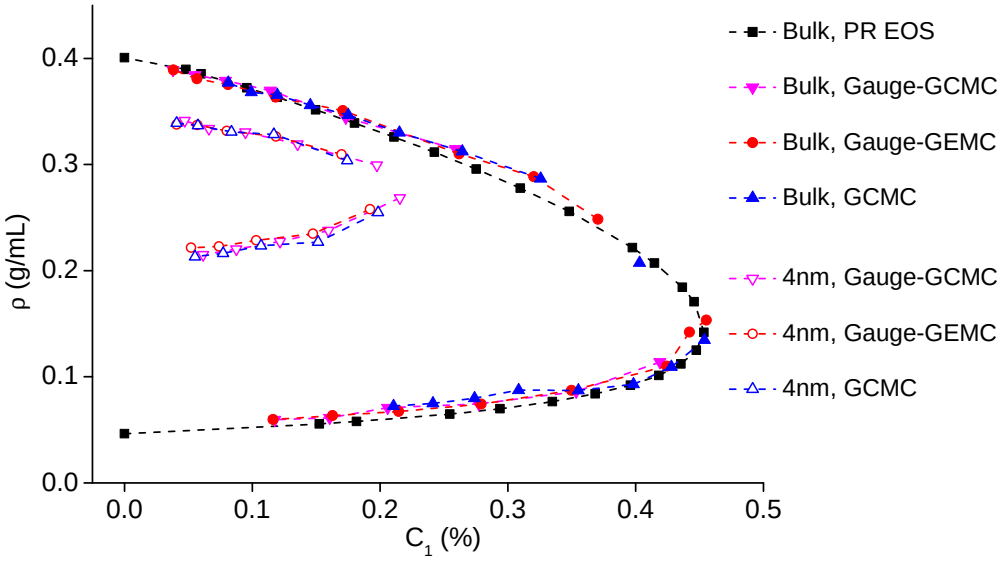

Downward triangles: gauge-GCMC results. Upward triangles: GCMC results. Circles: gauge-GEMC results. Squares: PR EOS results. Solid symbols: bulk situations. Empty symbols: in 4 nm slit pore. Reprinted from [3].

Figure 4.12: Density–composition diagrams of C_1/C_2 fluid at 273.15 K.

For tests in bulk, two identical boxes, either one could be the system box, are used in the gauge-GEMC simulations. By setting the molecular number N_{C_1} at specific values, a set of tests are computed by increasing the N_{C_2}, as shown in Fig. 4.13. After changing the value of N_{C_1}, more tests are conducted to generate a dense sampling in the $\mu_{C_1}\mu_{C_2}\rho$ space. Then the $\mu_{C_2}\rho$ diagram is interpolated from sampling points and used to calculate the phase equilibrium properties (Fig. 4.14). In GCMC simulations, several series tests are conducted by increasing μ_{C_2} while keeping μ_{C_1} at some specific values to generate the adsorption and desorption isotherms. For the gauge-GCMC method, which is used in a way similar to gauge-GEMC, several series tests are scheduled by increasing

N_{C_2} while keeping μ_{C_1} as constants to provide a dense sampling in the configuration space.

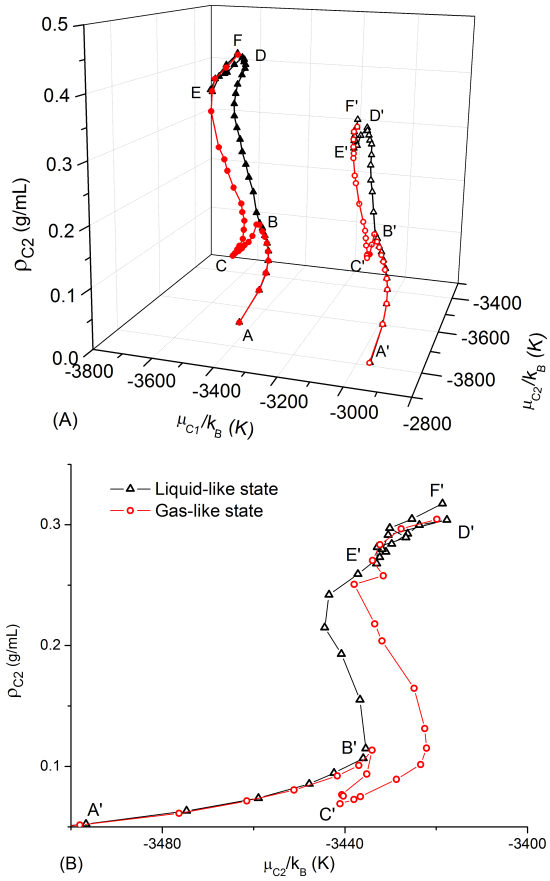

(A) 3D view, (B) $\mu_2 - \rho$ view. ABDEF and A'B'D'E'F': the liquid phase. ABCEF and A'B'C'E'F': vapor phase. $T = 273.15\ K$.

Figure 4.13: Sampling examples of C_1/C_2 system from gauge-GEMC in bulk.

After the above accuracy tests, the 4 nm slit pore boundary model is introduced in these three methods for the simulation of binary C_1/C_2 fluid. In the GCMC tests, μ_{C_1}/k_B varies from -3600 K to -3200 K while μ_{C_2}/k_B is set in the range of -4000 K to -2000 K. In the gauge-GCMC tests, N_{C_2} varies from 550 to 2450 while μ_{C_1}/k_B is set in the range

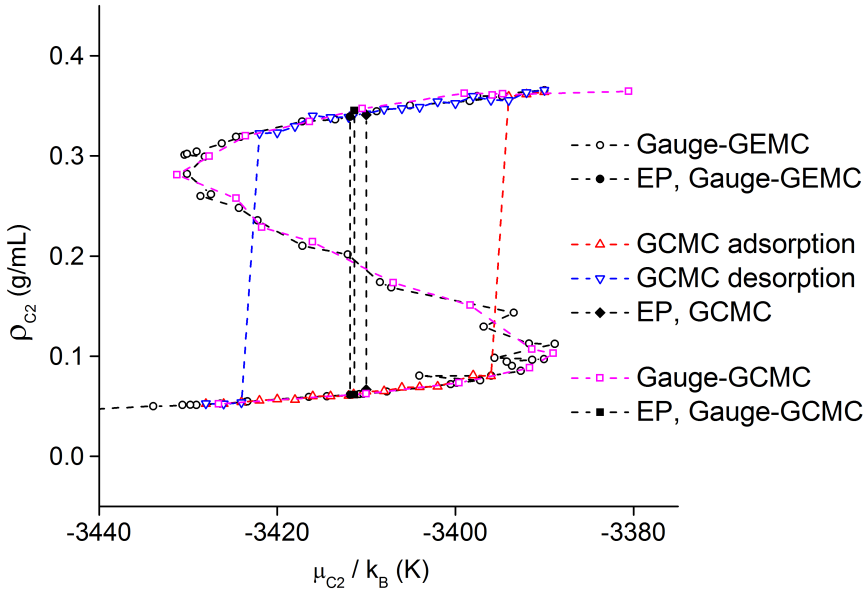

Adapted from [3].

Figure 4.14: Interpolated $\mu_{C_2}\rho$ diagram for C_1/C_2 fluid at 273.15 K in bulk.

of -3600 to -3200. In the gauge-GEMC tests, the N_{C_1} and N_{C_2} change from 50 to 550, and from 100 to 3000, respectively. Following the similar procedures described before, the parameter space μ_{C_1}-μ_{C_2}-ρ is intensively sampled and the equilibrium densities are also calculated. From Fig. 4.12, the liquid density is reduced while the vapor density is increased under confinement. A reasonable inference can be concluded that in the slit pore the critical point is shifted downward to a lower C_1 composition and higher density. From the additional GCMC tests at the equilibrium chemical potential (Figs. 4.15), there is a large divergence in the molecular number N_{C_2} between liquid and vapor states. Based on the number profile of each component in the radial direction (Fig. 4.16), the distributions of methane are quite similar in both phases. The N_{C_2} profiles are close to each other in the adsorption layers from two phases, but a big shift is presented at the box centers. Because the observation, that the N_{C_1} distributions are similar in both phases, is

available in other cases of this C_1/C_2 system, two reasonable inferences could be made: (1) C_2 has a stronger adsorption effect than C_1, and (2) the heavy component contributes more to the density difference between the two phases under confinement.

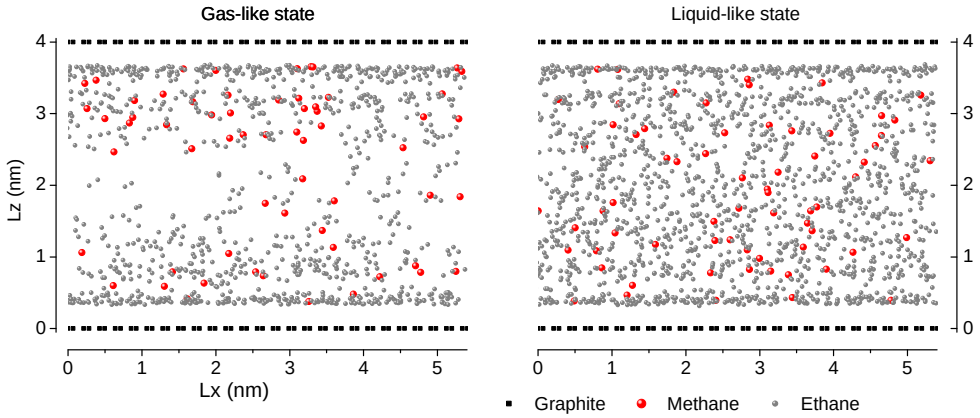

$\mu_1/k_B = -3400\ K, T = 273.15\ K$. Squares: graphite molecules. Gray, red spheres: C_2, C_1 molecules. C_1 is enlarged intentionally for better visualization. Reprinted from [3].

Figure 4.15: Side–view snapshot of the C_1/C_2 system under confinement

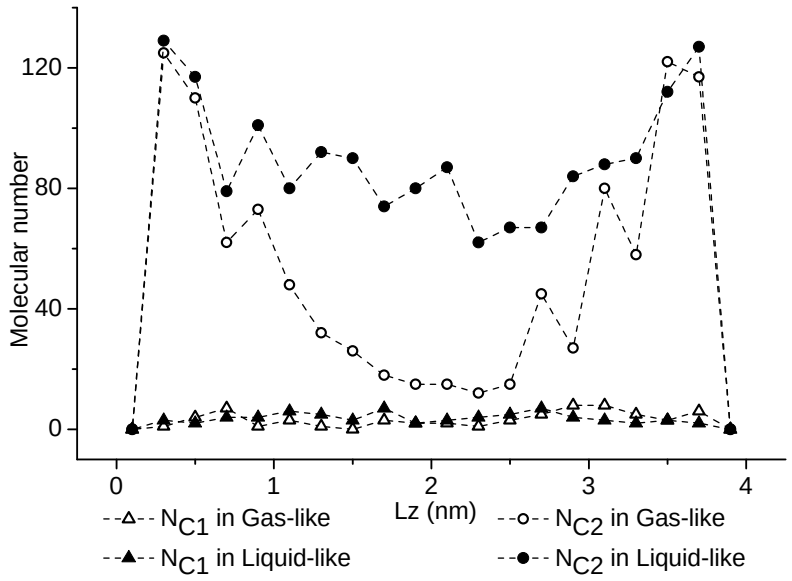

Empty, solid symbols: gas-like, liquid-like states. Triangles: N_{C_1}. Circles: N_{C_2}. Reprinted from [3].

Figure 4.16: Radial profiles of molecular number in the above Figure.

4.5 Multiple component fluids

For multi-component fluids, gauge-GEMC and GCMC are not suggested for the simulation because the prohibitive computation cost. One ternary fluid ($C_1/C_3/nC_5$) is studied in this section at 344.26 K (160 °F), and only gauge-GCMC is used for the simulation of phase equilibrium properties. As a standard procedure, a series accuracy simulations are carried out and compared with the data of PR EOS. As shown in Fig. 4.17, a great match is observed between the EOS data and the gauge-GCMC results in bulk conditions.

Following the similar procedure as in the binary test before, two identical boxes are included in the gauge-GCMC simulation. By setting up constant values for μ_{C_1} and μ_{C_3},

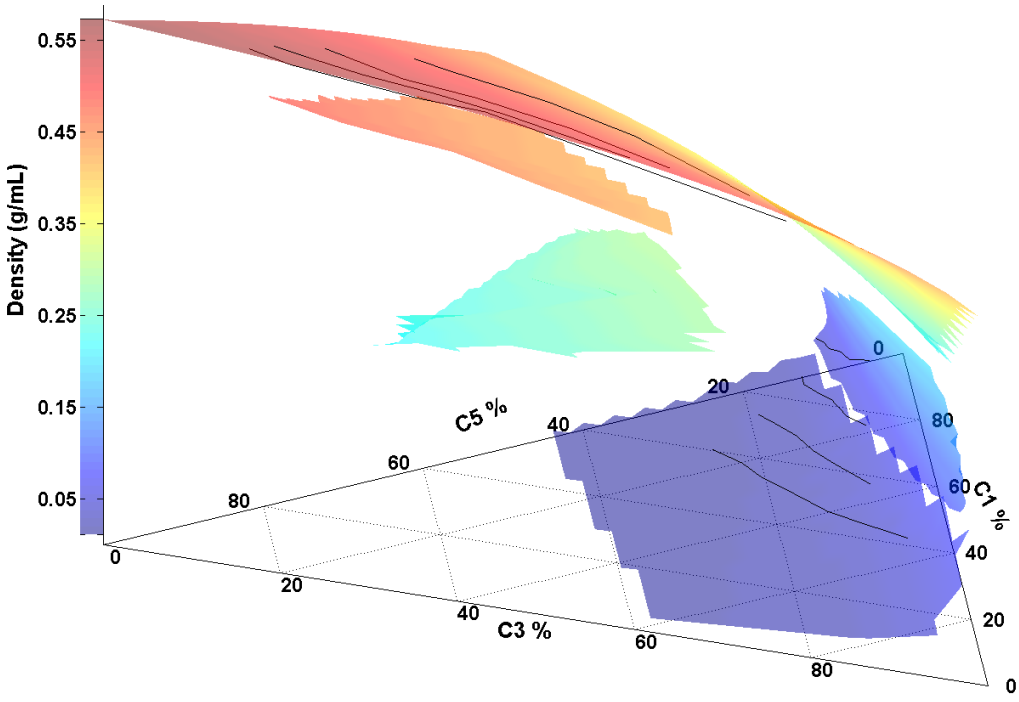

Black lines: accuracy tests in bulk. Inside contours: test results under confinement. Outside contours: theoretical results from the PR EOS in bulk. Reprinted from [3].

Figure 4.17: Composition–density diagrams of the $C_1/C_3/nC_5$ system at 344.261 K.

a set of simulations are performed by increasing the N_{nC_5}. From these simulation cases, the μ_{nC_5}-ρ relationship is provided for equilibrium density computation (Fig. 4.18). By running other series tests at various combinations of μ_{C_1} and μ_{C_3}, a sampling is generated with sufficient data points in the parameter space μ_{C_1}-μ_{C_3}-μ_{nC_5}-ρ. In Fig. 4.17, two surfaces are interpolated from theoretical data of the PR EOS to represent the liquid and vapor phases, which are named as the liquid surface (top) and vapor surface (bottom). The results of accuracy tests are plotted as black lines in this density–composition diagrams. Note that the results of accuracy tests show an excellent match with the theoretical data and the difference between the lines and surface is negligible.

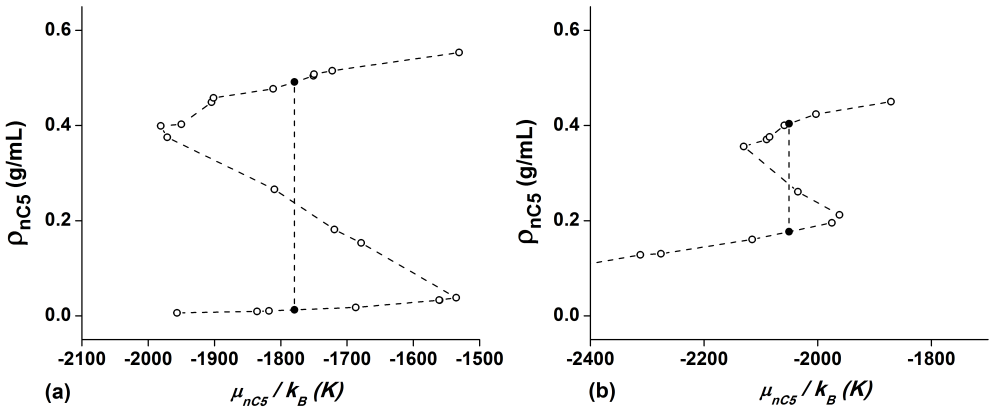

(a) in bulk, (b) in 4 nm slit pore. $\mu_{C_3}/k_B = -4500\ K$, $\mu_{C_1}/k_B = -4450\ K$. Reprinted from [3].

Figure 4.18: $\mu_{C_5}\rho$ diagrams in the $C_1/C_3/nC_5$ system at 344.261 K.

After the accuracy tests in bulk, the pore boundary is introduced as a 4 nm slit pore in the phase equilibrium simulations at 344.26 K. In the gauge-GCMC simulations, μ_{C_1}/k_B is in the range of -4450 to -3850, μ_{C_3}/k_B varies in the range of -4700 to -4000, and N_{nC_5} is increased from 50 to 1050. The μ_{nC_5}-ρ diagram has a clear van der Waals shape as shown in Fig. 4.18 from the series tests at a specific combination of μ_{C_1} and μ_{C_3}. Performing the above series simulations at other combinations of μ_{C_1} and μ_{C_3}, the equilibrium properties of confined phases are calculated and interpolated as inner curved surfaces in Fig. 4.17. Based on this 3D relationship, the density difference between the liquid and vapor phases is reduced, while the liquid density is decreased and the vapor density is increased. Several 2D slices are generated in Figs. 4.19 and 4.20 from the 3D figure. It is clear that the liquid phase has a limited change in the composition under confinement, however, the vapor phase shows a dramatic change in the composition with an increase of $nC_5\%$, because a lot of nC_5 molecules are adsorbed into the vapor phase. Based on the composition and density diagrams, it could be concluded that the critical point will be shifted to a large density. Also, the critical points under confinement have

larger compositions of nC_5 and C_1, but a smaller C_3 composition compared with those values in bulk.

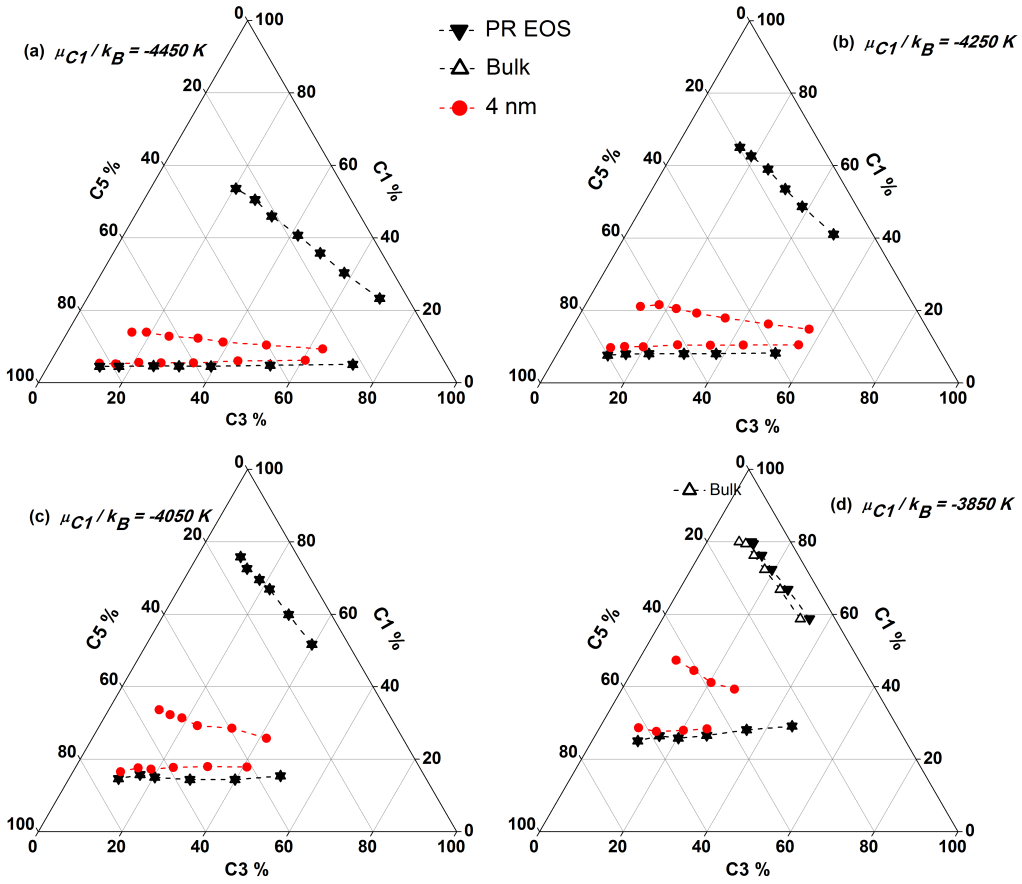

Empty triangles: gauge-GCMC results in bulk. Solid triangles: PR EOS data. Solid circles: gauge-GCMC results in a 4 nm slit pore. (a) $\mu_{C_1}/k_B = -4450\ K$, (b) $\mu_{C_1}/k_B = -4250\ K$, (c) $\mu_{C_1}/k_B = -4050\ K$, (d) $\mu_{C_1}/k_B = -3850\ K$. Reprinted from [3].

Figure 4.19: Ternary diagrams for the $C_1/C_3/nC_5$ system when $T = -344.261\ K$.

From the molecular distributions at equilibrium states (Figs. 4.21, 4.22), there is a large difference in the nC_5 molecular number between the liquid and vapor phases.

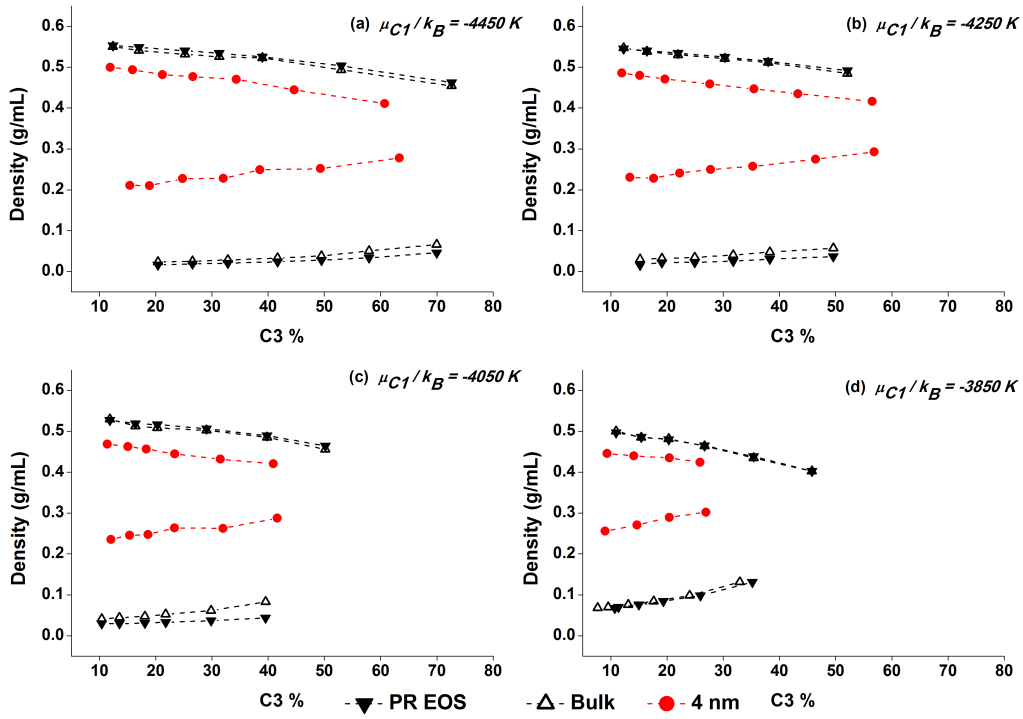

Empty triangles: gauge-GCMC results in bulk. Solid triangles: PR EOS data. Solid circles: gauge-GCMC results in a 4 nm slit pore. (a) $\mu_{C_1}/k_B = -4450\ K$, (b) $\mu_{C_1}/k_B = -4250\ K$, (c) $\mu_{C_1}/k_B = -4050\ K$, (d) $\mu_{C_1}/k_B = -3850\ K$. Reprinted from [3].

Figure 4.20: Density–Composition diagrams for the $C_1/C_3/nC_5$ system when $T = -344.261\ K$.

Based on two GCMC tests at the equilibrium chemical potential, the profiles of molecular number are generated in the radial direction (Fig. 4.22). The N_{C_1} distributions are quite similar in both phases. The N_{C_3} profiles have the close shape in the adsorption layers of both phases, and the same observation for N_{nC_5}. However, large differences are shown in the profiles of N_{C_3} and N_{nC_5}. Based on the tests of binary and ternary fluids, the two inferences in above section are more reliable that heavier components have stronger adsorption effect than lighter components, and heavier components contribute more to the density separation between two phases.

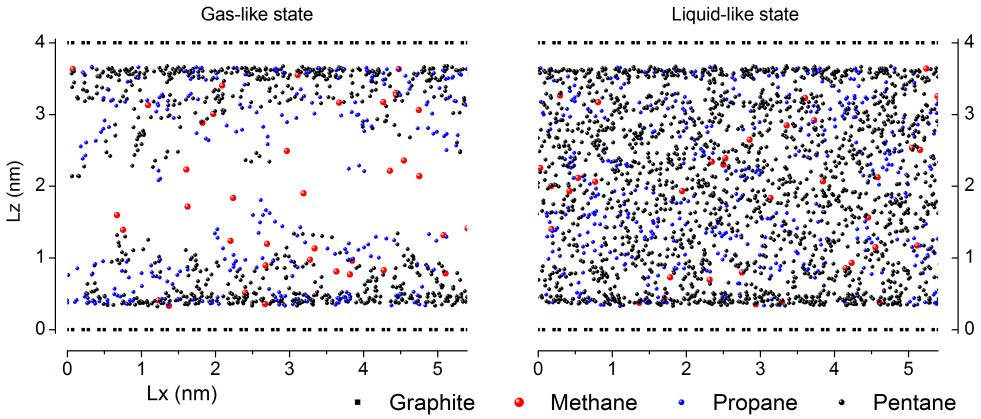

$T = 344.26\ K$, $\mu_1/k_B = -4400\ K$, $\mu_3/k_B = -4000\ K$. Black square: graphite molecule. Red: methane. Blue: propane. Black dot: n-pentane. Enlarged symbols for better visualization. Reprinted from [3].

Figure 4.21: Snapshot of $C_1/C_3/nC_5$ system under confinement.

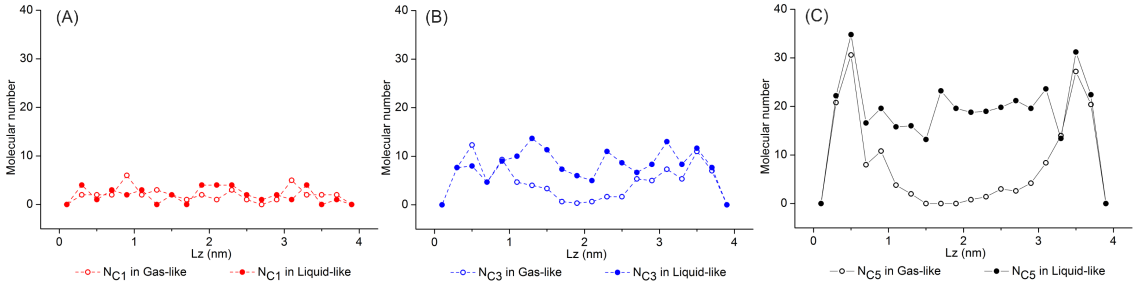

Radial distribution. (A) Methane, (B) Propane, (C) n-Pentane. Reprinted from [3].

Figure 4.22: Molecular number distributions in two phases from above figure.

5. PHASE BEHAVIOR IN SHALE CONSIDERING THE PORE SIZE DISTRIBUTION EFFECT*

As mentioned in chapter 1, shale pore system contains pores with various diameters, which is described as pore size distribution (PSD). To further understand the PSD influence on the confined phase behavior in nanopores, several cases are conducted by gauge-GCMC method to simulate phase diagrams of pure methane based on single-pore models with the diameter in the range of 4 to 10 nm. Then, several multiple pore models are designed to quantify the PSD effect on the phase behavior, including a model based on one shale rock sample from Eagle Ford field.

5.1 Simulation setting

The cylindrical model is designed as shown in the schematic of Fig. 5.1. Initially, one cubic box is saturated with a multilayer graphite model in which a layer separation is set as 0.335 nm in the Z direction. In each graphite layer (X-Y plane), carbon atoms are arranged following hexagon cell structure with a bond length of 0.1423 nm. After cutting out redundant atoms, the cylindrical model is finalized with a single pore diameter and boundary thickness. This single pore model is introduced in the fluid system box with 1D periodic boundary condition in the Z direction while the gauge box is performed in bulk with 3D periodic boundary setting.

From the field data of pore size distribution (PSD) in shale rocks, a pore system usually

*Part of the data reported in this chapter is reprinted with permission from "Molecular simulation of the pore size distribution effect on phase behavior of methane confined in nanopores" by Bikai Jin, Ran Bi, and Hadi Nasrabadi, 2017. *Fluid Phase Equilibria*, 452, 94-102, Copyright [2017] by Elsevier B.V.

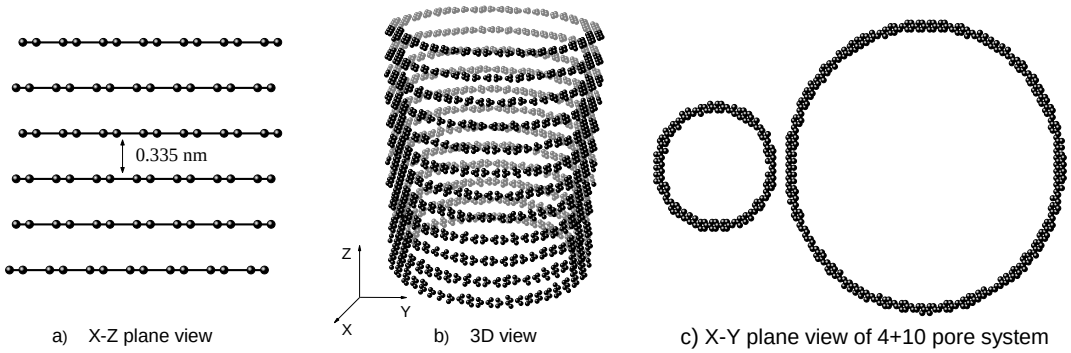

a) X-Z plane view of a multilayer graphite model. The layer separation is 0.335 nm and the bond length is 0.1423 nm. b) 3D view of a cylindrical pore with different colors for better visualization. c) X-Y plane view of a 4+10 parallel model. The atom size does not scale to the real values. Adapted from [16].

Figure 5.1: Schematic representation of the cylindrical model.

consists of pores varying from micropore ($< 2nm$) to macropores ($> 100nm$). Usually, the pore length is several orders of magnitude larger than the pore diameter [9, 106]. Based on the 1D periodic boundary condition, a single cylindrical model can represent the segment of pores with the similar diameters. By ignoring the boundary effect at conjunction points between pore segments, a pore system can be modeled by several single cylindrical pores with varying sizes. To investigate the PSD effect on the phase behavior, a multiple pore structure is designed as parallel pores, which is easy to implement in the simulations.

In this parallel model (Fig. 5.1c), pores with different diameters are aligned in the same direction. The pore model length needs to be at least $2 * r_{cutoff}$ to avoid overlap in the energy calculation. By keeping the gauge box in a bulk situation, this model is only considered in the fluid system box. Inside this model, fluid particles can be exchanged with each other between different pores. Since the pore boundary thickness could be

a large value and the pore separation could vary in the shale condition, there should not be any limit on the spatial positional relationship between pores. Thus, the energy computation between the pore i and pore j is not allowed while the boundary molecules of pore i are only used in the fluid energy calculation in pore i. During the simulation, the system energy is defined as the summation of the energies separately computed in each pore. Also, the total volume of each single pore is set as the system volume. In this work, a multiple pore model is named using the combination of pore diameters, such as the dual pore model in Fig. 5.1c is called "4+10" model.

5.2 Single pore size

In previous chapters, the gauge-GCMC has been proved as accurate as other Monte Carlo methods for phase behavior simulation of pure and multiple component fluids in bulk and confined situations [3]. In this section, the simulations of methane phase behavior are conducted based on a single-pore model with various diameters in the range of 4 to 10 nm (Fig. 5.2). As stated before, the phase diagram is computed based on several series of tests while each series is performed at one specific temperature with the different molecular number as inputs. By repeating the above process in pore models with different diameter, the phase diagrams of methane are generated as shown in Fig. 5.2 to show the PSD effect. Note that the density difference is decreased between two phases in these nanopores by increasing the vapor density and reducing the liquid density. The critical point is shifted downward with a higher density and lower temperature. It can be inferred that the phase diagram will approach the curve in bulk if the pore diameter is sufficiently large. Also, the shift trends of phase diagrams are similar to other observations [3, 4, 38]. Since different pore models are used in these works, there is no numerical comparison between our results and previous data.

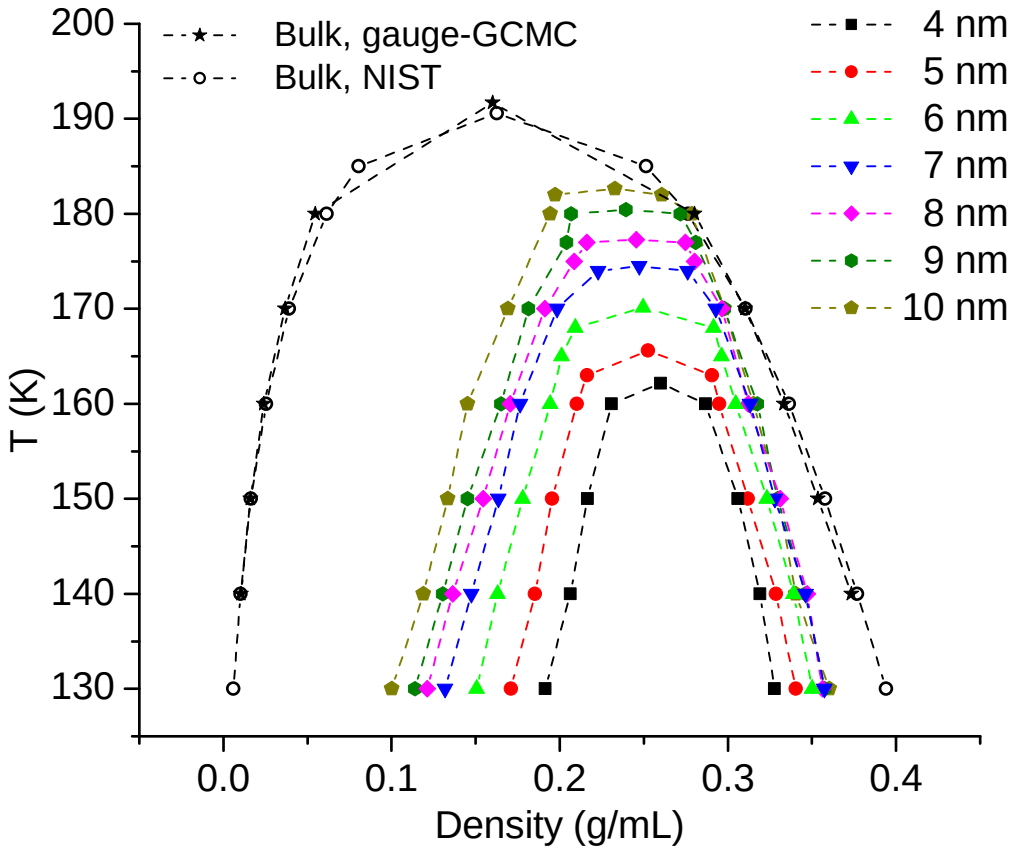

Empty circle: bulk data from NIST [104]. Square, circle, upward triangle, downward triangle, diamond, hexagon, pentagon: corresponding to the results of pores with diameters ranging from 4 to 10 nm, respectively. Star: simulation verification of gauge-GCMC method in bulk [3]. Reprinted from [16].

Figure 5.2: Temperature-density diagram of methane in cylindrical models with different diameters.

The system equilibrium state is determined when the fluid density gets stable in the system box, while the system Helmholtz free energy is minimized. Another GCMC tests are conducted based on the chemical potentials at equilibrium states to generate the density distribution of confined liquid and vapor phases in the radius direction. After the

systems get equilibrium, the simulation is continued for another 2 million Monte Carlo steps to generate 201 snapshots for the computation of radial distance of each molecule. These distance data are defined as zero at the pore boundary and are used to provide the density profile based on histogram analysis with an interval size of 0.05 nm (Fig. 5.3). The density profiles of the liquid phase from different pore size models have a similar distribution, including clearly multiple adsorption layers near the pore boundary, and the density approaches the bulk data as the distance from the boundary increases.

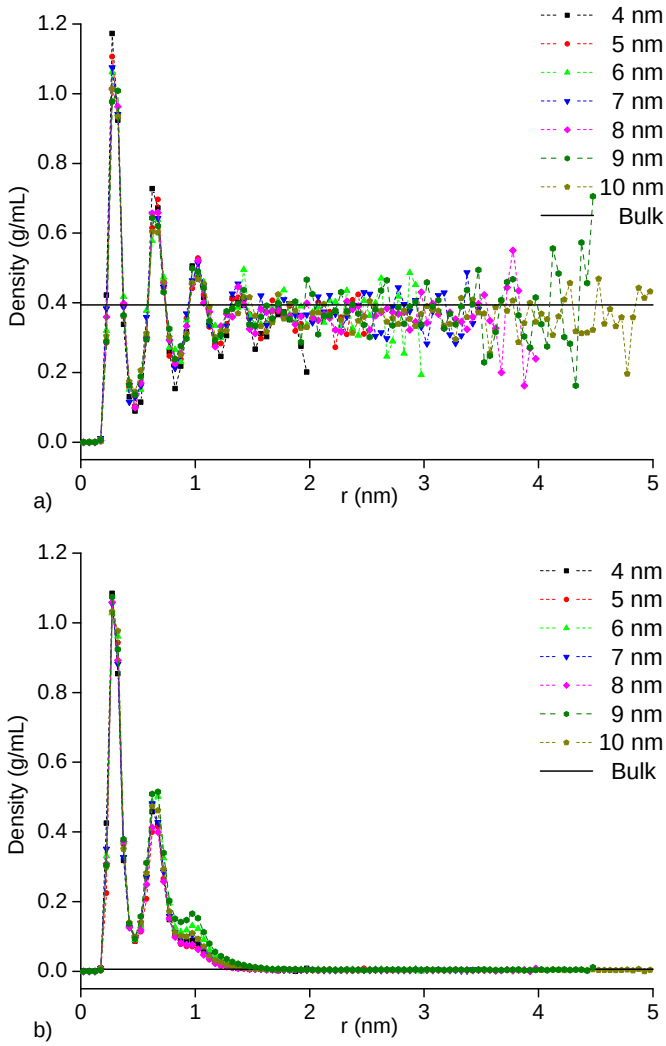

a) Liquid state, b) vapor state. Solid line: bulk data from NIST. Legends follow the above figure. Reprinted from [16].

Figure 5.3: Density radius profiles of methane at 130 K in single pores.

In addition, a fluctuation is observed in the density profiles near the box center, which can be explained as the free movement of molecules resulting from the weak adsorption effect. In the vapor cases, there are two adsorption layers, in which the highest density peak has the similar values as that of the liquid state. Comparing results from pores of

various diameters, pore of a large diameter only expands the center region and causes a limited change in the distribution of adsorption layers. It is a reasonable conclusion that the density profile in large pores ($> 10\ nm$) will have the similar shape of distribution curve as those in Fig. 5.3.

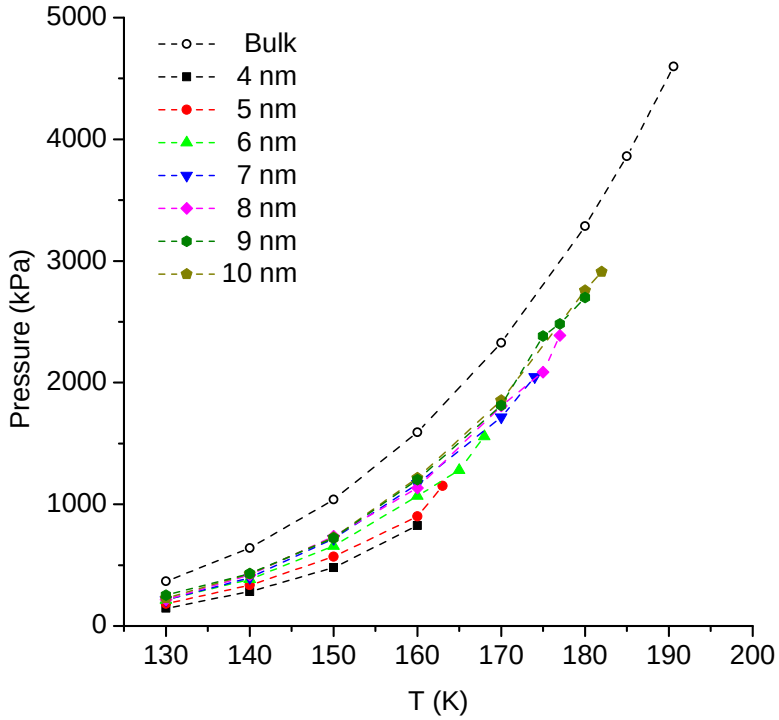

Figure 5.4: Pressure-temperature diagrams of confined methane.

At the equilibrium state, the confined fluids are also in equilibrium with the bulk vapor with the same chemical potential. Since the pressure inside the pore has different implications due to varied stress tensor [3, 102], the corresponding bulk pressure will be calculated from additional GCMC in bulk based on the equilibrium chemical potentials. As shown in Fig. 5.4, the pressure-temperature diagrams under confinement share the

same pattern with the bulk curve. The equilibrium pressure is increased with higher temperature. When the system temperature is close to the critical point, the phase separation is not so clear that the fluctuation may happen in these diagrams. When the pore is expanding, the pressure values will rise to the bulk data. Here, the critical pressure is not included since the chemical points are extrapolated without definite chemical potentials.

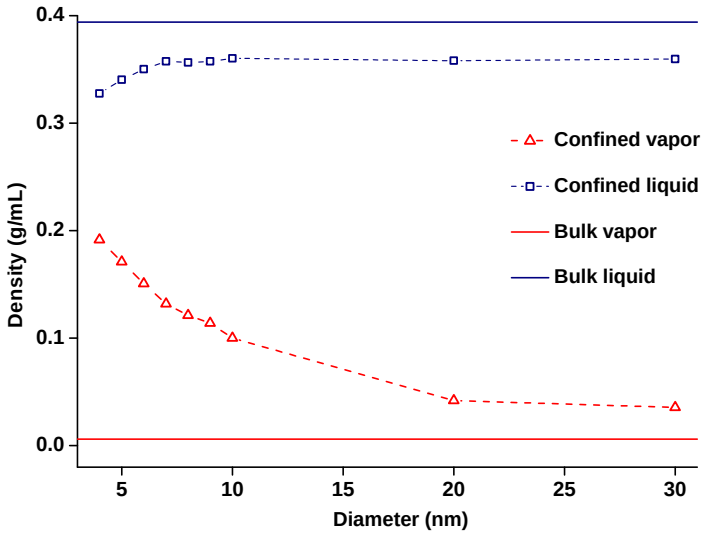

Solid lines: bulk data. Square, triangle: densities for liquid and vapor phases under confinement.

Figure 5.5: Density-diameter diagram for methane at 130 K.

To investigate the adsorption effect in big pores, two extra tests are conducted with large diameters (20 and 30 nm). Since the computation time is extremely long, the simulations are only performed for methane at 130 K (Fig. 5.5). As expected, the liquid density is increasing and vapor density is decreasing with growing pore diameter. Due to

the adsorption effect (Fig. 5.3b), the confined vapor density will always be higher than the bulk data. However, repulsion is associated with adsorption, which results in an empty region near the pore boundary in liquid states (Fig. 5.3a). This empty layer may have a negative contribution to the average density calculation, which is shown as a flat curve in confined liquid density (Fig. 5.5). From tests in this section and previous [3], it is hard to say that the contribution from adsorption is negligible in pores larger than 10 nm, especially in the vapor phase. On the contrary, the gas production will still suffer from the adsorption effect in big pores.

5.3 Multiple pore size

To investigate the PSD effect on confined phase behavior, multiple pore system is represented by parallel pores with several diameter combinations. Beginning with two dual-pore models and ending with an Eagle Ford case, the pore model gets complicated and closer to the real pore system in shale rock.

4+4 model

A validation case is conducted here to check if the same-size pores can produce similar phase diagrams as those of one single size model. Thus, two identical cylinders with 4 nm diameter are parallel placed in the fluid system box with 1D periodic boundary condition. The temperature-density relationship has a good match with the results from 4 nm single pore model, as shown in Fig. 5.6. Based on the density distribution of final configurations of 4+4 model tests at 130 K (Fig. 5.7), in which the interval size is set as 0.05 nm in the radius direction, these two cylinders are in the same situation during the simulation, which means the two pores are filled up at the same pace. Two adsorption layers are observed in both pores with the trend approaching bulk data at the box center.

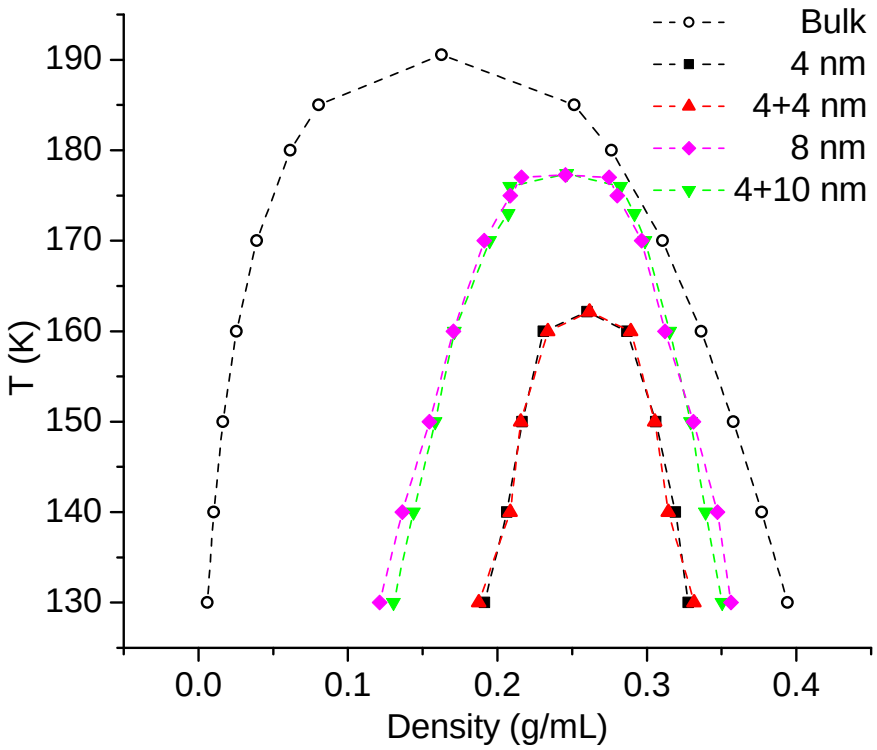

Empty circle: theoretical data in bulk. Square, diamond, upward triangle, downward triangle: corresponding to a single pore with a 4 and 8 nm diameter, and multi-pore models with diameters of "4+4" and "4+10" nm, respectively. Reprinted from [16].

Figure 5.6: Temperature-density diagram of methane in multi-pore models.

4+10 model

This 4+10 dual-pore model consists of two parallel cylinders with diameters in 4 and 10 nm. The system volume is defined as the summation of internal pore volumes. Methane molecules can be moved between these two cylinders and transferred between the gauge box and the system box. The simulation results are shown in Fig. 5.6, in which the phase diagram of this dual-pore model has an alike shape with those of an 8 nm single

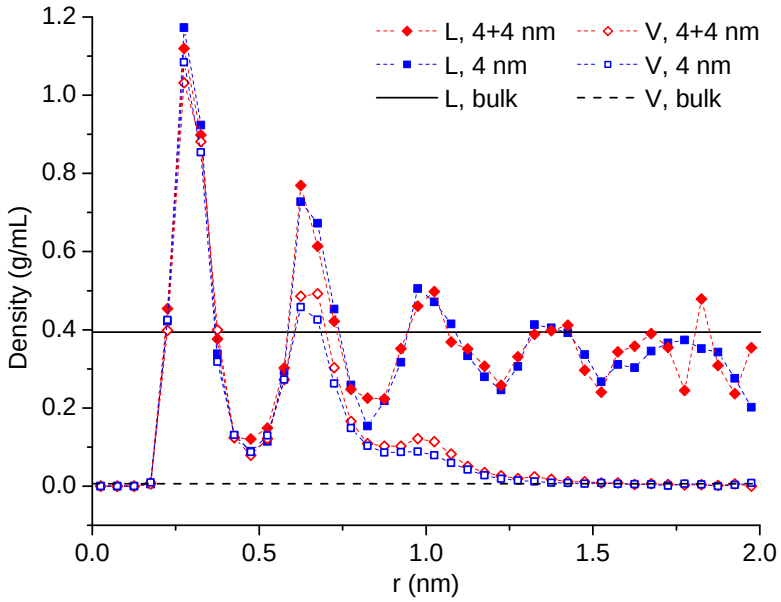

Solid, dashed lines: liquid and vapor data in bulk. Solid, empty symbols: liquid and vapor results. L: liquid state. V: vapor state. Reprinted from [16].

Figure 5.7: Density radius profiles of methane at 130 K in 4+4 pore models.

cylinder model. Although there is some divergence at lower temperatures, this 4+10 pore system has the similar performance as 8 nm single pore at fluid properties.

The fluid equilibrium properties are computed based on the van der Waals loop between the chemical potential and system density (Fig. 5.8). To have a better understanding of the filling process in this dual-pore system, four final configurations are visualized at states of stable vapor, metastable vapor, metastable liquid, and stable liquid (Fig. 5.9). At the stable vapor state with low system density, the 4 nm pore is filled up while the most molecules in the 10 nm pore belong to the adsorption layers. As the fluid system density increasing, the 4 nm pore has a denser molecular distribution and the fluid gets close to the liquid state in the 10 nm pore. This filling process provides the support to the conclusion that the smaller pores cause a stronger shift in the phase diagrams and

the liquid phase is usually condensed in the tiny pores first.

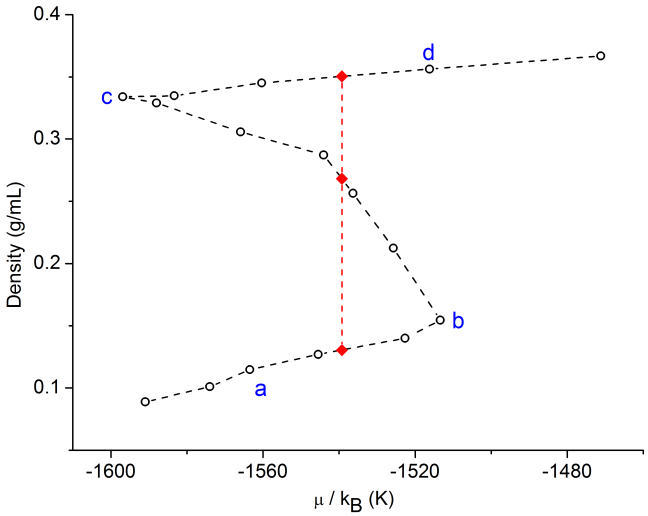

a) stable vapor, b) meta-stable vapor, c) meta-stable liquid, d)stable liquid. Circle: test data. Diamond: equilibrium points. Reprinted from [16].

Figure 5.8: μ-ρ diagram for methane at 130 K in the 4+10 model.

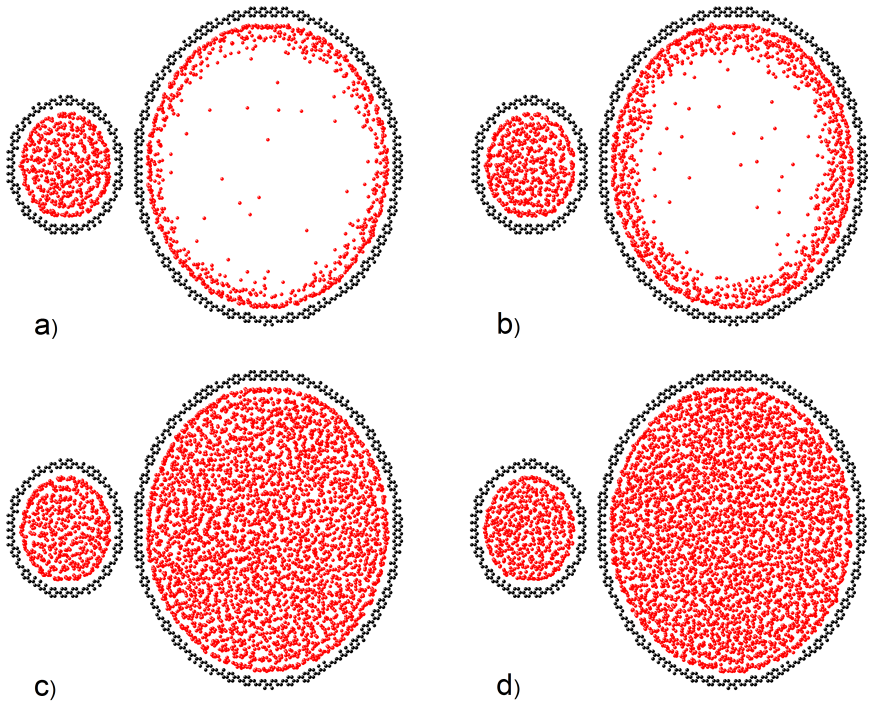

Black: graphite model. Red: methane particles. Reprinted from [16].

Figure 5.9: Top views of the molecular distribution in the states from Fig. 5.8.

4+4+10 model

For a better understanding of the shift effect difference between pores of various diameters, a triple-pore model is prepared with a combination of three diameters (4, 4 and 10 nm). As shown in Fig. 5.10, the phase diagram of this triple-pore model is shifted downward compared with the above dual-pore model (4+10). There are limited changes in the liquid densities but notable increases of vapor densities. It is clear that small pores contribute a large shift effect in the phase diagrams. In the dual-pore test, one 4 nm pore causes a downward shift effect in the phase diagram of 10 nm pore. With more small pores in the system (two 4 nm pores here), a greater shift effect will be introduced in phase diagrams. If small pores of a single diameter become dominance in the PSD, the

properties in the confined fluid system will have a similar phase behavior as the results of the single size pores (such as 4 nm pore in this case).

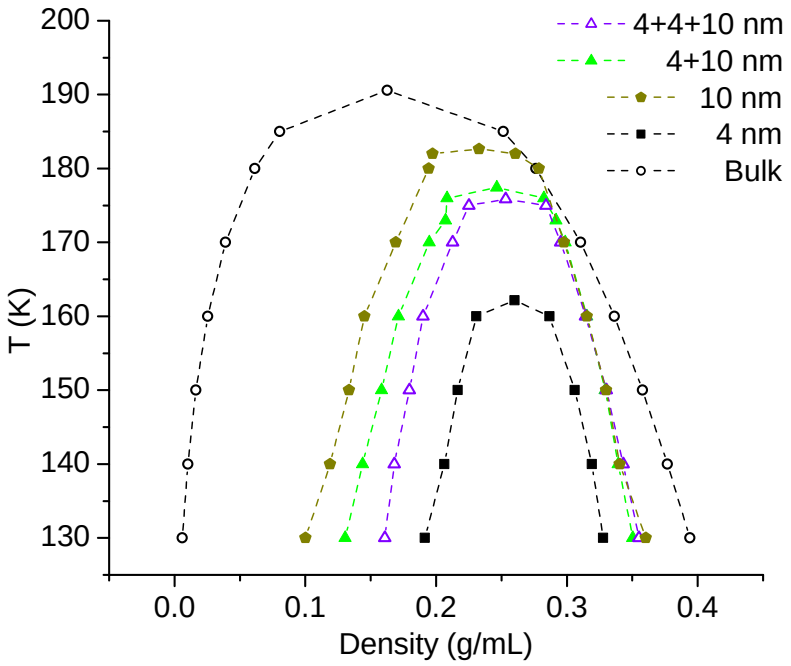

Empty circle: bulk data from NIST [104]. Square, solid triangle, empty triangle: 4 nm single pore, and multi-pore models with diameters of "4+10" and "4+4+10" nm, respectively. Reprinted from [16].

Figure 5.10: Temperature-density diagrams for methane in multi-pore models.

From the $\mu - \rho$ relationship in the shape of van der Waals shape (Fig. 5.11), the equilibrium properties are calculated based on this clear phase separation. Furthermore, the final configurations of four states on the S-shape loop are visualized to check the molecular distribution (Fig. 5.12). As stated in the previous section, the small pores have the priority over the large pores for liquid condensation. By increasing the total density of the fluid system, the density difference between pores will vanish and reach to the same

liquid values.

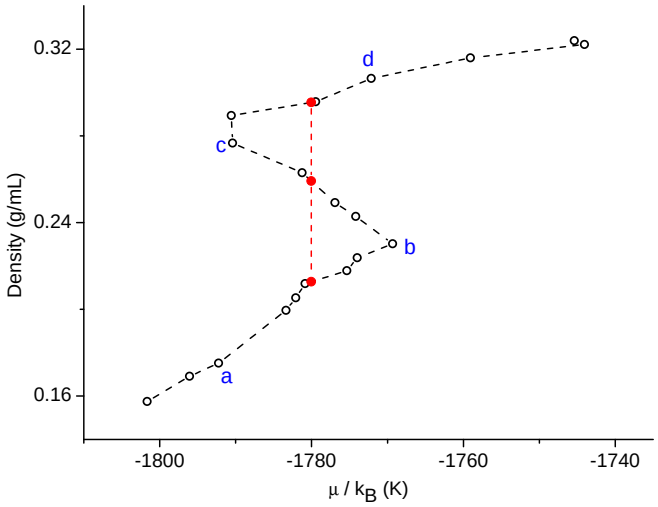

a) stable vapor, b) meta-stable vapor, c) meta-stable liquid, d) stable liquid. Circle: test data. Diamond: equilibrium points. Reprinted from [16].

Figure 5.11: μ-ρ diagram for methane at 170 K in the 4+4+10 model.

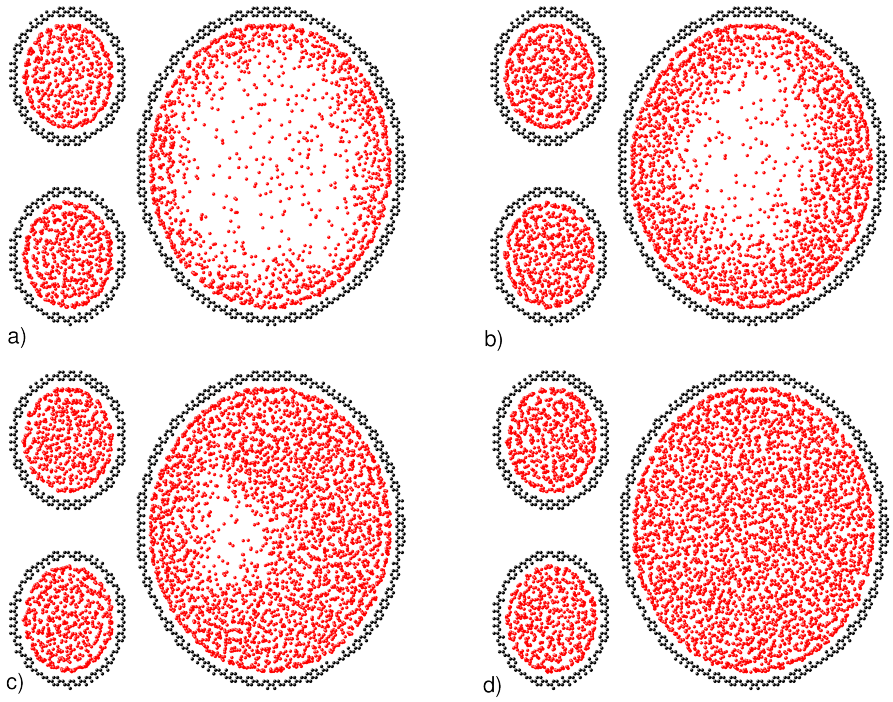

Black: graphite model. Red: methane molecules. Reprinted from [16].

Figure 5.12: Top views of the molecular distribution in the state a, b, c, and d from Fig. 5.11.

5.4 Eagle Ford model

In the real shale rock, the PSD is complicated than the previous case studies. To get a possible solution for the PSD effect on confined fluid phase behavior in a real situation, an Eagle Ford shale rock sample is studied in this section. Eagle Ford shale is a sedimentary formation as the oil and natural gas supply in south Texas. It was one of the most active unconventional production regions of U.S. in 2010. PSD data of Eagle Ford shale sample based on Hg intrusion method show the dominance of mesopores $(2 - 50\ nm)$ [7]. To simplify this PSD data into one achievable model, some specific pore diameters are picked to represent this Eagle Ford shale sample. The pore size selection

follows the rules that the pore should take a relatively large volume fraction of the PSD and have the phase behavior characteristics with a significant deviation from the bulk values. After the selection of specific pore diameters, the volume fraction of each pore diameter is calculated by minimizing the difference between the area under these discrete pore diameters and the volume fraction plot of the Eagle Ford PSD data. The Eagle Ford PSD data from Hg intrusion method are shown in Fig. 5.13 [7]. Pore diameters (4, 5, 6, 8, and 13 nm) are chosen to represent pore sizes of 3 to 4 nm, 4 to 5 nm, 5 to 6.25 nm, 6.25 to 9 nm, and 9 to 30 nm, respectively. Because of the small volume fraction and extremely large computation resource cost for molecular simulation, the pores with a diameter larger than 30 nm are not considered in this work. Also, it is reported in previous studies [31, 107] that the confinement effect is negligible for large pores, such as 30 nm in this case. Thus, the multiple pore model for this Eagle Ford sample is finalized as five independent pores with the paralleled arrangement in the Z direction and 1D periodic boundary condition. The volume fraction of each pore diameter is calculated as the ratio between the volume of the same size pores and the total system volume. The separation between pores is set as before that the molecules in a given pore have no contribution to the energy computation in other pores.

The phase diagrams are shown in Fig. 5.14 that this Eagle Ford pore model produces the similar diagram as that of a 10 nm single pore model. It is possible that this Eagle Ford sample can produce an equivalent confinement effect close to the shift effect from this 10 nm single pore. Thus, the simulations of this 10 nm single pore model could be an alternative to calculate the phase behavior and fluid characteristics of the Eagle Ford sample. Since the existence of such an alternative single pore model is the result of a case-by-case analysis, we do not claim that it is possible to find an "effective pore radius" to simplify the simulation of confined phase behavior for any rock sample.

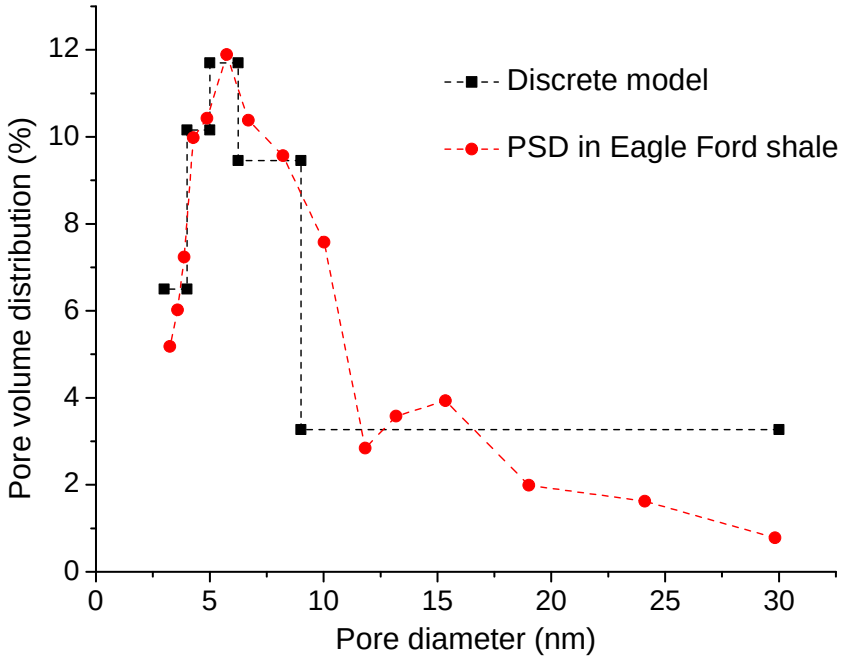

Sample data from Eagle Ford [7]. Reprinted from [16].

Figure 5.13: Pore size distribution of Eagle Ford shale samples after normalization.

The $\mu - \rho$ relationship is again obtained in the shape of van der Waals loop (Fig. 5.15). These two diagrams from Eagle Ford model and 10 nm single pore model are not identical but happen to generate the similar equilibrium points. In addition, the filling process is investigated through the molecular distribution of the system final configuration at different states (Fig. 5.16). As described in the last section, the liquid condensation will happen in small pores first. In all simulations, the Eagle Ford pore model is treated as a black box, in which only the thermodynamic relationship of $\mu - \rho$ is used to define the phase separation and to calculate the fluid equilibrium properties. Therefore, the phase behavior of the fluid in one pore may be different from the phase behavior of the whole fluid system. For example, in Fig. 5.16a, the liquid condensation already happens in small

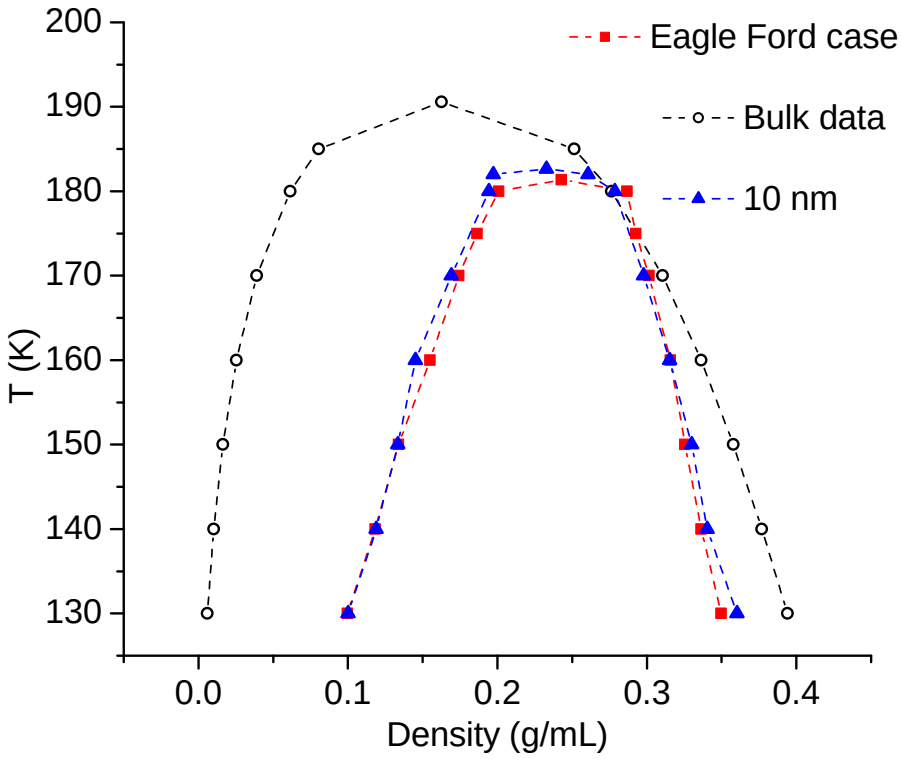

Empty circle: bulk data from NIST [104]. Square, triangle: results from Eagle Ford model and a 10 nm single pore model, respectively. Reprinted from [16].

Figure 5.14: Temperature-density diagrams for methane in an Eagle Ford pore model.

pores while the whole system is in the vapor state. Since these thermodynamic properties are defined as averages over the system, it is not possible to know these details from the $\mu - \rho$ relationship. Furthermore, the molecules are in dynamic equilibrium between small and large pores in any state. Because of the influence from other pores of different diameters, the phase behavior of fluids in one single pore of the multiple pore system is not the same as that in a single pore system of this diameter.

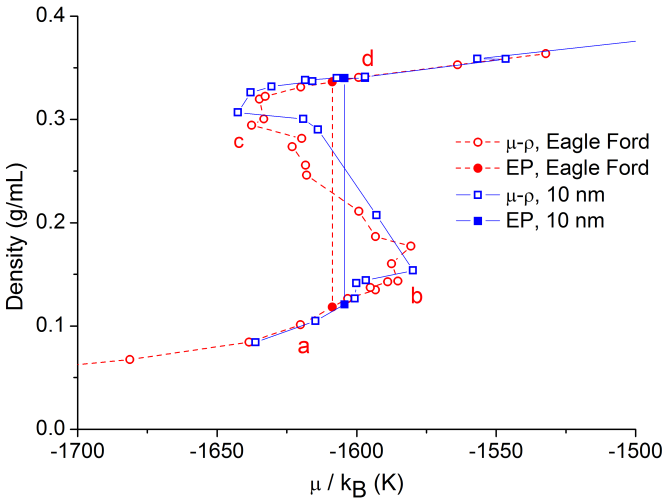

Molecular distribution in test a) stable vapor, b) meta-stable vapor, c) meta-stable liquid and d) stable liquid of Eagle Ford model are shown in the next figure. EP: equilibrium points. Reprinted from [16].

Figure 5.15: μ-ρ diagram for methane at 140 K in Eagle Ford and 10 nm single pore models.

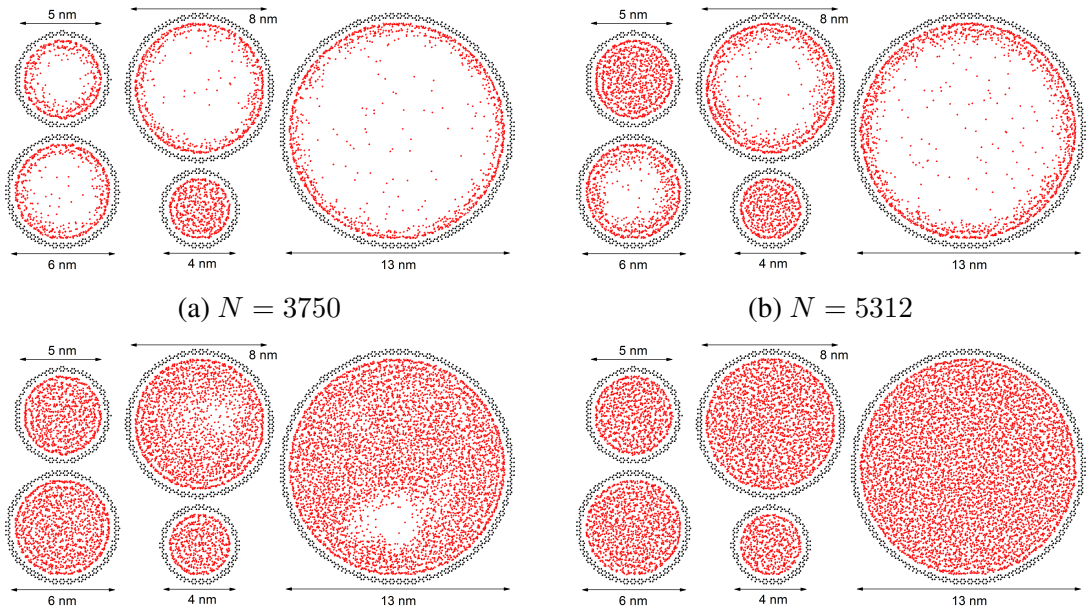

(a) $N = 3750$ (b) $N = 5312$

(c) $N = 12812$ (d) $N = 14875$

Methane at 140 K in the state a, b, c, and d from Fig. 5.15. N: total molecular number. Reprinted from [16].

Figure 5.16: Top views of the molecular distribution in Eagle Ford model.

6. PHASE BEHAVIOR IN SHALE ORGANIC AND INORGANIC NANOPORES*

In previous work, the shale is usually built as a simple model without the consideration of the material effect on phase behavior. To have a better understanding of phase diagrams in different shale environments, the gauge-GCMC method is chosen to perform phase behavior simulations of pure fluids (C_1, C_3) and one ternary case ($C_1/C_3/nC_5$) based on two types of nanopore models (slit and cylinder), which are generated from three different boundary materials (two inorganic minerals and one kerogen). Two minerals (quartz and calcite) are adopted for inorganic matter. A kerogen model is generated through molecular dynamics (MD) simulation and used as a rigid matrix in the MC simulation. Usually, pore size distribution in shale is reported based on the cylinder pore model assumption [10, 11]. Also, the slit model is widely used in the simulations. Thus, these two shapes of pore model are covered in this work.

6.1 Simulation setting

In shale, the organic matter consists of hydrocarbon, kerogen, asphaltene/resin, carbon dioxide and water [108, 109], in which the kerogen takes a great portion of the composition of shale organic material and is defined as the part of organic matter which is insoluble in dichloromethane. To understand the phase behavior of hydrocarbon fluids inside organic nanopores, kerogen is chosen to build a simplified model to represent the organic matter in shale. The possible molecular structures of kerogen compose of

*Part of the data reported in this chapter is reprinted with permission from "Phase Behavior in Shale Organic and Inorganic Nanopores From Molecular Simulation" by Bikai Jin and Hadi Nasrabadi, 2017. *SPE Annual Technical Conference and Exhibition*, 9-11 October, San Antonio, Texas, USA, Copyright [2017] by Society of Petroleum Engineers, Inc.

polyaromatic units linked by alkyl, ether, sulfur bridge and naphthenic [110]. Considering the atom ratios and functional groups of molecules from experimental data, a complex molecular structure consisting of 481 atoms has been proposed as a generic model for type II kerogen [108]. With the formula of $S_2C_{242}N_5O_{13}H_{219}$, the configuration of this molecule is shown in Figure 6.1a.

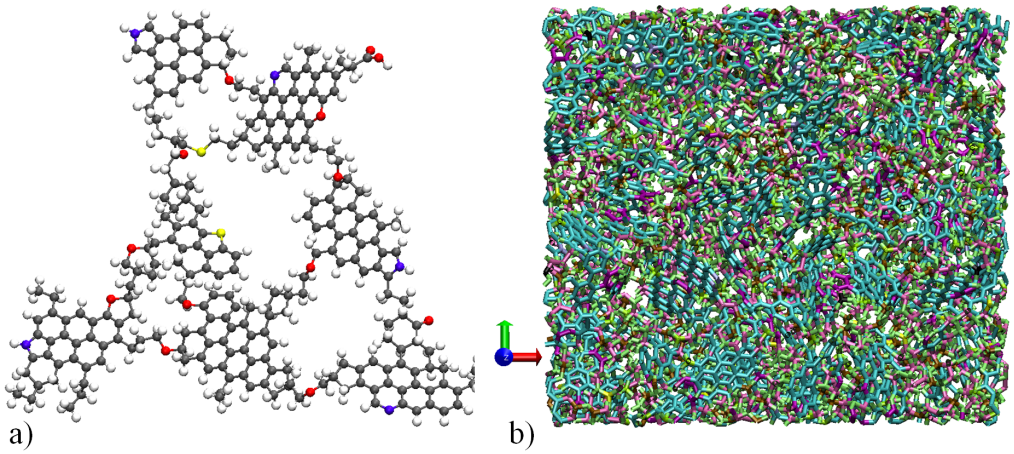

a) Molecular model with $M_W = 3469.6\ g/mol$. Gray, white, red, yellow, blue: carbon, hydrogen, oxygen, sulfur and nitrogen atoms, respectively. b) Final configuration of the kerogen material at the shale reservoir condition. Enlarged atom sizes for better visualization. Reprinted from [111].

Figure 6.1: Schematic of type II kerogen model.

To generate the nanopore model of kerogen material, 24 kerogen molecules are used to perform an annealing simulation from high temperature and high pressure to a typical reservoir situation of Eagle Ford [112–114]. This simulation is conducted in a cubic box with 3D periodic boundary condition and an initial density of $0.27\ g/mL$ based on molecular dynamic technique of LAMMPS software. Considering the Wäldman and Hagler mixing rules for unlike particles [115], the intermolecular interaction is

Table 6.1: MD simulation setting of kerogen material model generation.

ensemble	T (°F)	t (ps)*	P (psia)
NVT	1160.3	50	
NPT	1160.3	200	6500
NPT	800.3	200	6500
NPT	440.3	400	6500
NPT	330	400	6500

*: simulation time in picosecond.
Reprinted from [111].

computed on the basis of the all-atoms pcff+ force field for Lennard-Johns (LJ) 6-9 model [116, 117]. The intramolecular and electrostatic interactions are also included in the energy computation while the cutoff distance is set at 0.95 nm. For LJ potential and electrostatic energy beyond the cutoff, the long-term correction [58] and PPPM method [118] are used in the simulation. System temperature and pressure are constant input parameters and maintained by Nose/Hoover thermostat [119] and barostat [120]. This molecular dynamics simulation is divided into several stages and listed in Table 6.1. An NVT ensemble simulation is performed at the beginning as a relaxation or melting process at 1160.3 °F. Several NPT simulations are conducted one-by-one with a stepwise temperature reduction from 1160.3 °F to 330 °F. The final configuration of this kerogen material is shown in Fig. 6.1b with density $1.16\ g/mL$.

For the inorganic matters of shale, only quartz and calcite are studied in this work (Fig. 6.2). Quartz takes the highest percentage in the composition of shale inorganic matter and also serves as one of the most common minerals on earth's surface [121, 122]. α-quartz with the cell parameters ($a = 0.49133\ nm$, $c = 0.54053\ nm$, $\alpha = \beta = 90.0°$, $\gamma = 120.0°$) is used as the material cell model with a trigonal crystal structure of a $P3_121$

space group for the left-handed crystal.

Calcite is one kind of carbonate mineral which has a high portion of the shale composition. Based on the trigonal crystal system with R$\bar{3}$c space group [122], the cell parameters are listed as follows: $a = 0.49896\ nm$, $c = 1.7061\ nm$, $\alpha = \beta = 90.0°$, $\gamma = 120.0°$ (Fig. 6.2b).

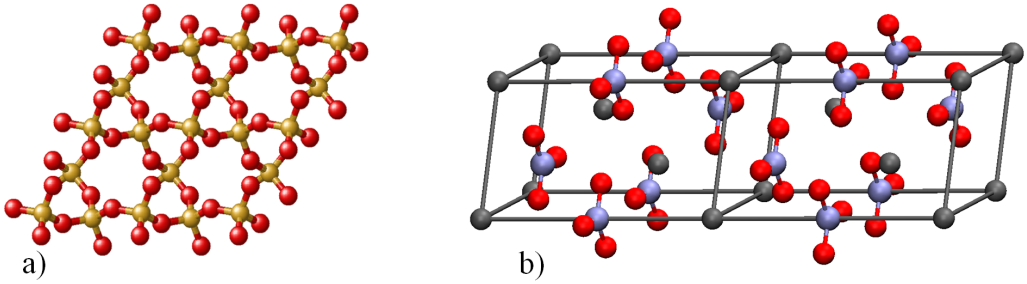

a) α-quartz molecular structure. Red and orange: oxygen and silicon atoms. b) Calcite molecular structure. Gray, blue and red: calcium, carbon, and oxygen atoms, respectively. Reprinted from [111].

Figure 6.2: Schematics of α-quartz and calcite.

Based on the molecular structures of these three materials, two kinds of pore models (slit and cylinder) are generated as shown in Fig. 6.3. By repeating the material cell model in one 2D surface, the single layer of the molecular boundary is constructed and put at the top and bottom of the simulation box to form the slit pore models of quartz and calcite. Slit pore model of kerogen is built by cutting out redundant atoms from a box saturated with the kerogen material. The distance between the two molecular layers is defined as the diameter of slit pore. Also, the cylindrical models with specific diameters and thicknesses are cut from saturated cubes of these three materials. The gauge meter is

set up in bulk condition while the cylinder and slit models are only conducted in the fluid system box with 1D and 2D periodic boundary conditions, respectively.

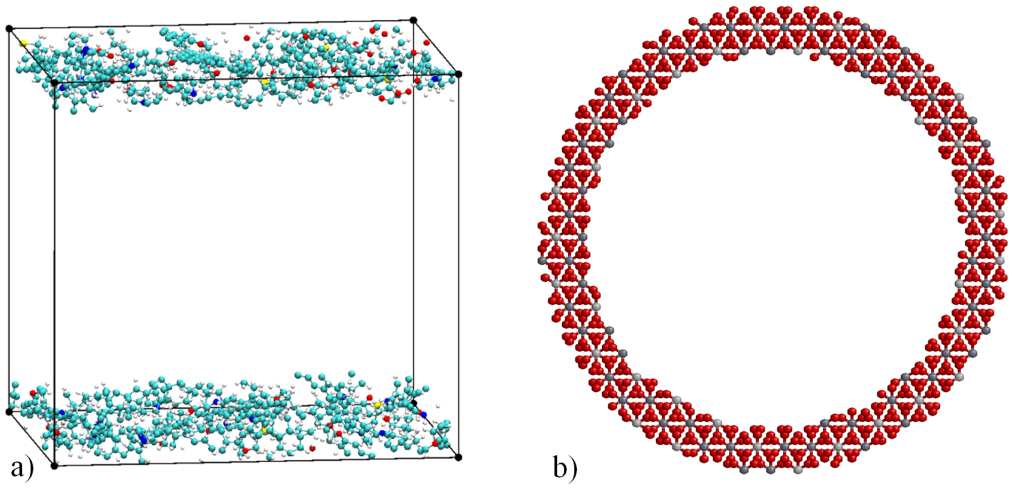

a) Slit pore model of kerogen material. Several pseudo atoms are included to provide the cube frame. The pore diameter is defined as the distance between the top and bottom molecular layers. b) Plain view of cylinder model based on quartz material. The diameter is defined as the inner diameter. Reprinted from [111].

Figure 6.3: Schematic representation of two pore models.

6.2 Single component fluids

Two single component fluids (methane, propane) are used to study the confined phase behavior in this section based on the slit and cylindrical pore models with diameters of 4, 7 and 10 nm. Gauge-GCMC method is used in the simulation that a set of tests are conducted with different molecular numbers as input parameters. Based on the $\mu - \rho$ relationships at various temperatures, the equilibrium properties are finalized and shown as the phase diagrams for each model. As plotted in Fig. 6.4, confined phase diagrams are shifted downward while the vapor densities are increased and liquid densities are

decreased. The critical temperature is reduced and the critical densities have greater values as previously described. Based on the results in pores of three diameters, it can be concluded that the confinement effect will vanish when the pore diameter becomes sufficiently large.

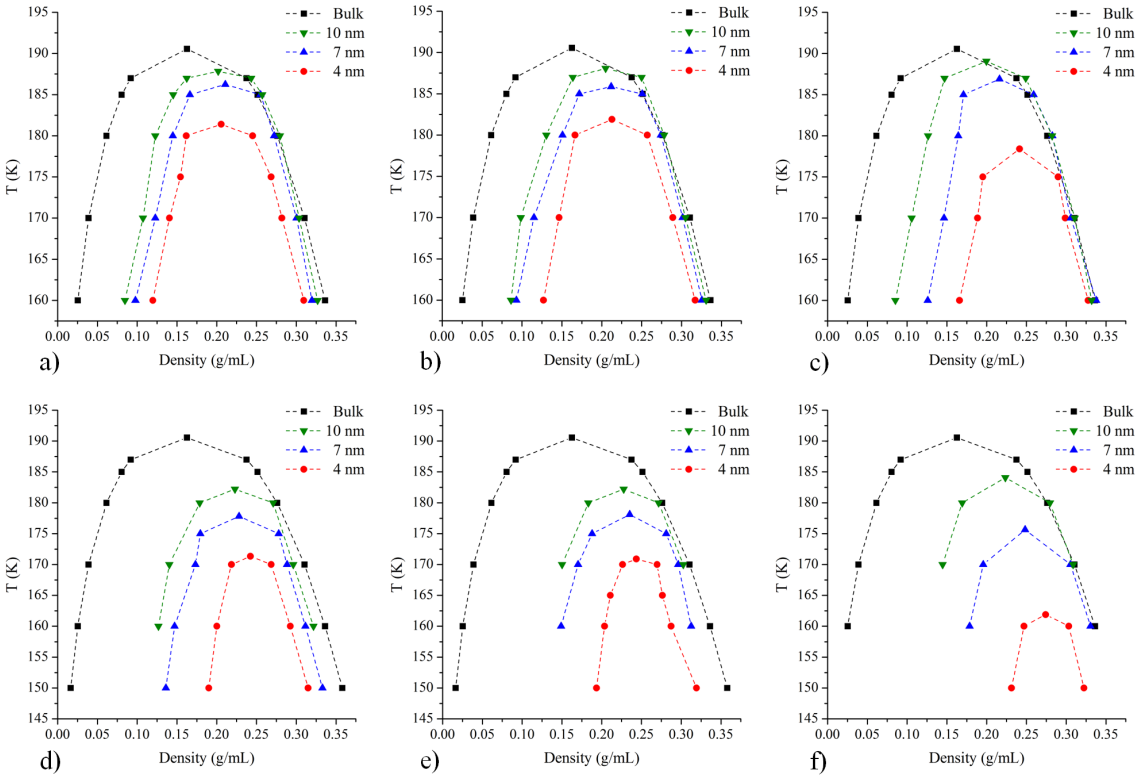

Top, bottom: results of slit and cylinder pores. Left, middle, and right: results for quartz, kerogen, and calcite pore, respectively. Reprinted from [111].

Figure 6.4: Phase diagrams for methane.

Comparing the simulation results from two kinds of pore models (Fig. 6.4), it is obvious that the cylindrical pores can provide more confinement effects on the fluids and cause a stronger shift effect on phase diagrams. Because the cylindrical model can

provide more inner surface than that of slit pore based on the same pore volume, the constraint inside the cylinder is stricter than that in the slit model. Based on the difference between results from pores of three materials, there is more offset in the phase diagrams of methane in the calcite pores while the phase diagrams from quartz pores are similar to those from kerogen pores. This divergence of adsorption effect results from the different contributions of molecular models in the energy computation. Based on the force field of Xiao [123], the potential parameter of calcium atom ($\varepsilon/k_B = 240.5925\ K$) is larger than that of other atoms. This strong adsorption setting results in the notable shift effect on the phase diagrams of calcite models. These above observations are also available from phase diagrams of propane in Fig. 6.5.

Additional GCMC simulations are conducted at the equilibrium chemical potentials to generate the fluid density distributions of methane in liquid and vapor states. In the tests of 4 nm slit pore at 170 K (Fig. 6.6), the point with the distance of zero is set at the pore boundary surface of the bottom layer while an interval size of 0.1 nm is used in the calculation of histogram data. The density profiles from three material models have the similar distribution of two peaks near the pore surfaces in both vapor and liquid phases. These density distribution differences between confined and bulk data are reduced when increasing the distance from pore boundaries. Note that the calcite pore models cause a larger peak value, which is resulted from a stronger adsorption effect. Comparing the results from two phases, there are more molecules in the box center of liquid phase than that of the vapor phase. It is possible that the fluid molecules in the box center have a larger probability to be recovered than those in the adsorption layers. The peaks near the pore boundary are also observed in the density radius profiles from tests of 7 nm cylindrical pores at 160 K (Fig. 6.7). Comparing the density distributions in slit and cylinder pores, the results from calcite pore models provide more constraints in the fluid

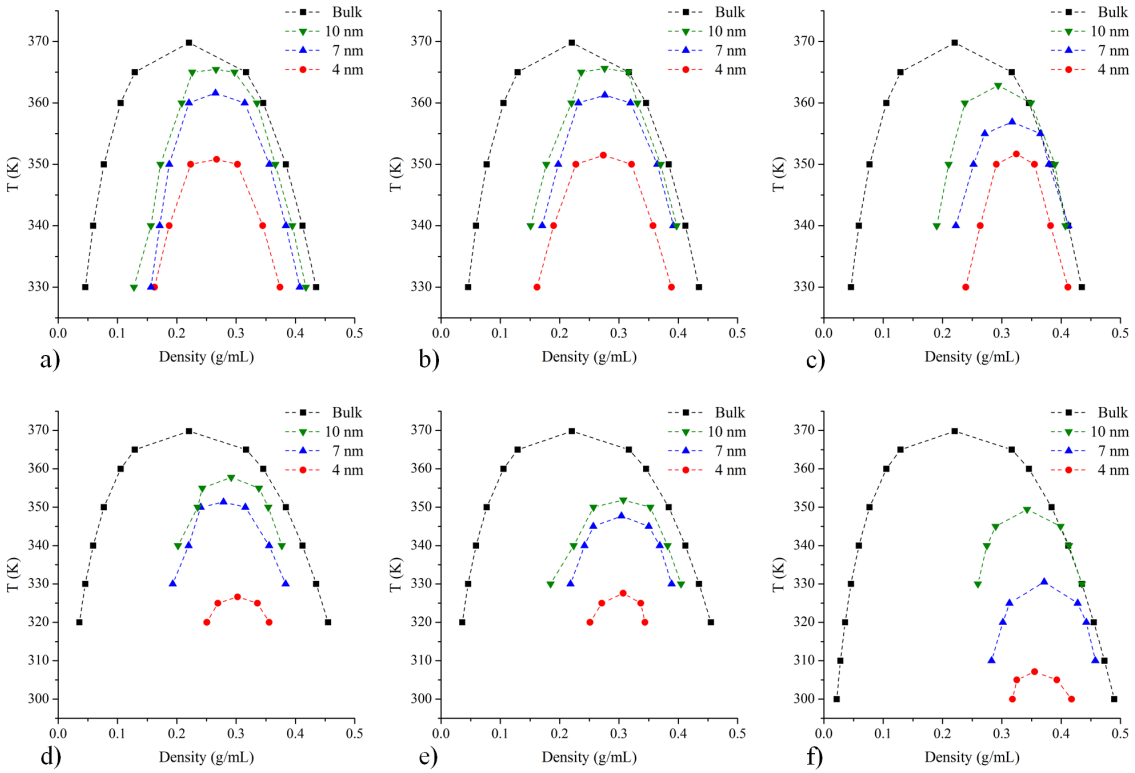

Top, bottom: results of slit and cylinder pores. Left, middle, and right: results of quartz, kerogen, and calcite material, respectively. Reprinted from [111].

Figure 6.5: Phase diagrams for propane.

distribution than that of other two materials.

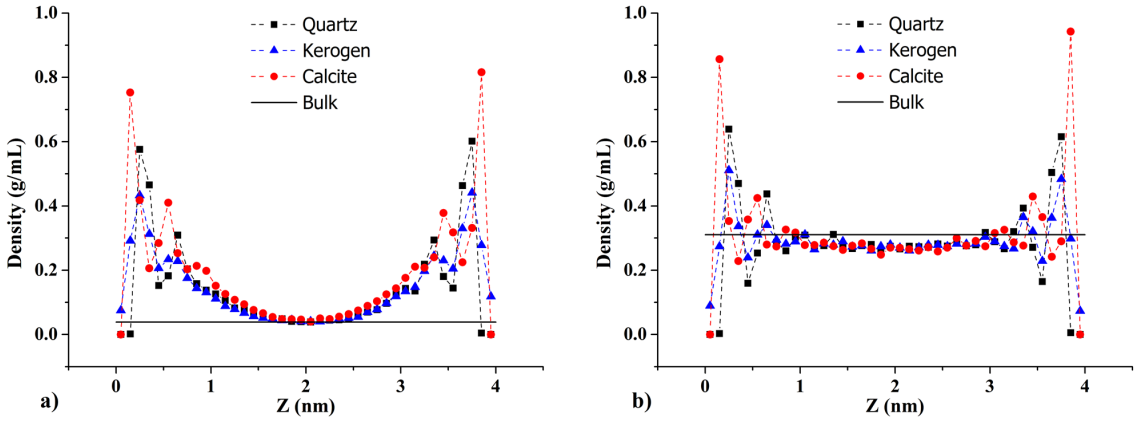

a) Vapor state, b) Liquid state. Bulk data are from NIST. Reprinted from [111].

Figure 6.6: Density profile of methane at 170 K in 4 nm slit pore with different pore materials.

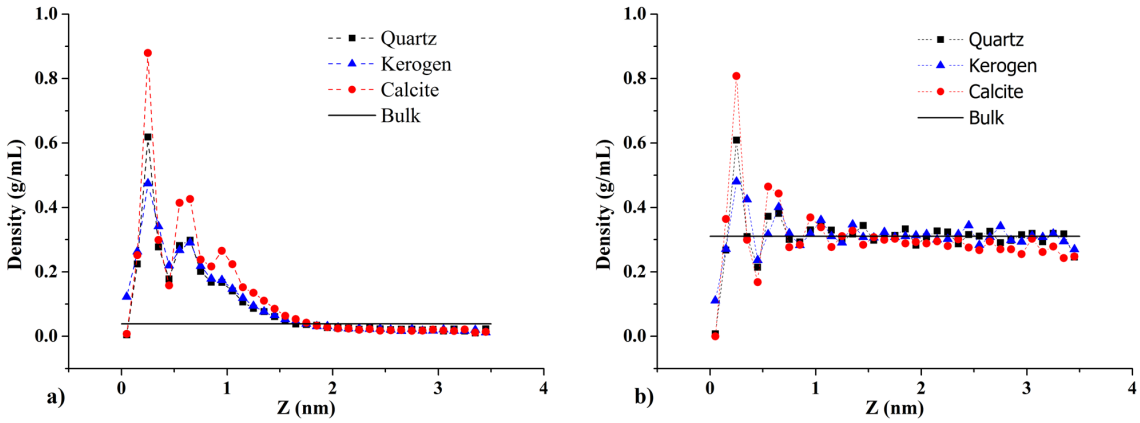

a) Vapor state, b) Liquid state. Bulk data are from NIST. Reprinted from [111].

Figure 6.7: Density radius profile of methane at 160 K in 7 nm cylinder pore with different pore materials.

6.3 Ternary fluids

To understand the different constraints on complex fluids from three material models, the gauge-GCMC method is used in one ternary fluid simulation (C1: methane, C3: propane, nC5: n-pentane) in 4 nm slit and cylinder pores. The accuracy of gauge-GCMC is confirmed with data of PR EOS in previous chapters for multiple component fluids. Input parameters are $T, V, \mu_{C_1}, \mu_{C_3}, N_{nC_5}$ for this fluid case. Based on different sets of molecular number N_{nC_5} for several combinations of (μ_{C_1}, μ_{C_3}), the $\mu_{nC_5} - \rho$ relationships are prepared for equilibrium properties computation. As shown in Fig. 6.8, the constraints of 4 nm slit pores are introduced in the fluid phase diagrams based on three materials model with the initial setting ($T = 160$ °F, $\mu_{C_1}/k_B = -4450\ K$). Inside the slit pores, there is a dramatic change in the composition of confined vapor phase while no significant change occurs in the liquid composition. The shifts of vapor composition results from the increased nC_5 molecules in the adsorption layers. It is a reasonable inference that the confined critical points will compositions of a smaller portion of C_3 and a larger percentage of C_1 and nC_5. From the composition-density diagrams (Fig. 6.9), the density differences under confinement are reduced between two phases. It is obvious that the fluid critical points will have larger densities in slit pores than the values in bulk.

By comparing the ternary and $\rho - C_3\%$ diagrams, the calcite model provides stronger confinement effect on the fluid while the other two models have the similar constraints. This observation is also supported by the density profiles in the vertical direction (Fig. 6.10). Similar to the density profiles of pure fluids, there are two peaks in the distributions near the pore boundaries. In the center region, the confined densities approach the values in bulk condition. Also, the peaks of the vapor profiles in calcite models have larger values than that in other two models. However, since the adsorption layers are fully saturated

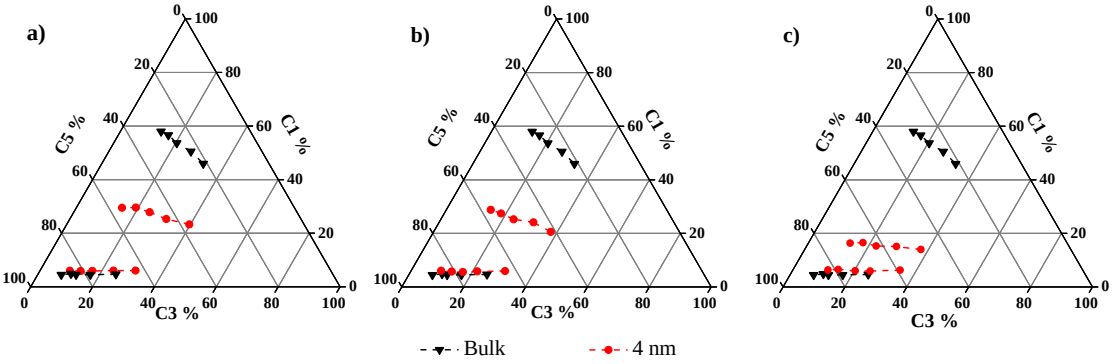

$T = 160$ °F, $\mu_{C_1}/k_B = -4450\ K$. Results of slit pore based on a) Quartz, b) Kerogen, and c) Calcite. Triangle, circle: simulation data in bulk and under confinement. Reprinted from [111].

Figure 6.8: Ternary diagrams of the $C_1/C_3/nC_5$ system in 4 nm slit pores.

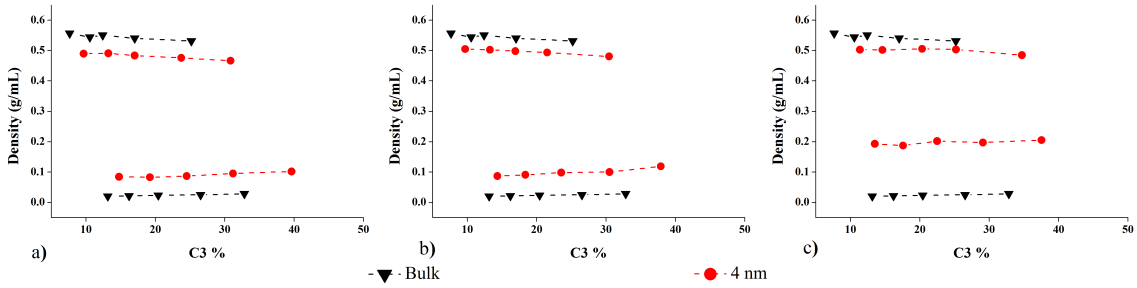

$T = 160$ °F, $\mu_{C_1}/k_B = -4450\ K$. Results of a) Quartz, b) Kerogen, and c) Calcite. Reprinted from [111].

Figure 6.9: Composition-density diagrams of the $C_1/C_3/nC_5$ system in 4 nm slit pores.

in the liquid state, the peak values are quite similar to each other. Detailed information about the molecular distribution is shown in Fig. 6.11 for each component. Heavier components (C_3 and nC_5) have a larger molecular number in the vapor phase of calcite models compared to their molecular number in quartz and kerogen pores. However, each component of the liquid phase has similar molecular distribution in pore models based on the three materials.

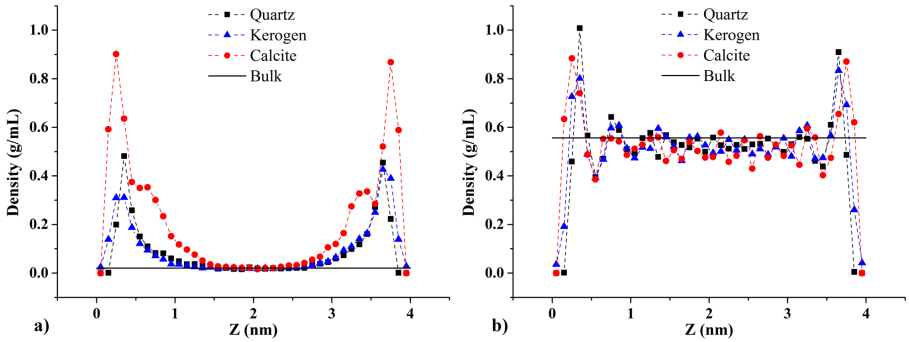

$\mu_{C_1}/k_B = -4450\ K$, $\mu_{C_3}/k_B = -4700\ K$. a) Vapor state, b) Liquid state. Bulk data are from NIST. Reprinted from [111].

Figure 6.10: Density profile of the $C_1/C_3/nC_5$ fluid at 160 °Fin 4 nm slit pore.

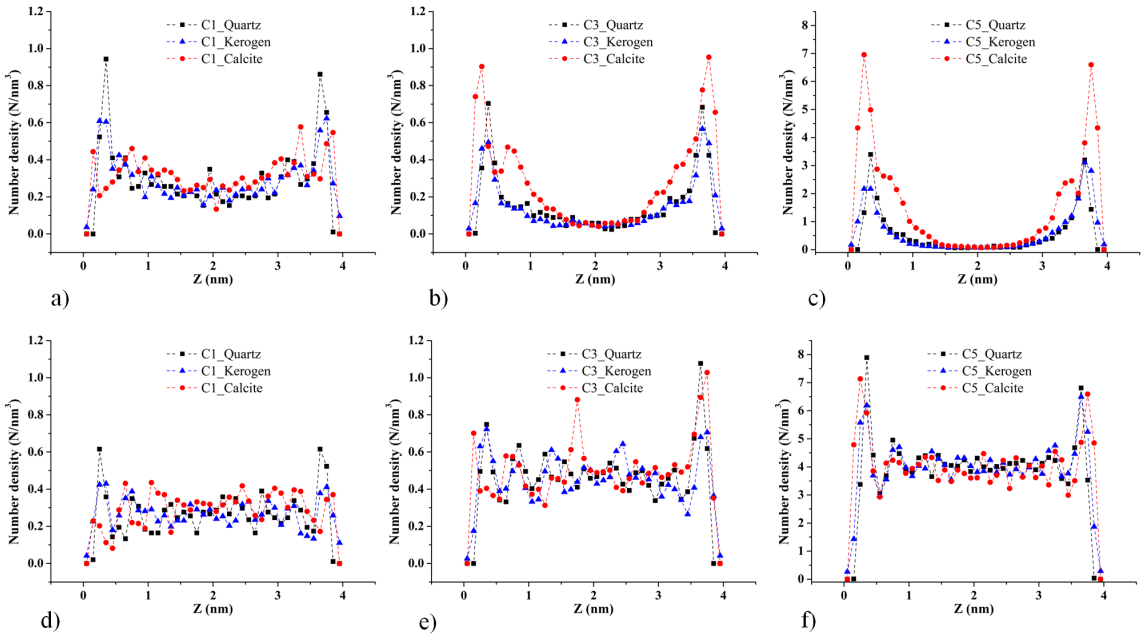

$T = 160$ °F, $\mu_{C_1}/k_B = -4450\ K$, $\mu_{C_3}/k_B = -4700\ K$. Top: Vapor state, bottom: Liquid state. Left, middle, right: the distribution of C_1, C_3, nC_5, respectively. Reprinted from [111].

Figure 6.11: Molecular number distribution of the $C_1/C_3/nC_5$ fluid in 4 nm slit pore.

To better understand the confinement effect on the phase behavior of this ternary fluid, a 4 nm cylindrical pore model is introduced in the simulations at the same initial condition ($T = 160$ °F, $\mu_{C_1}/k_B = -4450\ K$). As shown in Fig. 6.12, the ternary diagrams are shifted in the same trend as that in the slit pore tests, those nC_5 compositions are increased in the vapor phase and the liquid compositions have small changes. From the comparisons of ternary diagrams (Fig. 6.12) and $\rho - C_3\%$ relationships (Fig. 6.13) from three models, the boundary model of calcite material results in a more intense shift than that of the other two materials. The radius density distributions have the unimodal shape with peak values similar to those in the slit pores (Fig. 6.14). Again, the peak values are larger in calcite pore models while similar density distributions are observed in other two pore models. Comparing the results of slit pores (Fig. 6.8, 6.9) and those of cylinder models (Fig. 6.12, 6.13), it is obvious that cylinder models can provide more constraints on fluids and result in larger density changes. In the molecular distribution of each component in two phases (Fig. 6.15), heavier components (C_3 and nC_5) have a larger concentration in calcite models while they have similar distributions in the other two materials. Based on the molecular distributions of C_1 in slit and cylinder pores (Fig. 6.11 and 6.15), the difference in material does not cause a notable change in the distribution of methane molecules.

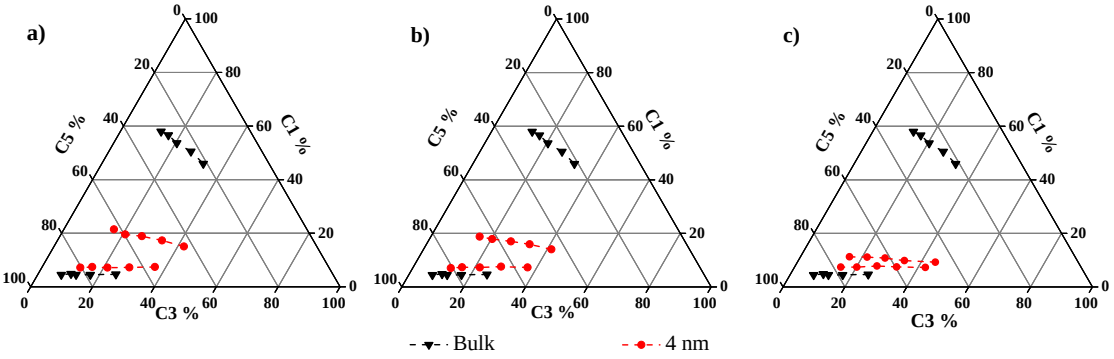

$T = 160$ °F, $\mu_{C_1}/k_B = -4450\ K$. Results of cylinder pores based on a) Quartz, b) Kerogen, and c) Calcite. Triangle, circle: simulation data in bulk and under confinement. Reprinted from [111].

Figure 6.12: Ternary diagrams of the $C_1/C_3/nC_5$ system in 4 nm cylinder pores.

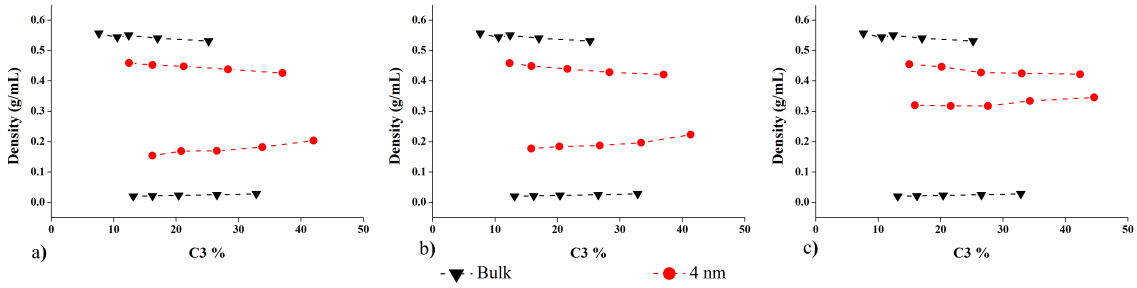

$T = 160$ °F, $\mu_{C_1}/k_B = -4450\ K$. Results of a) Quartz, b) Kerogen, and c) Calcite. Reprinted from [111].

Figure 6.13: Composition-density diagrams of the $C_1/C_3/nC_5$ system in 4 nm cylinder pores.

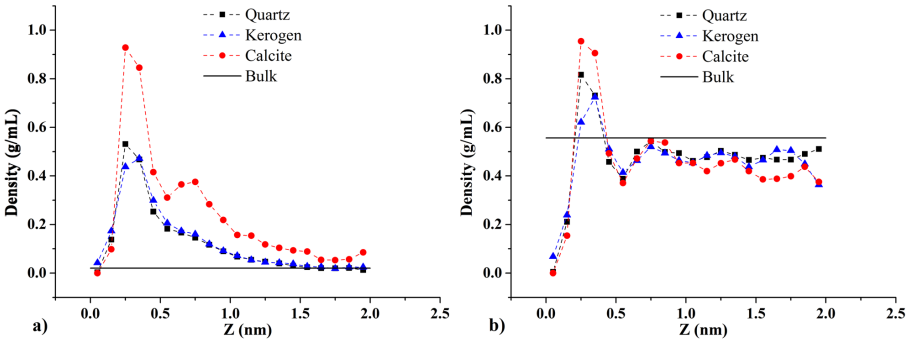

$\mu_{C_1}/k_B = -4450\ K$, $\mu_{C_3}/k_B = -4700\ K$. a) Vapor state, b) Liquid state. Bulk data are from NIST. Reprinted from [111].

Figure 6.14: Density profile of the $C_1/C_3/nC_5$ fluid at 160 °Fin 4 nm cylinder pore.

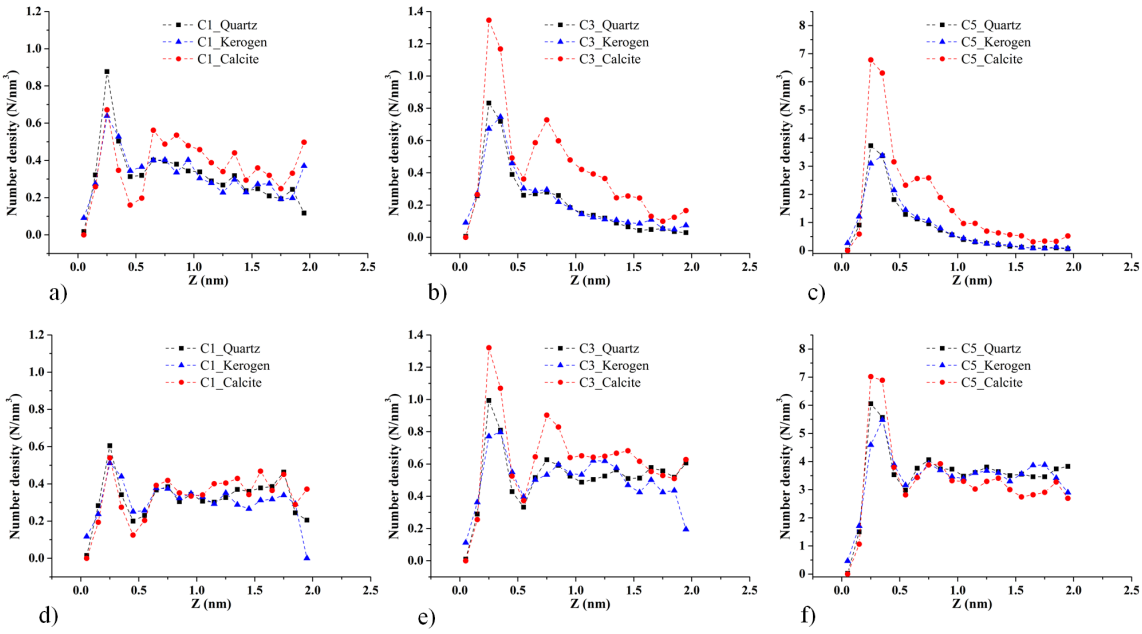

$T = 160$ °F, $\mu_{C_1}/k_B = -4450\ K$, $\mu_{C_3}/k_B = -4700\ K$. Top: Vapor state, bottom: Liquid state. Left, middle, right: the distribution of C_1, C_3, nC_5, respectively. Reprinted from [111].

Figure 6.15: Molecular number distribution of the $C_1/C_3/nC_5$ fluid in 4 nm cylinder pore.

In the above tests, the temperature ($T = 160$ °F) is lower than the possible values in shale reservoirs. To get a better description of fluid phase behavior in shale reservoir condition, two additional group tests are conducted at one typical shale temperature ($T = 290$ °F) by using slit and cylinder pores with the three materials. All other input parameters are kept the same as used before. In the cylinder pore tests, there is no phase separation observed at the given conditions. Usually, the energy barrier between liquid and vapor phases will decrease and the density difference between two phases is reduced as fluid temperature increases. Compared with slit pore results, vapor phase in cylinder pores has a larger density because more boundary surface area results in stronger adsorption contribution. Thus, it is possible that at this specific temperature, the fluid is close to or beyond the critical point and there is only one phase for fluids in cylinder pores. It has also been reported in [28] that confinement-induced supercriticality was observed during the experiments of hydrocarbons in nanopores.

For slit pore results, the similar confinement effects that the vapor phase has a higher composition of nC_5 while liquid densities are reduced and vapor densities are increased are observed. As shown in Fig. 6.16 and 6.17, the calcite slit pores cause stronger confinement effects than those of the other two materials. Comparing the results of slit pores at two temperatures (Fig. 6.9, 6.17), the density difference between two phases is reduced as expected when the temperature is increased.

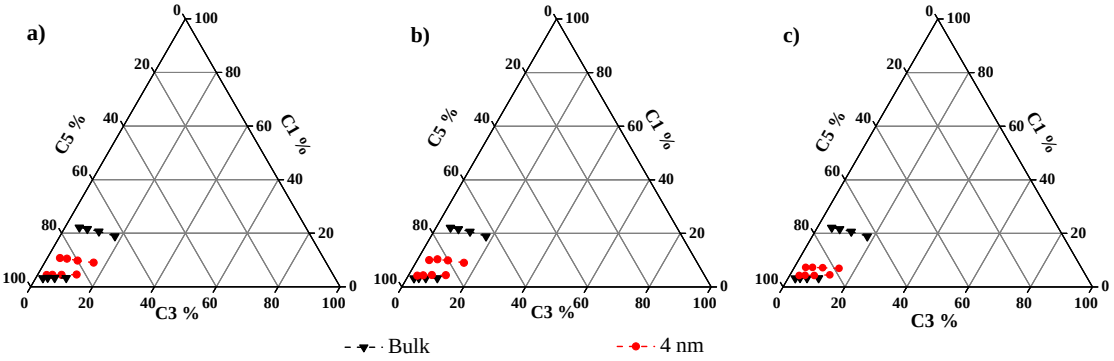

$T = 290$ °F, $\mu_{C_1}/k_B = -5700\ K$. Results of cylinder pores based on a) Quartz, b) Kerogen, and c) Calcite. Triangle, circle: simulation data in bulk and under confinement. Reprinted from [111].

Figure 6.16: Ternary diagrams of the $C_1/C_3/nC_5$ system in 4 nm slit pores.

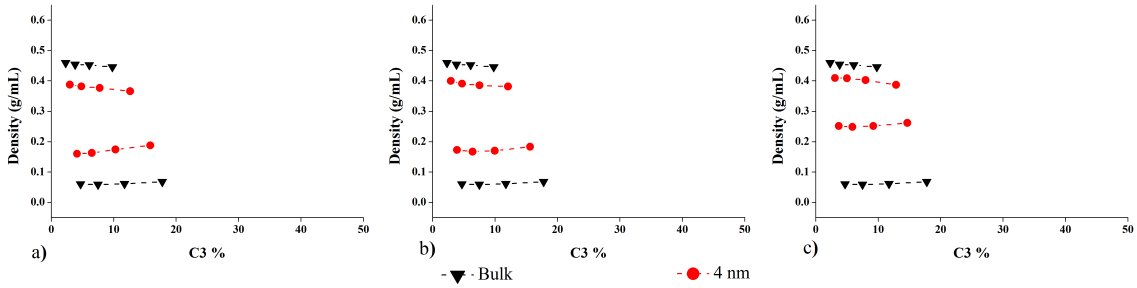

$T = 290$ °F, $\mu_{C_1}/k_B = -5700\ K$. Results of a) Quartz, b) Kerogen, and c) Calcite. Reprinted from [111].

Figure 6.17: Composition-density diagrams of the $C_1/C_3/nC_5$ system in 4 nm slit pores.

7. SUMMARY AND FUTURE WORK

Knowledge of hydrocarbon phase behavior is essential in the oil and gas industry. However, it is not well studied in shale situations compared with that in bulk conditions. To have an in-depth understanding of fluid phase behavior under confinement, Monte Carlo molecular simulation methods are chosen in this work to investigate the confined phase behavior of fluids in shale.

In chapter 2, after the study about several popular Monte Carlo methods, a novel method, gauge-GCMC, is designed for phase behavior simulation of multiple component fluids. This method is developed from the gauge-GEMC method and has the advantage that it is capable for the simulation of complex fluids and requires fewer computations for the phase behavior determination when compared with other methods.

In chapter 4, based on the slit-pore model of graphite material, the new method gauge-GCMC is applied for phase behavior simulations in bulk and confined conditions of pure fluids (C_1, C_2), a binary system (C_1/C_2), and one ternary case ($C_1/C_3/nC_5$). The accuracy of this new method is verified by comparing its results with those of other Monte Carlo methods and theoretical data. From all case studies under confinement, the typical results obtained apply to other fluids, that the liquid densities are reduced while the vapor densities are increased. Confined critical points are extrapolated with smaller densities comparing with the bulk values. The above conclusions are supported by the density profiles, in which peaks are formed near the pore surface. For pure systems, the critical temperatures are shifted downward and the phase diagrams approach its bulk data as the pore diameter increases. For a binary system, the critical point under confinement

has a lower C_1 composition. For a ternary fluid, the critical point in a 4 nm slit pore has a higher composition of C_1 and nC_5, but a smaller C_3 composition. Based on the results of binary and ternary systems, it is inferred that heavier components have a stronger adsorption effect than lighter components and have a significant contribution to the phase density differences under confinement.

In chapter 5, to investigate the PSD effect on confined phase behavior, the gauge-GCMC simulations are conducted for methane in shale nanopore systems which are represented by cylindrical models consisting of two types of pore models (single pore and multiple pores). The results from single pore models are similar to those in chapter 4, in that the density difference between liquid and vapor phases are reduced while the critical points are shifted to small temperatures and large densities under confinement. In the tests of multiple-pore models, the same shift trends are observed in the phase diagrams as stated above. For the 4+10 model, it may be possible that this model has similar properties to those of an 8 nm single pore. For the Eagle Ford field example, a five-pore model is built by discretizing the PSD data from experiments. This model can produce a phase diagram similar to that of a 10 nm single pore. According to all case studies, it is concluded that small pores have priority over large ones in being filled up, with the liquid condensation initially occurring in the small pores. Small pores can result in a greater shift on phase diagrams than other large pores. If the system contains more small pores, a larger shift will be introduced in the phase diagram due to the confinement effect.

In chapter 6, the gauge-GCMC simulation method is used to study the boundary material effect on the fluid phase behavior in shale nanopores. Two types of pore models (slit and cylinder), which are generated from three kinds of material (quartz, calcite,

kerogen), are used in the phase behavior simulation of pure fluids (methane and propane) and one ternary fluid in several conditions. For all fluid tests, vapor densities are increased and liquid densities are reduced in both slit and cylinder pores of three materials. Cylinder pores provide more adsorption surface area which results in a stronger confinement effect on the fluid phase behavior, compared with results of slit pores. Based on the results from three materials, calcite has the stronger shift effect while the other two materials contribute similar constraints on the phase diagrams. For ternary fluid tests, vapor phase has a large increase in the nC_5 composition while there are only small changes in the liquid phase composition. The critical points are extrapolated with larger densities and nC_5 compositions, compared with bulk data. In a group of tests at the typical shale reservoir temperature, there is no phase separation observed in cylinder models. It is possible that at this specific temperature, the fluid is close to or beyond the critical point and there is only one phase for fluids in cylinder pores. This observation agrees with the experimental work from Dr. Nasrabadi's group in which confinement-induced supercriticality was observed during the experiments of hydrocarbons in nanopores.

In the application of the gauge-GCMC method, some prior information is required. In the simulation of M component fluid using the gauge-GCMC method, the input parameters are temperature T, system volume V, chemical potentials μ_i ($i \neq M$) and total molecular number N_M of component M. All these parameters are kept as constant during the simulation process. Since the chemical potentials are included in the input list, there should be some prior information about the selected values. However, the chemical potential, also known as partial molar free energy, is hard to measure directly in the real conditions. For most of the time, only the change of chemical potential $\Delta\mu$ is available but not the absolute value. Since we need the $\mu - \rho$ diagrams in the shape of van der Waals loop for the phase equilibrium computation, an initial setting located in the

two-phase region is necessary and it can also reduce the simulation cost. Thus, some trial tests are necessary to get the suitable values of chemical potentials that the initial settings are located in the two-phase region. For example, in the ternary case $C_1/C_3/nC_5$, several trial tests are performed for pure light components (such as C_1 or C_3) to get possible chemical potentials. Based on the smallest values of (μ_{C_1}, μ_{C_3}), the first S-shape $\mu_{nC_5} - \rho$ relationship could be generated. Usually, the two-phase region for ternary fluids is able to be reached by modifying the chemical potentials of pure component tests. Since other Monte Carlo methods are not easy to apply in the simulation of multiple component fluids, as stated in chapter 2, gauge-GCMC is the first choice although some trial tests are required.

The gauge-GCMC method is designed for the simulation of multiple component fluids under confinement. However, the problem in field application is more complicated, for example, the fluid phase determination based on field data. Usually, it is available to get the reservoir temperature T, bottom hole pressure P and the fluid composition $C_i\%$ from the field, but not the chemical potentials. This setting is suitable for the simulation based on NPT ensemble, such as NPT-GEMC. But as stated in chapter 2, for NPT-GEMC simulation, the computation cost is prohibitive if multiple components are considered or explicit boundary model is included. Some trial tests, not covered in this work, were performed about NPT-GEMC simulation of binary fluids considering the graphite slit boundary. Since the boundary is represented by atoms, it is extremely difficult to perform the volume shift move. Although this obstacle was solved through some coding techniques, the simulation was stuck around the initial configuration or some local minimums and provided some fake results for the phase separation. To solve this practical problem, gauge-GCMC may be a possible choice. By introducing an isobaric control in the gauge box, this gauge meter could mimic the measurement of chemical

potential at some specific temperature and pressure. In addition, since the gauge box could be set in bulk condition, the above obstacle is avoided.

Based on the implementation of some advanced techniques in the molecular simulation, such as the parallel computation and GPU optimization, the simulation time has been greatly reduced. However, engineers hope to have the simulator as fast and accurate as possible, especially when working on a real fluid case. The fluid in shale usually has more than five major components, some of them consist of big molecules (e.g. C_7). Gauge-GCMC can be applied in those situations, but the simulation time could be a large value. Thus, new techniques are always required to improve the performance of Monte Carlo simulation. Also, cloud technology can help the field engineer to access the local machine for the phase behavior simulation. It is a great way to connect the research project with the field application, although it is out of the scope of this work.

REFERENCES

[1] G. Gulen, S. Ikonnikova, J. Browning, and S. Tinker, "Fayetteville shale-production outlook," *Society of Petroleum Engineers*, 2014.

[2] J. Browning, S. Ikonnikova, G. GÃijlen, and S. Tinker, "Barnett shale production outlook," *Society of Petroleum Engineers*, 2013.

[3] B. Jin and H. Nasrabadi, "Phase behavior of multi-component hydrocarbon systems in nano-pores using gauge-gcmc molecular simulation," *Fluid Phase Equilibria*, vol. 425, pp. 324 – 334, 2016.

[4] Z. Jin and A. Firoozabadi, "Thermodynamic Modeling of Phase Behavior in Shale Media," *SPE J.*, pp. 1–18, 2015.

[5] S. K. Singh, A. Sinha, G. Deo, and J. K. Singh, "Vapor-liquid phase coexistence, critical properties, and surface tension of confined alkanes," *J. Phys. Chem. C*, vol. 113, no. 17, pp. 7170–7180, 2009.

[6] J. Rouquerolt, D. Avnir, C. W. Fairbridge, D. H. Everett, J. H. Haynes, N. Pernicone, J. D. F. Ramsay, K. S. W. Sing, and K. K. Unger, "Recommendations for the characterization of porous solids," *Pure Appl. Chem.*, vol. 66, no. 8, pp. 1739–1758, 1994.

[7] C. R. Clarkson, N. Solano, R. M. Bustin, A. M. M. Bustin, G. R. L. Chalmers, L. He, Y. B. Melnichenko, A. P. Radliński, and T. P. Blach, "Pore structure characterization of north american shale gas reservoirs using usans/sans, gas adsorption, and mercury intrusion," *Fuel*, vol. 103, pp. 606–616, 2013.

[8] Y. Zhang, D. Shao, J. Yan, X. Jia, Y. Li, P. Yu, and T. Zhang, "The pore size distribution and its relationship with shale gas capacity in organic-rich mudstone

of wufeng-longmaxi formations, sichuan basin, china," *Journal of Natural Gas Geoscience*, vol. 1, no. 3, pp. 213–220, 2016.

[9] A. A. Hinai, R. Rezaee, L. Esteban, and M. Labani, "Comparisons of pore size distribution: A case from the western australian gas shale formations," *Journal of Unconventional Oil and Gas Resources*, vol. 8, pp. 1–13, 2014.

[10] R. F. Sigal, "Pore-size distributions for organic-shale-reservoir rocks from nuclear-magnetic-resonance spectra combined with adsorption measurements," *Society of Petroleum Engineers*, 2015.

[11] U. Kuila and M. Prasad, "Specific surface area and pore-size distribution in clays and shales," *Geophysical Prospecting*, vol. 61, no. 2, pp. 341–362, 2013.

[12] R. F. Sigal, "Pore-size distributions for organic-shale-reservoir rocks from nuclear-magnetic-resonance spectra combined with adsorption measurements," *SPE J.*, 2015.

[13] G. R. L. Chalmers and R. M. Bustin, "Porosity and pore size distribution of deeply-buried fine-grained rocks: Influence of diagenetic and metamorphic processes on shale reservoir quality and exploration," *Journal of Unconventional Oil and Gas Resources*, vol. 12, pp. 134–142, 2015.

[14] G. R. Chalmers, R. M. Bustin, and I. M. Power, "Characterization of gas shale pore systems by porosimetry, pycnometry, surface area, and field emission scanning electron microscopy/transmission electron microscopy image analyses: Examples from the barnett, woodford, haynesville, marcellus, and doig units," *AAPG Bulletin*, vol. 96, no. 6, pp. 1099–1119, 2012.

[15] A. G. Adesida, I. Akkutlu, D. E. Resasco, and C. S. Rai, "Characterization of barnett shale kerogen pore size distribution using dft analysis and grand canonical monte

carlo simulations.," *Society of Petroleum Engineers.*, 2011.

[16] B. Jin, R. Bi, and H. Nasrabadi, "Molecular simulation of the pore size distribution effect on phase behavior of methane confined in nanopores," *Fluid Phase Equilibria*, vol. 452, no. Supplement C, pp. 94 – 102, 2017.

[17] M. E. Curtis, R. J. Ambrose, C. H. Sondergeld, and C. S. Rai, "Investigation of the relationship between organic porosity and thermal maturity in the marcellus shale," *Proceedings of the North American Unconventional Gas Conference and Exhibition*, 2011.

[18] M. Gasparik, A. Ghanizadeh, P. Bertier, Y. Gensterblum, S. Bouw, and B. M. Krooss, "High-pressure methane sorption isotherms of black shales from the netherlands," *Energy & Fuels*, vol. 26, no. 8, pp. 4995–5004, 2012.

[19] T. Zhang, G. S. Ellis, S. C. Ruppel, K. Milliken, and R. Yang, "Effect of organic-matter type and thermal maturity on methane adsorption in shale-gas systems," *Organic Geochemistry*, vol. 47, no. Supplement C, pp. 120 – 131, 2012.

[20] M. E. Curtis, R. J. Ambrose, and C. H. Sondergeld, "Structural characterization of gas shales on the micro- and nano-scales," *Proceedings of the Canadian Unconventional Resources and International Petroleum Conference*, 2010.

[21] F. P. Wang and R. M. Reed, "Pore networks and fluid flow in gas shales," *Proceedings of the SPE Annual Technical Conference and Exhibition*, 2009.

[22] S. Montgomery, D. Jarvie, K. Bowker, and R. Pollastro, "Mississippian barnett shale, fort worth basin, north-central texas: Gas-shale play with multi-trillion cubic foot potential," *AAPG Bulletin*, vol. 89, no. 2, pp. 155 – 175, 2005.

[23] M. Thommes and G. H. Findenegg, "Pore Condensation and Critical-Point Shift of a Fluid in Controlled-Pore Glass," *Langmuir*, vol. 10, pp. 4270–4277, 1994.

[24] A. de Keizer, T. Michalski, and G. H. Findenegg, "Fluids in pores: experimental and computer simulation studies of multilayer adsorption, pore condensation and critical-point shifts," *Pure Appl. Chem.*, vol. 63, no. 10, pp. 1495–1502, 1991.

[25] S. Z. Qiao, S. K. Bhatia, and D. Nicholson, "Study of Hexane Adsorption in Nanoporous MCM-41 Silica," *Langmuir*, vol. 20, no. 2, pp. 389–395, 2004.

[26] S. Luo, H. Nasrabadi, and J. L. Lutkenhaus, "Effect of confinement on the bubble points of hydrocarbons in nanoporous media," *AIChE J.*, 2016.

[27] S. Luo, J. L. Lutkenhaus, and H. Nasrabadi, "Experimental Study of Confinement Effect on Hydrocarbon Phase Behavior in Nano-Scale Porous Media Using Differential Scanning Calorimetry," *SPE Annu. Tech. Conf. Exhib.*, 2015.

[28] S. Luo, J. L. Lutkenhaus, and H. Nasrabadi, "Confinement-induced supercriticality and phase equilibria of hydrocarbons in nanopores," *Langmuir*, vol. 32, no. 44, pp. 11506–11513, 2016.

[29] Q. Wu, B. Bai, Y. Ma, J. T. Ok, K. B. Neeves, and X. Yin, "Optic Imaging of Two-Phase-Flow Behavior in 1D Nanoscale Channels," *SPE J.*, pp. 793–802, 2014.

[30] L. Wang, E. Parsa, Y. Gao, J. T. Ok, K. Neeves, X. Yin, and E. Ozkan, "Experimental Study and Modeling of the Effect of Nanoconfinement on Hydrocarbon Phase Behavior in Unconventional Reservoirs," *SPE Annu. Tech. Conf. Exhib.*, 2014.

[31] M. Alfi, H. Nasrabadi, and D. Banerjee, "Experimental investigation of confinement effect on phase behavior of hexane, heptane and octane using lab-on-a-chip technology," *Fluid Phase Equilibria*, vol. 423, pp. 25 – 33, 2016.

[32] A. L. Myers and J. M. Prausnitz, "Thermodynamics of mixed-gas adsorption," *AIChE J.*, vol. 11, no. 1, pp. 121–127, 1965.

[33] R. J. Ambrose, R. C. Hartman, M. Diaz Campos, I. Y. Akkutlu, and C. H. Sondergeld, "New pore-scale considerations for shale gas in place calculations," *SPE Unconv. Gas Conf.*, 2010.

[34] R. J. Ambrose, R. C. Hartman, and I. Y. Akkutlu, "Multi-component sorbed-phase considerations for shale gas-in-place calculations," *SPE Prod. Oper. Symp.*, 2011.

[35] I. Langmuir, "The constitution and fundamental properties of solids and liquids. Part I. Solids.," *J. Am. Chem. Soc.*, vol. 252, pp. 2221–2295, 1916.

[36] S. Brunauer, P. H. Emmett, and E. Teller, "Adsorption of gases in multimolecular layers," *J. Am. Chem. Soc.*, vol. 60, no. 1, pp. 309–319, 1938.

[37] B. Lippens and J. de Boer, "Studies on pore systems in catalysts: V. the t method," *Journal of Catalysis*, vol. 4, no. 3, pp. 319 – 323, 1965.

[38] Z. Li, Z. Jin, and A. Firoozabadi, "Phase Behavior and Adsorption of Pure Substances and Mixtures and Characterization in Nanopore Structures by Density Functional Theory," *SPE J.*, vol. 19, no. 6, pp. 1096–1109, 2014.

[39] B. Nojabaei, R. T. Johns, and L. Chu, "Effect of Capillary Pressure on Phase Behavior in Tight Rocks and Shales," *SPE Reserv. Eval. Eng.*, vol. 16, no. 03, pp. 281–289, 2013.

[40] E. Parsa, X. Yin, and E. Ozkan, "Direct Observation of the Impact of Nanopore Confinement on Petroleum Gas Condensation," *SPE Annu. Tech. Conf. Exhib.*, 2015.

[41] Y. Ma, L. Jin, and A. Jamili, "Modifying Van Der Waals Equation of State to Consider Influence of Confinement on Phase Behavior," *SPE Annu. Tech. Conf. Exhib.*, 2013.

[42] L. Jin, Y. Ma, and A. Jamili, "Investigating The Effect of Pore Proximity on Phase Behavior And Fluid Properties in Shale Formations," *SPE Annu. Tech. Conf. Exhib.*, 2013.

[43] S. P. Tan and M. Piri, "Equation-of-state modeling of associating-fluids phase equilibria in nanopores," *Fluid Phase Equilibria*, vol. 405, no. Supplement C, pp. 157 – 166, 2015.

[44] X. Dong, H. Liu, J. Hou, K. Wu, and Z. Chen, "Phase equilibria of confined fluids in nanopores of tight and shale rocks considering the effect of capillary pressure and adsorption film," *Industrial & Engineering Chemistry Research*, vol. 55, no. 3, pp. 798–811, 2016.

[45] K. Sapmanee, *Effects of Pore Proximity on Behavior and Production Prediction of Gas/condensate*. University of Oklahoma, 2011.

[46] D. Devegowda, K. Sapmanee, F. Civan, and R. Sigal, "Phase behavior of gas condensates in shales due to pore proximity effects: Implications for transport reserves and well productivity," *SPE Annu. Tech. Conf. Exhib.*, 2012.

[47] N. S. Alharthy, T. N. Nguyen, T. W. Teklu, H. Kazemi, and R. M. Graves, "Multiphase Compositional Modeling in Small-Scale Pores of Unconventional Shale Reservoirs," *SPE Annu. Tech. Conf. Exhib.*, 2013.

[48] L. Travalloni, M. Castier, and F. W. Tavares, "Phase equilibrium of fluids confined in porous media from an extended peng–robinson equation of state," *Fluid Phase Equilibria*, vol. 362, no. Supplement C, pp. 335 – 341, 2014. Special Issue on PPEPPD 2013.

[49] Z. Jin and A. Firoozabadi, "Phase behavior and flow in shale nanopores from molecular simulations," *Fluid Phase Equilibria*, vol. 430, pp. 156–168, 2016.

[50] A. Z. Panagiotopoulos, "Monte Carlo methods for phase equilibria of fluids," *J. Phys. Cond. Matt.*, vol. 25, pp. 25–52, 2000.

[51] J. J. de Pablo, Q. Yan, and F. A. Escobedo, "Simulation of phase transitions in fluids," *Annu. Rev. Phys. Chem.*, vol. 50, pp. 377–411, 1999.

[52] a. Trokhymchuk and J. Alejandre, "Computer simulations of liquid/vapor interface in Lennard-Jones fluids: Some questions and answers," *J. Chem. Phys.*, vol. 111, no. 1999, pp. 8510–8523, 1999.

[53] I. Brovchenko, a. Geiger, and a. Oleinikova, "Water in nanopores. I. Coexistence curves from Gibbs ensemble Monte Carlo simulations.," *J. Chem. Phys.*, vol. 120, no. 4, pp. 1958–1972, 2004.

[54] A. Z. Panagiotopoulos, "Direct determination of phase coexistence properties of fluids by Monte Carlo simulation in a new ensemble," *Mol. Phys.*, vol. 100, no. 1, pp. 237–246, 1987.

[55] A. Z. Panagiotopoulos, N. Quirke, M. Stapleton, and D. J. Tildesley, "Phase equilibria by simulation in the Gibbs ensemble. Alternative derivation, generalization and application to mixture and membrane equilibria.," *Mol. Phys.*, vol. 63, no. 4, pp. 527–545, 1988.

[56] A. Z. Panagiotopoulos, "Adsorption and capillary condensation of fluids in cylindrical pores by Monte Carlo simulation in the Gibbs ensemble," *Mol. Phys.*, vol. 62, no. 3, pp. 701–719, 1987.

[57] B. R. Didar and I. Y. Akkutlu, "Pore-size Dependence of Fluid Phase Behavior and Properties in Organic-Rich Shale Reservoirs," *SPE Int. Symp. Oilf. Chem.*, 2013.

[58] D. Frenkel and B. Smit, "Monte Carlo Simulations in Various Ensembles," in *Underst. Mol. Simul. (Second Ed.* (D. Frenkel and B. Smit, eds.), ch. 5, pp. 111–137,

San Diego: Academic Press, second edi ed., 2002.

[59] L. A. Rowley, D. Nicholson, and N. G. Parsonage, "Monte Carlo grand canonical ensemble calculation in a gas-liquid transition region for 12-6 Argon," *J. Comput. Phys.*, vol. 17, no. 4, pp. 401–414, 1975.

[60] G. Calleja, B. Coto, A. Pinar, and A. M. Morales-Cas, "Ethane adsorption in slit-shaped micropores: Influence of molecule orientation on adsorption capacity," *Adsorption*, vol. 12, no. 1, pp. 45–54, 2006.

[61] D. D. Do and H. D. Do, "Adsorption of flexible n-alkane on graphitized thermal carbon black: Analysis of adsorption isotherm by means of GCMC simulation," *Chem. Eng. Sci.*, vol. 60, no. 7, pp. 1977–1986, 2005.

[62] D. D. Do and H. D. Do, "Evaluation of 1-site and 5-site models of methane on its adsorption on graphite and in graphitic slit pores," *The Journal of Physical Chemistry B*, vol. 109, no. 41, pp. 19288–19295, 2005.

[63] J. J. Potoff and A. Z. Panagiotopoulos, "Critical point and phase behavior of the pure fluid and a Lennard-Jones mixture," *J. Chem. Phys.*, vol. 109, no. 24, pp. 10914–10920, 1998.

[64] J. J. Potoff, J. Errington, and A. Z. Panagiotopoulos, "Molecular simulation of phase equilibria for mixtures of polar and non-polar components," *Mol. Phys.*, vol. 97, no. 10, pp. 1073–1083, 1999.

[65] J. J. Potoff and J. I. Siepmann, "Vapor-Liquid Equilibria of Mixtures Containing Alkanes , Carbon Dioxide , and Nitrogen," *AIChE J.*, vol. 47, no. 7, pp. 1676–1682, 2001.

[66] G. Kamath and J. J. Potoff, "Monte Carlo predictions for the phase behavior of H2 S+n-alkane, H2 S+CO2, CO2+CH4 and H2 S+CO2+CH4 mixtures," *Fluid Phase*

Equilib., vol. 246, no. 1-2, pp. 71–78, 2006.

[67] A. V. Neimark and A. Vishnyakov, "Gauge cell method for simulation studies of phase transitions in confined systems," *Phys. Rev. E*, vol. 62, no. 4 Pt A, pp. 4611–4622, 2000.

[68] A. Vishnyakov and A. V. Neimark, "Studies of liquid-vapor equilibria, criticality, and spinodal transitions in nanopores by the gauge cell Monte Carlo simulation method," *J. Phys. Chem. B*, vol. 105, no. 29, pp. 7009–7020, 2001.

[69] A. Vishnyakov and A. V. Neimark, "Multicomponent gauge cell method," *J. Chem. Phys.*, vol. 130, no. 22, 2009.

[70] N. Metropolis, "Equation of State Calculations by Fast Computing Machines," *J. Chem. Phys.*, vol. 21, no. 6, p. 1087, 1953.

[71] M. P. Allen and D. J. Tildesley, *Computer Simulation of Liquids (Oxford Science Publications)*. Oxford science publications, Oxford University Press, reprint ed., jun 1989.

[72] W. G. Madden, A. I. Pesci, and K. F. Freed, "Phase equilibria of lattice polymer and solvent: tests of theories against simulations," *Macromolecules*, vol. 23, no. 4, pp. 1181–1191, 1990.

[73] Q. Yan, H. Liu, and Y. Hu, "Simulation of Phase Equilibria for Lattice Polymers," *Macromolecules*, vol. 29, no. 11, pp. 4066–4071, 1996.

[74] F. Goujon, P. Malfreyt, A. Boutin, and A. H. Fuchs, "Vapour-Liquid Phase Equilibria of n-alkanes by Direct Monte Carlo Simulations," *Mol. Simul.*, vol. 27, no. 2, pp. 99–114, 2001.

[75] A. D. Mackie and A. Z. Panagiotopoulos, "Monte Carlo simulations of phase equilibria for a lattice homopolymer model," *Chem. Phys.*, vol. 1014, no. 1995, 1995.

[76] A. D. Mackie, K. Onur, and A. Z. Panagiotopoulos, "Phase equilibria of a lattice model for an oil-water-amphiphile mixture," *The Journal of Chemical Physics*, vol. 104, no. 10, pp. 3718–3725, 1996.

[77] B. L. Severson and R. Q. Snurr, "Monte Carlo simulation of n-alkane adsorption isotherms in carbon slit pores," *J. Chem. Phys.*, vol. 126, no. 13, p. 134708, 2007.

[78] B. K. Peterson and K. E. Gubbins, "Phase transitions in a cylindrical pore," *Molecular Physics*, vol. 62, no. 1, pp. 215–226, 1987.

[79] A. M. Ferrenberg, D. P. Landau, and R. H. Swendsen, "Statistical errors in histogram reweighting," *Phys. Rev. E*, vol. 51, no. 5, pp. 5092–5100, 1995.

[80] A. Ferrenberg and R. Swendsen, "New Monte Carlo technique for studying phase transitions," *Phys. Rev. Lett.*, vol. 61, no. 23, pp. 2635–2638, 1988.

[81] A. M. Ferrenberg and R. H. Swendsen, "Optimized Monte Carlo data analysis," *Phys. Rev. Lett.*, vol. 63, no. 12, pp. 1195–1198, 1989.

[82] R. H. Swendsen, "Modern methods of analyzing Monte Carlo computer simulations," *Physica A*, vol. 194, no. 1-4, pp. 53–62, 1993.

[83] R. H. Swendsen and A. M. Ferrenberg, "Histogram methods for monte carlo data analysis," in *Computer Simulation Studies in Condensed Matter Physics II* (D. P. Landau, K. K. Mon, and H.-B. Schüttler, eds.), (Berlin, Heidelberg), pp. 179–183, Springer Berlin Heidelberg, 1990.

[84] J. J. Potoff, *Monte Carlo simulation of mixture phase behavior: methods and applications*. PhD thesis, 1999.

[85] J. V. Sengers and J. M. H. L. Sengers, "Thermodynamic Behavior of Fluids near the critical point," *Ann. Rev. Phys. Chem.*, vol. 37, pp. 189–222, 1986.

[86] N. B. Wilding, "Simulation studies of fluid critical behaviour," *J. Phys. Condens. Matter*, vol. 9, pp. 585–612, 1997.

[87] A. D. Bruce and N. B. Wilding, "Scaling fields and universality of the liquid-gas critical point," *Phys. Rev. Lett.*, vol. 68, no. 2, pp. 193–196, 1992.

[88] A. Z. Panagiotopoulos, *Molecular Simulation of Phase Equilibria*, pp. 411–437. Dordrecht: Springer Netherlands, 1994.

[89] A. Z. Panagiotopoulos, "Exact Calculations of Fluid Phase Equilibria By Monte Carlo Simulations in a New Statistical Ensemble," *Int. J. Thermophys.*, vol. 10, no. 2, pp. 447–457, 1989.

[90] A. Firoozabadi, *Thermodynamics of Hydrocarbon Reservoirs*. McGraw-Hill Education, 1999.

[91] J. S. Rowlinson, F. L. Swinton, J. E. Baldwin, A. D. Buckingham, and S. Danishefsky, "Liquids and Liquid Mixtures (Third edition)," Butterworths Monographs in Chemistry, Butterworth-Heinemann, third edit ed., 1982.

[92] J. S. Rowlinson and B. Widom, *Molecular theory of capillarity*. International series of monographs on chemistry, Clarendon Press, 1982.

[93] G. Maitland, M. Rigby, E. B. Smith, W. Wakeham, and D. Henderson, "Intermolecular forces: Their origin and determination," vol. 36, pp. 57–, 01 1983.

[94] M. G. Martin and J. I. Siepmann, "Transferable Potentials for Phase Equilibria. 1. United-Atom Description of n -Alkanes," *J. Phys. Chem. B*, vol. 102, no. 97, pp. 2569–2577, 1998.

[95] J. N. C. Lopes and D. J. Tildesley, "Multiphase equilibria using the Gibbs ensemble Monte Carlo method," *Mol. Phys.*, vol. 92, no. 2, pp. 187–196, 1997.

[96] D. Berthelot, "Sur le mélange des gaz," *Comptes rendus Hebd. des séances l'Académie des Sci.*, vol. 126, pp. 338–340, 1898.

[97] H. J. C. B. van der Ploeg, P., "Molecular dynamics simulation of a bilayer membrane," *The Journal of Chemical Physics*, vol. 76, no. 6, pp. 3271 – 3276, 1982.

[98] W. L. Jorgensen, J. D. Madura, and C. J. Swenson, "Optimized intermolecular potential functions for liquid hydrocarbons," *Journal of the American Chemical Society*, vol. 106, no. 22, pp. 6638–6646, 1984.

[99] J. I. Siepmann, *Monte Carlo Methods for Simulating Phase Equilibria of Complex Fluids*, pp. 443–460. John Wiley & Sons, Inc., 2007.

[100] M. G. Martin and A. L. Frischknecht, "Using arbitrary trial distributions to improve intramolecular sampling in configurational-bias Monte Carlo," *Mol. Phys.*, vol. 104, no. 15, pp. 2439–2456, 2006.

[101] M. G. Martin, "MCCCS Towhee: a tool for Monte Carlo molecular simulation," *Mol. Simul.*, vol. 39, no. 14-15, pp. 1212–1222, 2013.

[102] K. E. Gubbins, Y. Long, and M. Śliwinska-Bartkowiak, "Thermodynamics of confined nano-phases," *The Journal of Chemical Thermodynamics*, vol. 74, pp. 169 – 183, 2014.

[103] R. Evans, U. M. B. Marconi, and P. Tarazona, "Fluids in narrow pores: Adsorption, capillary condensation, and critical points," *J. Chern. Phys.*, vol. 84, no. 4, 1986.

[104] P. J. Linstrom and W. G. Mallard, "NIST Chemistry WebBook,," *Natl. Inst. Stand. Technol.*, p. NIST Standard Reference Database Number 69, 2016.

[105] D. Y. Peng and D. B. Robinson, "A New Two-Constant Equation of State," *Ind. Eng. Chem. Fundam.*, vol. 15, no. 1, pp. 59–64, 1976.

[106] R. Yang, S. He, J. Yi, and Q. Hu, "Nano-scale pore structure and fractal dimension of organic-rich wufeng-longmaxi shale from jiaoshiba area, sichuan basin: Investigations using fe-sem, gas adsorption and helium pycnometry," *Marine and Petroleum Geology*, vol. 70, pp. 27–45, 2016.

[107] S. Luo, J. L. Lutkenhaus, and H. Nasrabadi, "Use of differential scanning calorimetry to study phase behavior of hydrocarbon mixtures in nano-scale porous media," *Journal of Petroleum Science and Engineering*, p. Available online 15 December 2016, 2016.

[108] J. Collell, P. Ungerer, G. Galliero, M. Yiannourakou, F. Montel, and M. Pujol, "Molecular simulation of bulk organic matter in type ii shales in the middle of the oil formation window," *Energy & Fuels*, vol. 28, no. 12, pp. 7457–7466, 2014.

[109] B. P. Tissot and D. H. Welte. Berlin, Germany: Springer, 1984.

[110] Behar, F. and Vandenbroucke, M., "Représentation chimique de la structure des kèrogènes et des asphaltènes en fonction de leur origine et de leur degré d'évolution," *Rev. Inst. Fr. Pét.*, vol. 41, no. 2, pp. 173–188, 1986.

[111] B. Jin and H. Nasrabadi, "Phase Behavior in Shale Organic and Inorganic Nanopores From Molecular Simulation," *SPE Annu. Tech. Conf. Exhib.*, 2017.

[112] U. EIA, "Updates to the eia eagle ford play maps," 2014.

[113] I. Deighton, "Basin temperature modeling using large bottom hole temperature datasets," *SMU Power Plays Geothermal Conference*, 2015.

[114] Pioneer, "Eagle ford shale field tour," 2011.

[115] M. Waldman and A. Hagler, "New combining rules for rare gas van der waals parameters," *Journal of Computational Chemistry*, vol. 14, no. 9, pp. 1077–1084, 1993.

[116] H. Sun, "Compass: An ab initio force-field optimized for condensed-phase applicationsoverview with details on alkane and benzene compounds," *The Journal of Physical Chemistry B*, vol. 102, no. 38, pp. 7338–7364, 1998.

[117] J. E. Jones, "On the determination of molecular fields. ii. from the equation of state of a gas," *Proceedings of the Royal Society of London A: Mathematical, Physical and Engineering Sciences*, vol. 106, no. 738, pp. 463–477, 1924.

[118] S. Plimpton, "Fast parallel algorithms for short-range molecular dynamics," *Journal of Computational Physics*, vol. 117, no. 1, pp. 1 – 19, 1995.

[119] W. G. Hoover, "Canonical dynamics: Equilibrium phase-space distributions," *Phys. Rev. A*, vol. 31, pp. 1695–1697, Mar 1985.

[120] W. G. Hoover, "Constant-pressure equations of motion," *Phys. Rev. A*, vol. 34, pp. 2499–2500, Sep 1986.

[121] C. R. Clarkson and B. Haghshenas, "Modeling of Supercritical Fluid Adsorption on Organic-Rich Shales and," *Society of Petroleum Engineers*, no. 2011, pp. 1–24, 2013.

[122] mindat.org.

[123] S. Xiao, S. A. Edwards, and F. Gräter, "A new transferable forcefield for simulating the mechanics of caco3 crystals," *The Journal of Physical Chemistry C*, vol. 115, no. 41, pp. 20067–20075, 2011.